UNIVERSITÀ DEGLI STUDI DI PALERMO

Mechanical, Manufacturing, Management and Aerospace Innovation

Dipartimento di Ingegneria

A study on damage evolution in composite laminates

A Ritz computational framework for VAT plates and experimental tests for SHM systems

Dottorando

Dott. Dario Campagna

Coordinatore

Prof.ssa Giovanna Lo Nigro

Tutor

Prof. Ivano Benedetti

Co-Tutor

Prof. Alberto Milazzo

M3AI — CICLO XXXIV

Abstract

This thesis investigates the development and implementation of numerical damage models and experimental tests for damage detection and monitoring in thermoplastic composite plates.

The core of this thesis is a numerical formulation based on the Ritz method within the Continuum Damage Mechanics framework, offering insights into the initiation, evolution, and failure of composite laminates, including Variable Angle Tow configurations. This method shows a remarkable reduction in computational costs compared to traditional approaches. However, the study also identifies limitations in the single-domain Ritz approach, highlighting the need for adaptive techniques to mitigate spurious numerical effects.

Additionally, part of the research activities have been performed at *Centro Italiano Ricerche Aerospaziali*, collaborating on an ongoing project featuring experimental tests on thermoplastic composite materials. This experimental campaign involved testing thermoplastic composite coupons equipped with various sensors, such as Fibre Bragg Gratings and distributed fibre optics. These tests aimed to evaluate the ability of the considered sensors to detect and localise damage under controlled conditions. The findings indicate that both sensor types are effective in damage detection, providing essential data for refining the numerical models, and laying the groundwork for the development of a fully functional SHM system for thermoplastic composite materials in

aerospace applications.

Future research directions include extensive experimental validation of the numerical models, integration of advanced sensor technologies with SHM systems, and the development of sophisticated algorithms for data analysis and damage prediction. The ultimate goal is to create more robust and reliable SHM systems, ensuring the safety and longevity of engineering structures.

Contents

List of Figures

List of Tables

List of Abbreviations

BVD Barely visible damage.

CDM Continuum Damage Mechanics.

CIRA Centro Italiano Ricerche Aerospaziali.

CZM Cohesive zone model.

DOF Degrees of freedom.

FBG Fibre Bragg Grating.

FEM Finite Element Method.

FSDT First-order shear deformation theory.

NDE Non-destructive evaluation.

RVE Representative volume element.

SHM Structural Health Monitoring.

TB1 Test Batch #1.

TB2 Test Batch #2.

VAT Variable Angle Tow.

Chapter 1

Introduction

1.1 Motivation

Multilayered composite materials enable the design of lightweight structures with improved stiffness, strength and fatigue properties when compared to metallic structures. For this reason, they find extensive applications in various fields of engineering, including the aerospace, naval, and automotive industries. Moreover, the use of thermoplastic resin instead of thermoset types enables the recyclability of the component at the end of its service life. Thermoplastics offer significant advantages over thermosetting materials, not only enabling the recyclability of components at the end of their service life but also facilitating in situ repairs without the need for disassembly. Additionally, these materials can simplify the manufacturing processes, further enhancing their appeal in various industrial applications [2, 3]. Recent advancements in manufacturing techniques such as automated fibre placement, automated tape laying, and additive manufacturing have made it possible to create thermoplastic composite structures with variable mechanical properties [4, 5, 6, 7]. This innovation has led to the development of Variable Angle Tow (VAT) laminates, in which the

in-plane orientation of the fibres within the individual plies varies according to selected laws throughout the structure [8]. Significant advances have been made in the development and optimisation of VAT composites, trying to identify the fibre patterns that may enhance properties of interest, e.g. the buckling load [9], the fundamental frequencies [10, 11], or the dynamic response under low-speed impact [12].

Despite the benefits of thermoplastic composite materials, they are still under investigation for their full potential in various industrial applications. Designers and engineers require modelling and computational tools capable of accurately predicting the structural response of the designed components. The need for such tools is particularly critical when new manufacturing techniques, as in the case of VAT composites, widen the design space. One of the most widely used computer methods for solving structural problems is the Finite Element Method (FEM) [13, 14, 15, 16], which has also attained a recognised level of commercial maturity. Due to the high variability of the in-plane and through-the-thickness material features, the accurate FE analysis of VAT laminates critically depends on the quality and resolution of the employed mesh, thus generally attracting considerable computational costs [17]. To mitigate such problems and speed up the analysis, while retaining a high level of accuracy, various mesh-less methods have been developed as alternatives to FEM [18, 19, 20, 21]. The Ritz method, which may be thought of as a global mesh-less technique in this context, has shown success in the study of conventional, laminated, and VAT composite structures [22, 23, 24, 25, 10, 11].

Different works have focused on the study of damage evolution in VAT composite plate using damage models at different scale of idealisation [26, 27, 28, 29, 30, 31, 32]. Modelling progressive damage in composite materials is challenging due to the many damage mechanisms that must be considered. Depending on the idealisation scale, damage can be modelled in various ways,

from the micro-scale to the macro-scale. Using a micro-mechanical approach, damage initiation and evolution in heterogeneous materials can be investigated considering individual material phases within representative volume elements (RVEs) [33, 34, 35]. Instead, at the macro-scale laminate level, damage may be generally represented either as a softened region [36, 37, 38] or as a hard discontinuity [25, 9]. At the intermediate meso-scale level, in which individual plies are represented as homogeneous, Continuum Damage Mechanics (CDM) is, among different approaches, one of the most employed frameworks for investigating the initiation and evolution of damage [39, 40]. In CDM, damage is generally represented as a progressive loss of material stiffness and different FE approaches have been developed based on such modelling assumption [41, 42, 43, 44, 45].

Finite element formulations have also been employed to develop 3D CDM-based material models to simulate the progressive intra-laminar degradation of fibre reinforced laminates as well as delamination using cohesive interfaces between layers [46, 47, 48, 49]. In addition to FE-based analysis methods, single domain meshless approaches, such as the Ritz method, have been shown to be effective, especially when dealing with smeared damaged zones [28].

However, in some cases, damage tends to concentrate in a narrow region due to specific loading conditions or initial imperfections [50, 51]. Within a classical single-domain Ritz approach, this localisation of damage can introduce spurious effects when reconstructing the damaged state, commonly due to Gibbs effects, which can result in nonphysical responses. Therefore, designers and engineers must be aware of the constraints and limitations associated with various modelling and computational tools when predicting the structural behaviour of composite materials and components.

Although the Ritz method offers several advantages, there is limited literature considering this approach to investigate damage initiation and evolution.

Existing works on this topic often employ overly simplified damage models that provide a binary representation of damage [52, 53, 54], which are more suitable for identifying damage initiation rather than capturing damage evolution. Therefore, these approaches tend to be overly conservative.

Numerical models, which serve as predictive tools, provide essential insights into the damage mechanisms and structural responses of thermoplastic composites under various load conditions. By simulating damage processes and their impact on material integrity, these models help identify potential weak points and the conditions under which damage is likely to occur. This modelling is critical not only for understanding material behaviour but also for laying the groundwork for practical applications, such as in the design and implementation of Structural Health Monitoring (SHM) systems [55].

The rising cost of maintenance is a significant challenge in many engineering fields, especially in damage tolerance approaches in product design, leading to complex and frequent maintenance inspection schedules. Engineers often face logistical problems and difficulties in predicting damage propagation in different materials, particularly composite materials. In response to these challenges, the detection of structural damage has become a primary focus of research over the past decades. SHM systems have emerged as a crucial solution, offering a continuous assessment of structural integrity [56]. This reduces the frequency of necessary inspections and extends the intervals between them, ensuring the safety and reliability of critical components across various engineering domains.

A key advantage of SHM systems is their ability to perform non-destructive inspections, ensuring that structures remain intact while detecting and monitoring potential damage. This practice minimises the number of indispensable inspections and maximises the time between required checks. The successful development of an SHM system for thermoplastic composites begins with

two foundational activities: detailed numerical modelling and comprehensive experimental testing. These initial steps are essential for ensuring that the eventual SHM system can effectively detect and monitor damage within these advanced materials.

Parallel to numerical modelling, experimental tests are fundamental for validating theoretical predictions and determining optimal sensor placements and configurations in later stages of SHM system development. Before an SHM system can be fully implemented, selected sensors and monitoring technologies need to be verified for their capability to detect and quantify damage accurately within thermoplastic composites. In this thesis work, experimental tests were performed to evaluate the performance of different sensor types under controlled damage scenarios, thereby generating empirical data that can be used to refine the numerical models. This step ensures that the sensors chosen are sensitive enough to detect the onset of damage early and robust enough to operate under the specific conditions expected in practical applications.

In this context, SHM systems represent a significant advancement in the maintenance and management of engineering structures, providing a sophisticated method to address the complex issues associated with damage detection and maintenance scheduling.

1.2 Thesis outline

This thesis incorporates the author's prior work from various projects, including findings from previously published peer-reviewed journal and conference articles [57, 58, 59, 60, 28, 61]. After the current introduction Chapter, it is structured as follows:

- *Chapter 2* gives an overview of the current state of the art about damage modelling in composite materials and the importance of developing

damage numerical model along with experiments to lay the foundation of development of SHM systems.

- *Chapter 3* presents details about the theoretical framework developed for the numerical damage model with the definition of the fundamental equations, including the damage model adopted within the CDM framework.

- *Chapter 4* introduces a novel CDM-Ritz numerical scheme for the progressive damage analysis in composite material. The governing equations of the structure are derived using the principle of total potential energy along with the Ritz method. Furthermore, the chapter presents two different approaches to the damage model, highlighting the strengths and weaknesses of both approaches.

- *Chapter 5* provides the comprehensive plan for the experimental tests and a detailed descriptions of the tests that was performed during a six months visiting period at *Centro Italiano Ricerche Aerospaziali* (CIRA). It begins with an overview of the experimental objectives and then gives specifics for each test, including the materials and specimens used, the equipment setup, and the step-by-step procedures to be followed.

- *Chapter 6* shows the results obtained from both the numerical models and the experimental tests. It begins with the numerical results, detailing the performance and predictive capabilities of the developed models under various conditions. Graphical representations, tables, and comprehensive analyses highlight key trends and observations. Next, the chapter presents the outcomes of the experimental tests, including force and displacement measurements, strain data from sensors, and observations related to damage detection and propagation. Each set of results

is analysed to explore their implications, and address potential sources of error.

- *Chapter 7* concludes the thesis by summarising key findings and guiding future developments. It highlights the contributions of the CDM-Ritz damage models and experimental tests, examining their strengths and limitations. Suggestions for further research and development are also discussed.

Chapter 2

State of the art

In this chapter, to better understand the context and motivation behind this thesis, a comprehensive review of the state of the art is presented. Starting with a theoretical overview of various damage models for composite materials, the chapter will explore the fundamentals of Structural Health Monitoring. Additionally, the necessity of numerical models in conjunction with experimental tests will be discussed to highlight their significance in advancing SHM systems.

2.1 Damage models for composite plates

Composite materials are widely used in various industries due to their high strength-to-weight ratio and customizable properties. However, their complex nature poses significant challenges for damage modelling. Before focusing on how damage can be modeled, it is essential to first understand the types of damage that can occur in composite plates.

Longitudinal Failure

In fibre-reinforced composites, most of the applied loads are carried by the fibres. When these fibres fail, whether due to tension or compression, the internal stresses must be redistributed to other parts of the structure. This redistribution can potentially lead to a catastrophic failure of the entire structure.

For composites with a high fibre volume fraction, and in those where the resin matrix's strain to failure is greater than that of the reinforcing fibres, such as carbon-epoxy composites, longitudinal failure typically begins with isolated fibre fractures in weak regions. These localised fibre fractures increase the normal and interfacial shear stresses in neighbouring fibres. The resulting local stress concentrations can cause matrix cracking, fibre-matrix debonding, and, in ductile matrices, conical shear failures. As the load continues to increase, additional fibre fractures occur, ultimately leading to the structure's collapse.

When a composite is subjected to longitudinal tensile loading, failure occurs in both the fibres and the matrix. Fracture typically propagates along a plane parallel to the fibres and the thickness direction [62], see i.e. Fig.(2.1). On the other hand, when a composite plate is subjected to compressive load-

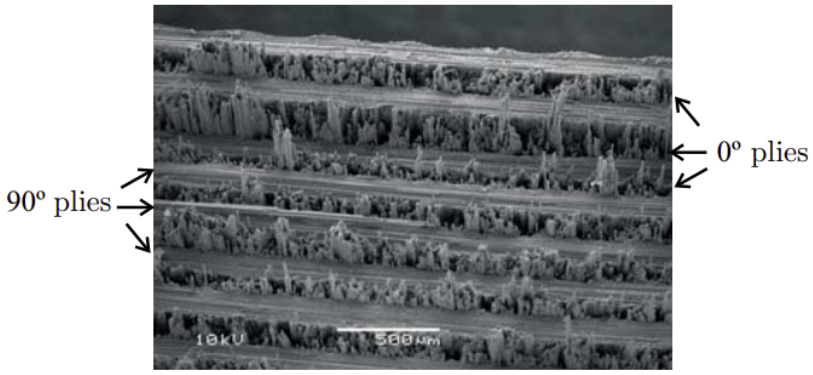

Figure 2.1: Liongitudinal failure for 0° plies.

ing, the structural failure is addressed by the collapsing of the fibres as a result of shear kinking and damage of the supporting matrix [63, 64]. A kink band in a carbon-epoxy laminate resulting from compressive longitudinal stresses is shown in Fig.(2.2) [65]. Argon [66] was the pioneer in analysing the kinking

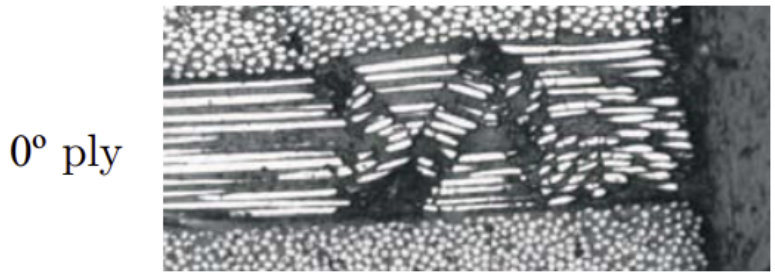

Figure 2.2: Kink band in a 0° ply.

phenomenon, basing his analysis on the assumption of an initial local fibre misalignment. This misalignment induces shear stresses between fibres, causing them to rotate. This rotation, in turn, amplifies the shear stress, ultimately leading to instability.

Transverse failure

Transverse failure includes matrix cracking as well as fibre-matrix debonding. A transverse fracture that grow along the thickness of the ply is caused by the combined action of minor defects, such as small fibre-resin debonds, resin-rich regions, and resin voids, present in a ply and transverse tensile and in-plane shear loads, see i.e Fig.(2.3). The transverse cracks grow in the resin and at the fibre-resin interface without breaking fibres.

Delamination

Delamination is a common damage mechanism in multidirectional laminated composites, primarily due to their inherent weakness in the thickness direc-

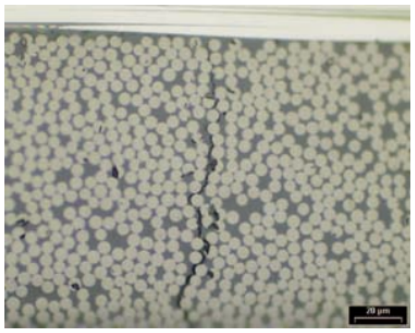

Figure 2.3: Transverse failure in 90° ply.

tion. The three-dimensional stress states that arise near geometric discontinuities—such as ply drop-offs, stiffener terminations, flanges, bonded and bolted joints, and access holes—facilitate the initiation of delamination. This delamination leads to a decrease in the composite structure's bending stiffness and, under compressive loads, can result in local buckling.

After understanding the various types of damage that can occur in composite materials, it becomes essential to explore how these damages can be modelled effectively. Damage modelling is a critical aspect of composite material analysis, as it allows engineers and researchers to predict the initiation, growth, and impact of damage within these complex structures. Through accurate damage modelling, it is possible to design more resilient composite structures and optimise maintenance strategies. The following subsections introduce the key concepts and methodologies used in damage modelling, providing a foundation for understanding how different damage mechanisms can be represented and analyses in composite structures.

2.1.1 Energy-Based Models

Energy-based models are fundamental in understanding damage initiation and propagation in composite materials [67]. These models are based on the princi-

ple that damage occurs when the energy release rate exceeds a critical threshold. The energy release rate G is a measure of the energy available for crack propagation per unit area of the crack surface. In composite materials, the energy release rate can be influenced by factors such as fibre-matrix interactions, matrix cracking, and fibre breakage.

The critical energy release rate G_c is a material property that defines the resistance to crack growth. For a crack to propagate, the energy release rate must reach or exceed this critical value. Energy-based models are particularly useful for predicting the onset of delamination and matrix cracking, which are common failure modes in composites. These models often employ fracture mechanics principles and can be applied to both static and dynamic loading conditions.

Mathematically, the energy release rate for a mode I (opening mode) crack can be expressed as:

$$G_I = \frac{P^2 a}{2BE}, \tag{2.1}$$

where P is the applied load, a is the crack length, B is the specimen width and E is the modulus of elasticity. For mixed-mode loading, the total energy release rate can be calculated using a combination of mode I and mode II components:

$$G_{total} = G_I + G_{II} \tag{2.2}$$

Energy-based models provide a robust framework for understanding the mechanisms of damage initiation and growth in composite materials [68, 69].

2.1.2 Cohesive Zone Models

Cohesive zone models (CZM) are widely used to simulate the initiation and propagation of cracks in composite materials. These models represent the process zone at the crack tip (see Fig.(2.4) [70]), where material separation

occurs, using traction-separation laws [71, 72]. CZMs are particularly effective in capturing the non-linear behaviour associated with damage and failure in composites.

The traction-separation law defines the relationship between the tractions and the displacements at the cohesive zone. A typical traction-separation law is characterised by an initial linear elastic region, followed by a peak traction, and a subsequent softening region leading to complete separation. The area under the traction-separation curve represents the fracture energy G_c required for crack propagation.

Typically, cohesive constitutive models must meet certain criteria, which can be summarised as follows [70]:

- The traction-separation behaviour should remain unaffected by any applied rigid body motion.
- The energy required to create a new surface is finite and related to the fracture energy, which may be evaluated from the area under the traction-separation curve.
- The fracture energy for mode I should generally be distinct from that associated with mode II.
- The cohesive law is associated with a finite characteristic length related to the size of the cracking process zone.
- Beyond a certain threshold, the cohesive traction features a softening behaviour, with traction magnitude decreasing as the separation increases.
- It is possible to define a potential function associated to the decohesion process, so that the energy dissipation is independent on the loading/unloading/reloading path.

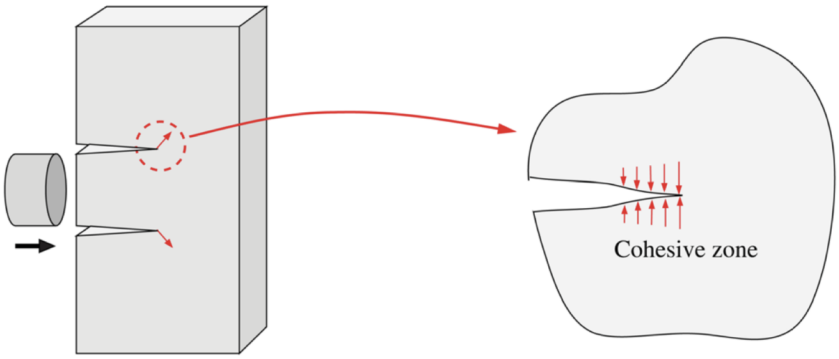

Figure 2.4: Schematic representation of the CZM.

2.1.3 Continuum Damage Mechanics

Continuum Damage Mechanics provides a framework for modelling the progressive degradation of material properties due to damage. Unlike discrete models that simulate individual cracks, CDM treats damage as a continuous variable distributed over the material volume. This approach is particularly useful for predicting complex failure modes in composites, such as fibre breakage, matrix cracking, and delamination.

Numerous researchers have increasingly attempted to tackle the issue of damage growth in laminated fibre-reinforced plastic composites using continuum damage mechanics. In essence, CDM aims to predict the impact of micro-scale defects and damage at the macro-scale level by making assumptions about the nature of the damage and its effects on the material's macro-scale properties, such as elastic modulus [73, 74, 75, 76, 77]. Many CDM approaches base their stress-strain relationships on the concept of strain, stress, or energy equivalence [78, 79]. To predict post-failure behaviour, an evolution law for damage growth must be established. Because these models are developed at the material level, they can be seamlessly integrated into numerical code for practical structural applications, whether for laminated structures or other

types of structures. Ladevèze [40] investigated matrix damage in composites and suggested that only the shear and transverse tensile moduli are influenced by the damage state, while the other independent elastic properties remain unchanged until rupture. Consequently, only two damage variables are necessary for laminates. Another in-plane, anisotropic damage model proposed by Matzenmiller et al. [39] is notable for its damage growth law based on a cumulative distribution function. In addition, the reduction of elastic moduli in Matzenmiller's model is controlled by five damage variables, enabling damage modelling in orthotropic material. The evolution of a damage variable is governed by effective stress components acting on the failure plane.

However, some issues can arise with strain localisation in constitutive models, which are typically expressed in terms of stress-strain relations. In finite element modelling of damage, strain softening behaviour becomes dependent on the mesh size of the finite element. To address this issue, Bažant and Oh [80] proposed a crack band model to establish a smeared formulation that avoids strain localisation. In smeared formulations, the specific or volumetric energy, defined by the area under the stress-strain curve, is related to the material's fracture energy. This means that the fracture energy is distributed over the entire volume of the element. As a result, a geometric parameter relative to the element dimensions, known as the characteristic length, is introduced into the constitutive law. For a square element, this characteristic length is defined by the following relation:

$$L_c = \frac{\sqrt{A_{IP}}}{\cos\theta}, \tag{2.3}$$

where A_{IP} is the area associated with an integration point and θ is the angle of the mesh line along which the crack band advances with the crack direction. However, this relation must be constrained to $\theta = 45°$ degrees. When the direction of crack propagation is unknown, Maimí et al. [81] computed the average of the aforementioned expression for further development. Additionally,

Oliver [82] proposed another method for evaluating characteristic length that is consistent with mesh discretization and takes crack orientation into account.

CDM models, from a more general point of view, introduce a damage variable ω that quantifies the state of damage in the material. The variable ranges from 0 (undamaged) to 1 (fully damaged). The evolution of damage is governed by constitutive laws that relate stress, strain, and damage.

Key features of CDM include:

- **Damage Evolution Laws**: These laws describe how damage accumulates under different loading conditions. They are often based on energy dissipation principles and can include terms for various damage mechanisms;

- **Effective Stress Concept**: CDM uses the concept of effective stress, which accounts for the reduction in load-carrying capacity due to damage. The effective stress $\hat{\sigma}$ is related to the nominal stress $\tilde{\sigma}$ by the damage variable ω following the relation

$$\hat{\sigma} = \frac{\tilde{\sigma}}{1 - \omega} \tag{2.4}$$

In summary, damage modelling in composites involves a range of approaches, from energy-based fracture mechanics to cohesive zone models and continuum damage mechanics. Each method offers unique insights and capabilities, making them valuable tools for predicting and understanding the behaviour of composite materials under various loading conditions.

2.2 Structural Health Monitoring systems

Structural Health Monitoring is an evolving technology designed to continuously observe the condition of structures to detect damage with minimal

human intervention. This chapter provides an overview of SHM systems, their application to composite materials, the types of sensors used, and the primary goals of SHM implementation.

2.2.1 SHM goals

The primary goal of SHM is to improve the reliability and safety of structures while reducing maintenance costs. By continuously monitoring the structural health, SHM systems can detect damage early, preventing catastrophic failures and extending the service life of the structure. In the aerospace industry, where regular inspections can be costly and time-consuming, SHM systems offer a significant advantage by enabling condition-based maintenance [83, 84]. This approach allows for repairs to be made only when necessary, based on real-time data from the SHM system, rather than on a fixed schedule. Additionally, SHM systems can provide valuable insights into the behaviour of composite materials under various loading conditions, contributing to the development of more accurate models and better-designed composite structures. The ultimate goal is to achieve a balance between safety, performance, and cost-effectiveness in maintaining critical structures.

SHM systems aim to enhance the efficiency of maintenance procedures, minimise downtime, and reduce the overall life-cycle cost of structures [85, 86]. By providing continuous monitoring, SHM systems help to identify the exact location and extent of damage, allowing for targeted maintenance interventions. This reduces the need for extensive inspections and repairs, saving time and resources. Furthermore, SHM systems contribute to the safety and reliability of structures by ensuring that any damage is detected and addressed promptly. As the technology evolves, the integration of advanced sensors and data analysis techniques will further improve the capabilities of SHM systems,

making them an indispensable tool in the maintenance of composite materials in various industries.

2.2.2 SHM in composites

Composite materials present unique challenges for SHM due to their anisotropy and heterogeneous nature. Unlike metals or plastics, which have uniform properties, composites are made from fibres and matrix materials that can vary widely in their properties based on the manufacturing process. This complexity makes modelling and damage detection more difficult. Traditional non-destructive evaluation (NDE) techniques, such as visual inspection and x-radiography, often fall short when it comes to detecting subsurface damage in composites [87, 88, 89]. Therefore, advanced SHM systems are very important for monitoring these materials effectively. SHM in composites is especially critical in the aerospace industry, where damage to composite structures can lead to catastrophic failures. By embedding sensors within composite structures, SHM systems can provide real-time data on the integrity of these materials, helping to ensure safety and reliability while reducing maintenance costs.

Several methods have been developed for SHM in composites, including strain gauge [90], optical fibre [91], and ultrasonic and vibration-based methods [92, 93, 94]. Strain gauge methods cover only small areas and require numerous gauges to monitor large structures, resulting in a complex system. Optical fibre methods, using embedded small-diameter fibres, offer the advantage of covering larger areas and being multiplexed for comprehensive monitoring. However, they face challenges such as shear-lag effects and potential initiation sites for cracks [95]. Ultrasonic methods, like A, B, and C-scans, are effective but typically require access to both sides of the structure, making them impractical for large components [96]. Vibration-based methods, includ-

ing modal response analysis and acoustic emission techniques, provide valuable data but are complex to interpret and often require extensive sensor networks [97].

2.2.3 SHM through fibre optics

The effectiveness of an SHM system largely depends on the sensors used to detect damage. Various types of sensors are employed in SHM systems, each with its strengths and limitations. Among these, Fibre Bragg Grating (FBG) sensors and distributed fibre optics are particularly notable for their applications in composite materials.

Fibre Bragg Grating sensors

FBG sensors are widely used in SHM systems due to their sensitivity and accuracy [98, 99, 100, 101]. These sensors reflect specific wavelengths of light, which shift in response to strain or temperature changes in the structure. This makes FBG sensors particularly useful for monitoring the internal strain of composite materials. They can be embedded within the composite during manufacturing or attached to the surface. FBG sensors are advantageous because they are lightweight, have a high bandwidth, and consume low power, making them suitable for aerospace applications. However, the implementation of FBG sensors requires careful consideration of the potential impact on the composite's structural integrity and the complexity of data interpretation. The fundamental principle behind the operation of an FBG is Fresnel reflection. The reflected wavelength, called the Bragg wavelength, is defined as

$$\lambda_B = 2n_{eff}\Lambda \tag{2.5}$$

where n_{eff} is the actual refractive exponent of centre fibre and Λ is the grating period. Here, n_{eff} and Λ both depend on the strain and temperature, so the

Bragg wavelength is sensitive to both of them. Fig.2.5 shows the structure of FBG with refractive index n, profile and spectral response P, where l is the fibre length.

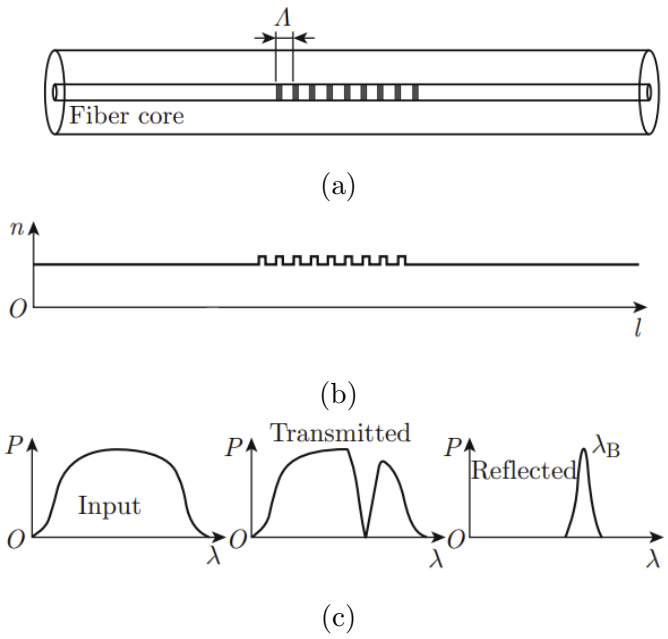

Figure 2.5: FBG structure with refractive index profile and spectral response: (a) Optical fibre; (b) Core refractive index; (c) Spectral response.

FBG sensors provide high-resolution strain measurements, which are crucial for detecting local deformations that could indicate the onset of damage. They are also immune to electromagnetic interference, making them ideal for use in harsh environments.

As to the measurement of deformation, the FBG central wavelength varies with the change of the parameters caused by the fibre. The relative Bragg wavelength shift $\Delta\lambda_B \backslash \lambda_B$, induced by longitudinal traction or compression of the fibre, can be computed by

$$\frac{\Delta\lambda_B}{\lambda_B} = \varepsilon_1 - \frac{n^2}{2}\left[p_{11}\varepsilon_t + p_{12}\left(\varepsilon_1 + \varepsilon_t\right)\right] \tag{2.6}$$

where ε_1 and ε_t are the longitudinal and transversal components of the deformation respectively, and p_{11} and p_{12} are the components of the photo-elastic tensor.

The data from FBG sensors can be integrated into SHM systems to create detailed maps of strain distribution, aiding in the early detection of structural issues. Despite these advantages, challenges such as the integration process and ensuring the durability of the sensors within the composite matrix need to be addressed.

Distributed fibre optics

Distributed fibre optic sensors, such as those based on Brillouin and Raman scattering [102], provide continuous strain or temperature measurements along the length of the fibre. Brillouin scattering is a phenomenon where light interacts with acoustic phonons in the fibre, causing a shift in the frequency of the scattered light. This frequency shift is related to the strain and temperature in the fibre. The Brillouin frequency shift ν_B can be expressed as,

$$\nu_B = \frac{2nv_A}{\lambda}, \tag{2.7}$$

where n is the refractive index of the fibre, v_A is the acoustic velocity in the fibre and γ is the wavelength of the incident light. Any changes in temperature or applying a deformation, affect the Brillouin frequency shift [103]. This relationship can be expressed as

$$\Delta\nu_B = C_\varepsilon\varepsilon + C_T\Delta T, \tag{2.8}$$

where C_ε and C_T are strain and temperature coefficients respectively. By measuring the Brillouin frequency shift along the fibre, distributed strain and temperature profiles can be obtained.

Raman scattering involves the inelastic scattering of light by optical phonons in the fibre. The intensity of the scattered light depends on the temperature of

the fibre. The Anti-Stokes I_{AS} and Stokes I_S components of Raman scattering are used to measure temperature changes. The ratio of these components is given by

$$\frac{I_{AS}}{I_S} = Ae^{\frac{-h\nu}{kT}}, \tag{2.9}$$

where A is a constant, h is Planck's constant, ν is the frequency of the incident light, k is Boltzmann's constant and T is the absolute temperature. By analysing the ratio of the Anti-Stokes to Stokes intensity, the temperature distribution along the fibre can be determined.

This capability allows for extensive coverage of large structures with a single fibre, making it a cost-effective solution for SHM [104, 105]. These sensors can detect changes in the material properties due to damage, providing valuable data for early damage detection. The distributed nature of these sensors means they can monitor entire structures rather than discrete points, offering a comprehensive view of the structural health.

Distributed fibre optics are particularly useful in detecting the progression of damage over time [106, 107, 108]. For example, Brillouin-based sensors measure strain and temperature by analysing frequency shifts in the scattered light, allowing for detailed monitoring over long distances. Raman-based sensors are similar but are often used for temperature measurements. These sensors are advantageous for covering large areas and providing detailed information about the structural state. However, they require sophisticated signal processing algorithms to interpret the data accurately, and the installation process must ensure that the fibres are well integrated into the structure without affecting its integrity [109, 110, 111].

2.2.4 Computational modelling for SHM

The integration of numerical models into SHM systems plays a crucial role in enhancing the accuracy and reliability of damage detection in composite structures. These models are indispensable for simulating the behaviour of materials under various conditions, predicting damage, and interpreting sensor data effectively [55, 112].

Importance of numerical models in SHM

Numerical models provide a comprehensive understanding of how composite materials behave under different loading scenarios, environmental conditions, and operational stresses. By simulating these conditions, it is possible to predict the initiation and progression of damage within a structure. This predictive ability is essential for developing targeted monitoring strategies and optimising the placement of sensors [113, 114, 115, 116, 117, 118].

Furthermore, numerical models enhance the interpretation of data collected from SHM sensors. They act as a reference, allowing for the comparison of real-time sensor data with simulated results to identify anomalies. This comparison helps in distinguishing between normal operational variations and actual structural damage, thereby improving the accuracy of damage detection and reducing false positives [119].

Additionally, numerical models are instrumental in the design and optimisation of SHM systems. By simulating various scenarios, engineers can test different sensor configurations and data analysis algorithms to identify the most effective setup for monitoring a particular structure. This process not only enhances the efficiency of SHM systems but also reduces development costs and time.

Development of numerical models for SHM

Developing numerical models for SHM involves several key steps. The process begins with the characterisation of the material properties of the composite structure [120]. This includes determining the mechanical properties, such as elasticity, strength, and fatigue behaviour, as well as the thermal and environmental properties that may affect the material's performance.

Next, the numerical model must incorporate various damage mechanisms relevant to composite materials, such as matrix cracking, fibre breakage, delamination, and debonding. These damage mechanisms can be modelled using FEM, continuum damage mechanics, or other techniques, as already discussed in *Section 2.1*.

Once the numerical model is developed, it is used to simulate the structural behaviour under different loading conditions. The simulated results are then validated against experimental data to ensure the accuracy and reliability of the model. This validation process may involve laboratory tests on composite specimens subjected to controlled loads and monitored with SHM sensors [121, 122, 123].

Finally, the validated numerical model is integrated with the SHM system to provide a reference for interpreting sensor data [124]. This integration may involve real-time data processing algorithms that compare sensor readings with the model's predictions, identify anomalies, and trigger alerts if damage is detected.

In conclusion, numerical models are a critical component of advanced SHM systems. They provide a detailed understanding of structural behaviour, enhance data interpretation, and enable predictive maintenance, thereby improving the safety, reliability, and cost-effectiveness of composite structures. As research and technology continue to evolve, the integration of numerical

models into SHM systems will undoubtedly become even more integral to the management and maintenance of composite materials in various high-stakes industries.

Chapter 3

CDM model for composite laminated plates

In this chapter, the theoretical formulation and the numerical implementation of a Ritz-CDM numerical model for the analysis of composite material is presented. Starting from the definition of the problem, the basic equations of the structural problem will be presented. Then, the CDM damage model used is described.

3.1 Problem statement

A quadrilateral laminated composite plate referred to a Cartesian coordinate system x_1, x_2, x_3, with the axis x_3 directed along the thickness h, is considered, as shown in Fig.(3.1). The reference mid-plane lies on the plane x_1 x_2 and is denoted by Ω while $\delta\Omega$ identifies its boundary.

The plate is assembled from N_{ply} VAT laminae, whose reinforcing fibres follow curved paths, thus exhibiting varying angles concerning the structural reference directions. Such fibre paths are described by specifying suitable laws for the fibre orientation θ. In this study, referring to Fig.(3.2), the following

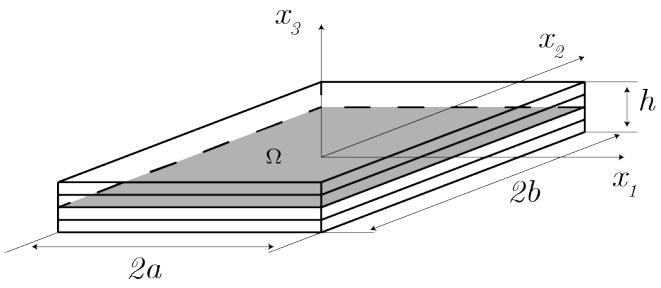

Figure 3.1: Schematic representation of multilayered composite plate.

law is used

$$\theta = \theta_0 + \frac{\theta_A r_B - \theta_B r_A}{r_B - r_A} + |r| \frac{\theta_B - \theta_A}{r_B - r_A} \tag{3.1}$$

where θ_0 is the angle between the baseline and the axis x_1, θ_A and θ_B measure the angle of the fibres at the points A and B, whilst r_A and r_B are the distances of these points from the projection O' of the plate centre on the baseline. Following the notation introduced by Gurdal *et al.* [8], point A is assumed to coincide with the projection of the centre point of the plate O' and $r_B = 2a$, so that the law that describes the fibre path of a lamina can be denoted as $\theta_0 + \langle \theta_A | \theta_B \rangle$.

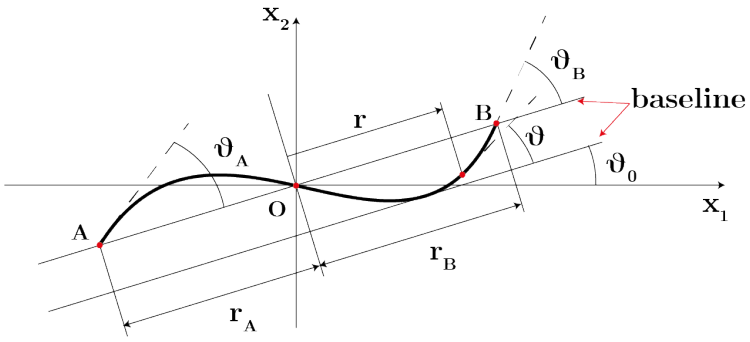

Figure 3.2: Geometric description of VAT lamina for fibre orientation definition.

To model general quadrilateral plates, a natural coordinate system $(\xi, \eta) \in [-1, 1] \times [-1, 1]$ is introduced, as in Fig.(3.3). The in-plane coordinates are

given by

$$x_i = \sum_{\alpha=1}^{4} g_\alpha(\xi, \eta) x_{i\alpha}, \qquad i = 1, 2 \tag{3.2}$$

where $x_{i\alpha}$ are the coordinates of the αth vertex of the plate mid-plane and g_α are the standard bi-linear shape functions, namely,

$$g_\alpha = \frac{(-1)^{\alpha-1}}{4}(\xi + \xi_\alpha)(\eta + \eta_\alpha), \qquad \alpha = 1, \ldots, 4 \tag{3.3}$$

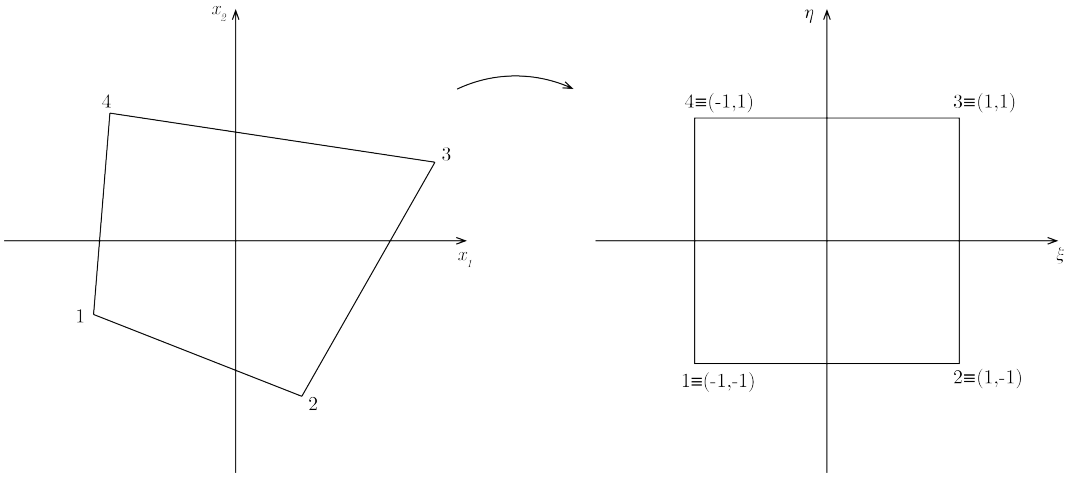

Figure 3.3: Plate mid-plane mapping: from the general quadrilateral domain in the x_1x_2 coordinate system to square domain $[-1;1] \times [-1;1]$ in $\xi\eta$ natural coordinate system.

3.2 Kinematic assumptions

In the present formulation, the plate kinematics is based on the *First-order shear deformation theory* (FSDT) [125]. Thus, the displacement vector components $\boldsymbol{d} = \{d_1, d_2, d_3\}^\intercal$ are given by

$$d_1 = u_1(x_1, x_2) + x_3\vartheta_1(x_1, x_2) \tag{3.4a}$$

$$d_2 = u_2(x_1, x_2) + x_3\vartheta_2(x_1, x_2) \tag{3.4b}$$

$$d_3 = u_3(x_1, x_2) + \overline{w}(x_1, x_2) \tag{3.4c}$$

where u_1 and u_2 are the mid-plane in-plane displacement components, u_3 is the mid-plane transverse deflection, ϑ_1 and ϑ_2 are the section rotations, and $\overline{w}$ is a prescribed initial displacements, which may describe the possible presence of geometrical plate imperfections. Eq. (3.4) can be compactly written as,

$$\boldsymbol{d} = \boldsymbol{u} + x_3 \boldsymbol{L}\boldsymbol{\vartheta} + \overline{\boldsymbol{w}} \tag{3.5}$$

where, $\boldsymbol{u} = \{u_1, u_2, u_3\}^\intercal$, $\boldsymbol{\vartheta} = \{\vartheta_1, \vartheta_2, \vartheta_3\}^\intercal$, $\overline{\boldsymbol{w}} = \{0, 0, \overline{w}\}^\intercal$ and

$$\boldsymbol{L} = \begin{bmatrix} 1 & 0 & 0 \\ 0 & 1 & 0 \\ 0 & 0 & 0 \end{bmatrix}. \tag{3.6}$$

It is worth noting that ϑ_3 is a "drilling" rotation that does not affect the plate deformation and it is used only to enforce the multi-domain interface continuity condition as described in Sec. (4.2.3).

The strain vector $\boldsymbol{e}$ is partitioned into in-plane and out-of-plane components, denoted by the subscripts p and n respectively,

$$\boldsymbol{e} = \{e_{11}, e_{22}, e_{12}, e_{13}, e_{23}, e_{33}\}^\intercal = \left\{ \begin{array}{c} \boldsymbol{e}_p \\ \\ \boldsymbol{e}_n \end{array} \right\}. \tag{3.7}$$

Admitting geometric non-linearity in the von Kármán sense, the strain displacement relationships may be written as

$$\begin{aligned} \boldsymbol{e}_p = \boldsymbol{\mathcal{D}}_p \boldsymbol{u} + \frac{1}{2} \left(\boldsymbol{\mathcal{D}}_p \otimes u_3\right) \boldsymbol{\mathcal{D}}_n \boldsymbol{u} + x_3 \boldsymbol{\mathcal{D}}_p \boldsymbol{L}\boldsymbol{\vartheta} + \left(\boldsymbol{\mathcal{D}}_p \otimes \overline{w}\right) \boldsymbol{\mathcal{D}}_n \boldsymbol{u} = \\ = \boldsymbol{\varepsilon}_p + \boldsymbol{\varepsilon}_{nl} + x_3 \boldsymbol{\kappa} + \bar{\boldsymbol{\varepsilon}} = \\ = \boldsymbol{\varepsilon} + x_3 \boldsymbol{\kappa} \end{aligned} \tag{3.8}$$

and

$$\boldsymbol{e}_n = \boldsymbol{\mathcal{D}}_n \boldsymbol{u} + \boldsymbol{L}\boldsymbol{\vartheta} = \boldsymbol{\gamma} \tag{3.9}$$

where $\boldsymbol{\mathcal{D}}_p$ and $\boldsymbol{\mathcal{D}}_n$ are matrix linear differential operators defined as

$$\boldsymbol{\mathcal{D}}_p = \begin{bmatrix} \partial_{x_1} & 0 & 0 \\ 0 & \partial_{x_2} & 0 \\ \partial_{x_2} & \partial_{x_1} & 0 \end{bmatrix} \qquad \boldsymbol{\mathcal{D}}_n = \begin{bmatrix} 0 & 0 & \partial_{x_1} \\ 0 & 0 & \partial_{x_2} \\ 0 & 0 & 0 \end{bmatrix} \tag{3.10}$$

with $\partial_{x_i} = \partial(\circ)/\partial x_i$. In Eqs.(3.8-3.9), the symbol $\otimes$ denotes the Kronecker product, while $\boldsymbol{\varepsilon}$, $\boldsymbol{\kappa}$ and $\boldsymbol{\gamma}$ denote the in-plane strains, curvatures and shear strains vectors, respectively; the subscript nl denotes non-linear terms induced by the von Kármán assumption.

3.3 Plate constitutive description in the presence of damage

In this section, the constitutive relations for VAT laminae are presented considering the possible presence of damage. Using the damage model developed by Matzenmiller et al. [39], the material stiffness coefficients are degraded by means of four damage indices, two associated with either tensile or compression loading along the fibre direction, namely ω_{ft} and ω_{fc} and two associated with either tensile or compression loading along the direction transversal to the fibres, i.e. ω_{mt} and ω_{mc}. On the other hand, it is worth underlining that the constitutive relations are written in the local material coordinate system and are a function of the in-plane coordinates, due to the variation of the in-plane fibre orientation $\theta(x_1, x_2)$ for a VAT lamina. This dependency is omitted in the subsequent equations for the sake of readability.

In the framework of CDM, employing the damage indices ω introduced above, one can obtain the relation between nominal in plane stress components, collected in $\tilde{\boldsymbol{\sigma}}_p$, and the effective stress components, collected in $\hat{\boldsymbol{\sigma}}_p$, as

$$\hat{\boldsymbol{\sigma}}_p = \boldsymbol{M}\tilde{\boldsymbol{\sigma}}_p, \tag{3.11}$$

where $\boldsymbol{M}$ is a damage operator defined as

$$\boldsymbol{M} = \begin{bmatrix} \frac{1}{1-\omega_1} & 0 & 0 \\ 0 & \frac{1}{1-\omega_2} & 0 \\ 0 & 0 & \frac{1}{1-\omega_6} \end{bmatrix}, \tag{3.12}$$

with ω_1, ω_2 and ω_6 being the longitudinal (fibre–dominated), transverse (matrix–dominated) and shear damage indices respectively, defined as

$$\omega_1 = \begin{cases} \omega_{ft} & \text{if} \quad \hat{\sigma}_{11} \geq 0 \\ \omega_{fc} & \text{if} \quad \hat{\sigma}_{11} < 0 \end{cases} \qquad \omega_2 = \begin{cases} \omega_{mt} & \text{if} \quad \hat{\sigma}_{22} \geq 0 \\ \omega_{mc} & \text{if} \quad \hat{\sigma}_{22} < 0 \end{cases} \tag{3.13}$$

and

$$\omega_6 = 1 - (1 - \omega_{ft})(1 - \omega_{fc})(1 - \omega_{mt})(1 - \omega_{mc}), \tag{3.14}$$

Each damage index ω_i can vary between 0, when no damage is present, and 1, when material failure takes place.

Using the definition in Eq.(3.11) with the stress-strain relations gives

$$\tilde{\boldsymbol{e}}_p = \boldsymbol{S}\hat{\boldsymbol{\sigma}}_p = \boldsymbol{S}\boldsymbol{M}\tilde{\boldsymbol{\sigma}}_p \tag{3.15}$$

where $\tilde{\boldsymbol{e}}_p$ collects the in-plane strain in the local material coordinate system and

$$\boldsymbol{S} = \begin{bmatrix} \frac{1}{E_1} & -\frac{\nu_{21}}{E_1} & 0 \\ -\frac{\nu_{12}}{E_2} & \frac{1}{E_2} & 0 \\ 0 & 0 & \frac{1}{G_{12}} \end{bmatrix} \tag{3.16}$$

is the compliance matrix, E_i is the Young's modulus, ν_{ij} are the Poisson's coefficients and G_{12} is the shear modulus. Defining the damage compliance tensor as

$$\hat{\boldsymbol{S}} = \boldsymbol{S}\boldsymbol{M} = \begin{bmatrix} \frac{1}{E_1(1-\omega_1)} & -\frac{\nu_{21}}{E_1} & 0 \\ -\frac{\nu_{12}}{E_2} & \frac{1}{E_2(1-\omega_2)} & 0 \\ 0 & 0 & \frac{1}{G_{12}(1-\omega_6)} \end{bmatrix}, \tag{3.17}$$

where the assumptions on the degradation of the Poisson ratio made by Matzenmiller et al. [39] have been adopted, and substituting in Eq.(3.15), one obtains the following constitutive relation

$$\tilde{\boldsymbol{\sigma}}_p = \hat{\boldsymbol{S}}^{-1}\tilde{\boldsymbol{e}}_p = \hat{\boldsymbol{C}}\tilde{\boldsymbol{e}}_p, \tag{3.18}$$

where $\hat{\boldsymbol{C}}$ is the stiffness matrix in presence of damage, explicitly given by

$$\hat{\boldsymbol{C}} = \frac{1}{D}\begin{bmatrix} (1-\omega_1)E_1 & (1-\omega_1)(1-\omega_2)\nu_{21}E_1 & 0 \\ (1-\omega_1)(1-\omega_2)\nu_{12}E_2 & (1-\omega_2)E_2 & 0 \\ 0 & 0 & D(1-\omega_6)G_{12} \end{bmatrix}, \tag{3.19}$$

with

$$D = 1-(1-\omega_1)(1-\omega_2)\nu_{12}\nu_{21}. \tag{3.20}$$

The plate constitutive equations may be obtained following the classical procedure given in Ref.[125] and read as

$$\begin{Bmatrix} \boldsymbol{N} \\ \boldsymbol{M} \\ \boldsymbol{T} \end{Bmatrix} = \begin{bmatrix} \boldsymbol{A} & \boldsymbol{B} & 0 \\ \boldsymbol{B} & \boldsymbol{D} & 0 \\ 0 & 0 & \boldsymbol{A}_s \end{bmatrix} \begin{Bmatrix} \boldsymbol{\varepsilon} \\ \boldsymbol{\kappa} \\ \boldsymbol{\gamma} \end{Bmatrix}, \tag{3.21}$$

where the membrane stress $\boldsymbol{N} = \{N_{11}, N_{22}, N_{12}\}^\intercal$, the moments per unit length $\boldsymbol{M} = \{M_{11}, M_{22}, M_{12}\}^\intercal$ and the transverse stress resultants $\boldsymbol{T} = \{T_{13}, T_{23}\}^\intercal$ are given by

$$\boldsymbol{N} = \int_{-h/2}^{h/2} \boldsymbol{\sigma}_p \, dx_3, \qquad \boldsymbol{M} = \int_{-h/2}^{h/2} \boldsymbol{\sigma}_p x_3 \, dx_3, \qquad \boldsymbol{T} = \int_{-h/2}^{h/2} K_s \boldsymbol{\sigma}_n \, dx_3, \tag{3.22}$$

where K_s is a shear correction factor, while the generalised stiffness matrices are

$$\begin{aligned} \boldsymbol{A} &= \sum_{k=1}^{N_{ply}} \int_{h_{k-1}}^{h_k} \boldsymbol{Q}_p^{\langle k \rangle}(\theta) \, dx_3 & \boldsymbol{B} &= \sum_{k=1}^{N_{ply}} \int_{h_{k-1}}^{h_k} x_3 \, \boldsymbol{Q}_p^{\langle k \rangle}(\theta) \, dx_3 \\ \boldsymbol{D} &= \sum_{k=1}^{N_{ply}} \int_{h_{k-1}}^{h_k} x_3^2 \, \boldsymbol{Q}_p^{\langle k \rangle}(\theta) \, dx_3 & \boldsymbol{A}_s &= \sum_{k=1}^{N_{ply}} \int_{h_{k-1}}^{h_k} \boldsymbol{Q}_n^{\langle k \rangle}(\theta) \, dx_3, \end{aligned} \tag{3.23}$$

where $\boldsymbol{Q}_p^{\langle k\rangle}(\theta) = \boldsymbol{L}_p(\theta)\,\hat{\boldsymbol{C}}^{\langle k\rangle}\boldsymbol{L}_p^{\intercal}(\theta)$ and $\boldsymbol{Q}_n^{\langle k\rangle}(\theta) = \boldsymbol{L}_n(\theta)\,\hat{\boldsymbol{C}}_n^{\langle k\rangle}\boldsymbol{L}_n^{\intercal}(\theta)$, for each *k-th* ply, contain ply stiffness coefficients that depend on the fiber orientation $\theta(x_1, x_2)$; the matrix $\hat{\boldsymbol{C}}^{\langle k\rangle}$ is defined in Eq.(3.19) and depends on the local damage level, the rotation matrices $\boldsymbol{L}_p$ and $\boldsymbol{L}_n$ contain the direction cosines and depend on the local fibre orientation $\theta(x_1, x_2)$ and the matrix $\boldsymbol{C}_n$ is given by

$$\boldsymbol{C}_n = \begin{bmatrix} G_{23} & 0 \\ 0 & G_{13} \end{bmatrix}. \tag{3.24}$$

3.3.1 Damage onset and evolution

In the present work, the damage analysis is based on a material degradation model. After an activation threshold is overcome, the corresponding damage index starts evolving according to an evolution law, thus inducing strain softening in the constitutive material response.

Damage onset is tracked in the framework of Hashin's theory [126, 127], which considers four different activation criteria along the fibres and matrix-dominated transverse directions under either tensile or compression loading. They are defined as follows.

Fibre tension:

$$F_{ft} = \left(\frac{\hat{\sigma}_{11}}{X_T}\right)^2 = 1 \tag{3.25a}$$

Fibre compression:

$$F_{fc} = \left(\frac{\hat{\sigma}_{11}}{X_C}\right)^2 = 1 \tag{3.25b}$$

Matrix tension:

$$F_{mt} = \left(\frac{\hat{\sigma}_{22}}{Y_T}\right)^2 + \left(\frac{\hat{\sigma}_{12}}{S_L}\right)^2 = 1 \tag{3.25c}$$

Matrix compression:

$$F_{mc} = \left(\frac{\hat{\sigma}_{22}}{2S_L}\right)^2 + \left[\left(\frac{Y_C}{2S_T}\right)^2 - 1\right]\frac{\hat{\sigma}_{22}}{Y_C} + \left(\frac{\hat{\sigma}_{12}}{S_L}\right)^2 = 1 \tag{3.25d}$$

In Eqs.(3.25), $\hat{\sigma}_{ij}$ are the components of the stress tensor computed from Eq.(3.11) and X_T, X_C , Y_T ,Y_C, S_L, S_T are the ply strengths associated with each loading mode and direction. The shear transverse strength S_T, if is not available, can be computed as $S_T = 0.5Y_C$ [126].

Following the onset of damage, further increases of the effective loads generally result in the evolution of the activated damage indices and thus in the the degradation of the material properties associated with them. Referring to a linear softening law, as schematically shown in Fig.(3.4), upon defining the following *equivalent strains* for each loading/damage mode

$$\textit{Fibers} \quad \begin{cases} e_{ft,eq} = \langle e_{11} \rangle \\ e_{fc,eq} = \langle -e_{11} \rangle \end{cases} \qquad \textit{Matrix} \quad \begin{cases} e_{mt,eq} = \sqrt{\langle e_{22} \rangle^2 + e_{12}^2} \\ e_{mc,eq} = \sqrt{\langle -e_{22} \rangle^2 + e_{12}^2} \end{cases} \tag{3.26}$$

where $\langle \circ \rangle = (\circ + | \circ |)/2$ denotes the Macaulay brackets, the current value of the *i-th* damage index can be computed considering the evolution, during the loading process, of the quantities

$$\omega_i(\tau) = \frac{e_{i,eq}^f \left(e_{i,eq} - e_{i,eq}^0 \right)}{e_{i,eq} \left(e_{i,eq}^f - e_{i,eq}^0 \right)}, \qquad i = ft, fc, mt, mc, \tag{3.27}$$

where τ denotes a generic loading/time ordering parameter spanning the loading history $\mathscr{H}$, $e_{i,eq}^0$ is the equivalent strain at the onset of damage and $e_{i,eq}^f = \alpha_i \, e_{i,eq}^0$ is the equivalent strain at rupture; in particular, to ensure a monotonically increasing evolution, the current value of the *i-th* damage index is defined as

$$\omega_i = \max\{0, \max_{\tau \in \mathscr{H}} \{\omega_i(\tau)\}\}. \tag{3.28}$$

It is worth noting that, in general, different values of damage are associated with tensile or compression loading, which means that, for example, two different values of ω_1 are defined with respect to the fibres direction at

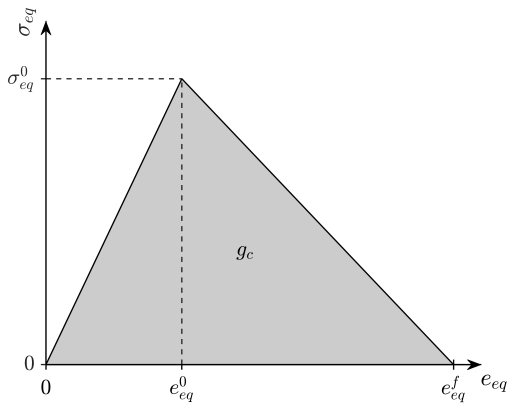

Figure 3.4: Adopted stress-strain softening curve.

a given material point, and Eq.(3.28) must be updated distinguishing tensile form compression loading, see e.g. Ref.[43].

In Eq.(3.27), the strain at rupture $e^f_{i,eq}$ can be computed from the knowledge of the material fracture toughness G_c [80, 128]. To ensure that the fracture toughness remains constant, $e^f_{i,eq}$ must be adjusted introducing a discretization dependent length L_c, which modifies the shape of the strain-softening curve linking it to the size of the discretization itself, see e.g. Refs.[129, 130]. In Fig.(3.4), the area under the stress-strain curve

$$g_c = \int_0^{e^f_{eq}} \sigma_{eq} de_{eq} \tag{3.29}$$

corresponds to the energy dissipated at failure per unit volume. Defining the *equivalent displacement* as $\delta_{eq} = e_{eq} L_c$, the fracture energy dissipated per unit area can be written as

$$G_c = g_c L_c = \int_0^{\delta^f_{eq}} \sigma_{eq} d\delta_{eq}. \tag{3.30}$$

Considering that the fracture energy G_c is a known material property, $e^f_{i,eq}$ can be eventually computed as

$$e^f_{i,eq} = \frac{2G_c}{\sigma^0_{eq} L_c}. \tag{3.31}$$

While in finite element models L_c is directly linked to the mesh size, in the proposed Ritz scheme

$$L_c = \sqrt{\frac{S}{M_\chi N_\chi}} \tag{3.32}$$

where S is the area of the discretized domain, whilst M_χ and N_χ are the maximum degrees of the polynomial Ritz approximation scheme, which will be further discussed in the subsequent section. Alternatively, as proposed in Refs.[131, 132] it is possible to provide the equivalent strain ratio α_i as an input parameter.

Chapter 4

A novel CDM-Ritz computational scheme

Considering the non-linear evolution of damage under progressive loading, the solution of the considered mechanical problem requires the implementation of an incremental-iterative approach, which will be described in this chapter. The discrete governing equations at a given load step can however be obtained by stating the stationarity of the plate's total potential energy and employing the plate kinematics assumptions, the constitutive equations and the Ritz approximation of the kinematic primary variables. Once the discrete equations are available, the adoption of a suitable incremental-iterative scheme allows for capturing the evolving damage and the associated variation of the structure stiffness coefficients. The overall procedure is described in the following sections.

4.1 Problem variational statement

At a given load level, the discrete governing equations can be written starting from the statement of stationarity of the structure total potential energy

$$\delta\Pi = \delta U + \delta V = 0 \tag{4.1}$$

where U is the internal energy and V is the work done by the external forces.

Considering the plate kinematics and constitutive relations given in the above sections, the internal energy U may be written as

$$U = \frac{1}{2}\int_{\Omega}\sum_{k=1}^{N_{ply}}\left\{\int_{h_{k-1}}^{h_k}\left(\boldsymbol{e}_p^{\intercal}\boldsymbol{\sigma}_p + \boldsymbol{e}_n^{\intercal}\boldsymbol{\sigma}_n\right)dx_3\right\}d\Omega =$$

$$= \frac{1}{2}\int_{\Omega}\sum_{k=1}^{N_{ply}}\left\{\int_{h_{k-1}}^{h_k}\left[\left(\boldsymbol{\varepsilon}^{\intercal} + x_3\boldsymbol{\kappa}^{\intercal}\right)\boldsymbol{Q}_p^{\langle k\rangle}\left(\boldsymbol{\varepsilon} + x_3\boldsymbol{\kappa}\right) + \boldsymbol{\gamma}^{\intercal}\boldsymbol{Q}_n^{\langle k\rangle}\boldsymbol{\gamma}\right]dx_3\right\}d\Omega \tag{4.2}$$

while the external work is given by

$$V = -\int_{\Omega}(\boldsymbol{u}^{\intercal}\boldsymbol{q} + \boldsymbol{\vartheta}^{\intercal}\boldsymbol{m})d\Omega - \int_{\partial\Omega}\left(\boldsymbol{u}^{\intercal}\,\overline{\boldsymbol{N}} + \boldsymbol{\vartheta}^{\intercal}\,\overline{\boldsymbol{M}}\right)d\partial\Omega \tag{4.3}$$

where $\boldsymbol{q} = \{q_1, q_2, q_3\}^{\intercal}$ and $\boldsymbol{m} = \{m_1, m_2, 0\}^{\intercal}$ are the external forces and external moments per unit area applied over the domain Ω, whereas $\overline{\boldsymbol{N}}$ and $\overline{\boldsymbol{M}}$ denote prescribed forces and moments applied on the plate boundary $\partial\Omega_l \subset \partial\Omega$. The plate essential boundary conditions are provided by prescribing the generalized displacements on the boundary $\partial\Omega_c$ as follows

$$\begin{aligned}\boldsymbol{\Xi}_u\boldsymbol{u} &= \boldsymbol{\Xi}_u\,\overline{\boldsymbol{u}} \quad \text{on } \partial\Omega_c\\ \boldsymbol{\Xi}_\vartheta\boldsymbol{\vartheta} &= \boldsymbol{\Xi}_\vartheta\,\overline{\boldsymbol{\vartheta}} \quad \text{on } \partial\Omega_c\end{aligned} \tag{4.4}$$

where $\boldsymbol{\Xi}_u$ and $\boldsymbol{\Xi}_\vartheta$ are boolean matrix operator used for selecting the desired constrained generalized displacements whereas the over-bar denotes prescribed quantities.

4.2 Ritz solution scheme

Once the plate governing equations – Eqs.(4.1) - (4.2) - (4.3) – have been written, their discrete form can be built using the Ritz approximation scheme developed e.g. in Refs.[22, 23]. The main items of the solution procedure are outlined in this section.

4.2.1 Ritz polynomial approximation

The Ritz scheme expresses the components of the generalized displacements appearing in Eqs.(4.1) - (4.2) as

$$\chi = \sum_{m=1}^{M_\chi} \sum_{n=1}^{N_\chi} \psi_m(\xi)\, \psi_n(\eta)\, C_{\chi_{(m-1)M+n}} = \boldsymbol{\Psi}_\chi \boldsymbol{C}_\chi \tag{4.5}$$

where $\chi \in \{u_1, u_2, u_3, \vartheta_1, \vartheta_2\}$ is the generic component of displacement, $\psi_m(\xi)$ and $\psi_n(\eta)$ are the trial function of order m or n and $C_{\chi_{(m-1)M+n}}$ are the unknown Ritz coefficients. In this work, among other possible choices, Legendre orthogonal polynomials

$$\psi_n(\zeta) = \frac{1}{2^n n!} \frac{d^n}{d\zeta^n} \left[\left(\zeta^2 - 1\right)^n \right], \tag{4.6}$$

have been selected as trial functions $\psi_m(\xi)$ and $\psi_n(\eta)$, as they proved effective in plate problems [133].

Eq.(4.5) can be specialized to the plate primary variables $\boldsymbol{u}$ and $\boldsymbol{\vartheta}$ and written in compact matrix form as

$$\boldsymbol{u} = \begin{bmatrix} \boldsymbol{\Psi}_{\boldsymbol{u_1}} & 0 & 0 \\ 0 & \boldsymbol{\Psi}_{\boldsymbol{u_2}} & 0 \\ 0 & 0 & \boldsymbol{\Psi}_{\boldsymbol{u_3}} \end{bmatrix} \begin{Bmatrix} \boldsymbol{C}_{u_1} \\ \boldsymbol{C}_{u_2} \\ \boldsymbol{C}_{u_3} \end{Bmatrix} = \begin{bmatrix} \boldsymbol{\Phi}_{u_1} \\ \boldsymbol{\Phi}_{u_2} \\ \boldsymbol{\Phi}_{u_3} \end{bmatrix} \boldsymbol{U} = \boldsymbol{\Phi}_u \boldsymbol{U} \tag{4.7}$$

and

$$\boldsymbol{\vartheta} = \begin{bmatrix} \boldsymbol{\Psi}_{\boldsymbol{\vartheta_1}} & 0 & 0 \\ 0 & \boldsymbol{\Psi}_{\boldsymbol{\vartheta_2}} & 0 \\ 0 & 0 & \boldsymbol{\Psi}_{\boldsymbol{\vartheta_3}} \end{bmatrix} \begin{Bmatrix} \boldsymbol{C}_{\vartheta_1} \\ \boldsymbol{C}_{\vartheta_2} \\ \boldsymbol{C}_{\vartheta_3} \end{Bmatrix} = \begin{bmatrix} \boldsymbol{\Phi}_{\vartheta_1} \\ \boldsymbol{\Phi}_{\vartheta_2} \\ \boldsymbol{\Phi}_{\vartheta_3} \end{bmatrix} \boldsymbol{\Theta} = \boldsymbol{\Phi}_\vartheta \boldsymbol{\Theta}. \tag{4.8}$$

Using the above equations, the in-plane strains vector $\boldsymbol{\varepsilon}$, the curvatures vector $\boldsymbol{\kappa}$ and the shear strains vector $\boldsymbol{\gamma}$ can be written as

$$\begin{aligned} \boldsymbol{\varepsilon} &= \boldsymbol{\mathcal{B}}_{pU}\boldsymbol{U} + \frac{1}{2}\boldsymbol{\mathcal{B}}_{nlU}\boldsymbol{U} + \bar{\boldsymbol{\mathcal{B}}}_{nlU}\boldsymbol{U}, \\ \boldsymbol{\kappa} &= \boldsymbol{\mathcal{B}}_{p\Theta}\boldsymbol{\Theta}, \qquad \boldsymbol{\gamma} = \boldsymbol{\mathcal{B}}_{nU}\boldsymbol{U} + \boldsymbol{\mathcal{B}}_{i\Theta}\boldsymbol{\Theta} \end{aligned} \tag{4.9}$$

where the operators $\boldsymbol{\mathcal{B}}$ are given by

$$\begin{aligned} \boldsymbol{\mathcal{B}}_{pU} &= \boldsymbol{\mathcal{D}}_p\boldsymbol{\Phi}_u & & \\ \boldsymbol{\mathcal{B}}_{nU} &= \boldsymbol{\mathcal{D}}_n\boldsymbol{\Phi}_u & \bar{\boldsymbol{\mathcal{B}}}_{nlU} &= [\boldsymbol{\mathcal{D}}_p \otimes \overline{w}]\,\boldsymbol{\mathcal{D}}_n\boldsymbol{\Phi}_u \\ \boldsymbol{\mathcal{B}}_{p\Theta} &= \boldsymbol{\mathcal{D}}_p\boldsymbol{\Phi}_\vartheta & \boldsymbol{\mathcal{B}}_{nlU} &= [\boldsymbol{\mathcal{D}}_p \otimes (\boldsymbol{\Phi}_{u_3}\boldsymbol{U})]\,\boldsymbol{\mathcal{D}}_n\boldsymbol{\Phi}_u \\ \boldsymbol{\mathcal{B}}_{i\Theta} &= \boldsymbol{\Phi}_\vartheta & & \end{aligned} \tag{4.10}$$

4.2.2 Discrete equations and incremental solution

By considering Eqs.(4.7-4.8) and employing a penalty approach to enforce the essential boundary conditions, the stationarity condition $\delta\Pi = 0$ with respect to $\boldsymbol{U}$ and $\boldsymbol{\Theta}$ leads to the discrete system

$$\begin{aligned} &\int_\Omega \left[\left(\boldsymbol{\mathcal{B}}_{pU} + \boldsymbol{\mathcal{B}}_{nlU} + \bar{\boldsymbol{\mathcal{B}}}_{nlU}\right)^\intercal \boldsymbol{A} \left(\boldsymbol{\mathcal{B}}_{pU} + \frac{1}{2}\boldsymbol{\mathcal{B}}_{nlU} + \bar{\boldsymbol{\mathcal{B}}}_{nlU}\right) + \boldsymbol{\mathcal{B}}_{nU}^\intercal \boldsymbol{A}_s \boldsymbol{\mathcal{B}}_{nU} \right] \boldsymbol{U} d\Omega + \\ &\quad + \int_\Omega \left[\left(\boldsymbol{\mathcal{B}}_{pU} + \boldsymbol{\mathcal{B}}_{nlU} + \bar{\boldsymbol{\mathcal{B}}}_{nlU}\right)^\intercal \boldsymbol{B}\boldsymbol{\mathcal{B}}_{p\Theta} + \boldsymbol{\mathcal{B}}_{nU}^\intercal \boldsymbol{A}_s \boldsymbol{\mathcal{B}}_{i\Theta} \right] \boldsymbol{\Theta} d\Omega + \\ &\quad + \int_\Omega \left[\boldsymbol{\mathcal{B}}_{p\Theta}^\intercal \boldsymbol{B} \left(\boldsymbol{\mathcal{B}}_{pU} + \frac{1}{2}\boldsymbol{\mathcal{B}}_{nlU} + \bar{\boldsymbol{\mathcal{B}}}_{nlU}\right) + \boldsymbol{\mathcal{B}}_{i\Theta}^\intercal \boldsymbol{A}_s \boldsymbol{\mathcal{B}}_{nU} \right] \boldsymbol{U} d\Omega + \\ &\quad + \int_\Omega \left(\boldsymbol{\mathcal{B}}_{p\Theta}^\intercal \boldsymbol{D}\boldsymbol{\mathcal{B}}_{p\Theta} + \boldsymbol{\mathcal{B}}_{i\Theta}^\intercal \boldsymbol{A}_s \boldsymbol{\mathcal{B}}_{i\Theta} \right) \boldsymbol{\Theta} d\Omega + \\ &\quad + \int_{\partial\Omega_c} \left(\boldsymbol{\Phi}_u^\intercal \boldsymbol{\Xi}_u^\intercal \boldsymbol{\omega}_u \boldsymbol{\Xi}_u \boldsymbol{\Phi}_u \boldsymbol{U} + \boldsymbol{\Phi}_\vartheta^\intercal \boldsymbol{\Xi}_\vartheta^\intercal \boldsymbol{\omega}_\vartheta \boldsymbol{\Xi}_\vartheta \boldsymbol{\Phi}_\vartheta \boldsymbol{\Theta} \right) d\partial\Omega + \\ &\quad = \int_\Omega \left(\boldsymbol{\Phi}_u^\intercal \boldsymbol{q} + \boldsymbol{\Phi}_\vartheta^\intercal \boldsymbol{m} \right) d\Omega + \int_{\partial\Omega_l} \left(\boldsymbol{\Phi}_u^\intercal\, \overline{\boldsymbol{N}} + \boldsymbol{\Phi}_\vartheta^\intercal\, \overline{\boldsymbol{M}} \right) d\partial\Omega + \\ &\quad + \int_{\partial\Omega_c} \left(\boldsymbol{\Phi}_u^\intercal \boldsymbol{\Xi}_u^\intercal \boldsymbol{\omega}_u \boldsymbol{\Xi}_u \boldsymbol{\Phi}_u\, \overline{\boldsymbol{u}} + \boldsymbol{\Phi}_\vartheta^\intercal \boldsymbol{\Xi}_\vartheta^\intercal \boldsymbol{\omega}_\vartheta \boldsymbol{\Xi}_\vartheta \boldsymbol{\Phi}_\vartheta\, \overline{\boldsymbol{\vartheta}} \right) d\partial\Omega, \end{aligned} \tag{4.11}$$

which may be written in compact form as

$$\left(\boldsymbol{K}_0 + \overline{\boldsymbol{K}}_0 + \boldsymbol{K}_1 + \boldsymbol{K}_2 + \overline{\boldsymbol{K}}_1 + \boldsymbol{R}\right)\boldsymbol{X} = \boldsymbol{F}_D + \boldsymbol{F}_L \tag{4.12}$$

where $\boldsymbol{X} = \{\boldsymbol{U}, \boldsymbol{\Theta}\}^{\intercal}$ is the vector collecting the unknown coefficients of the Ritz series expansion, $\boldsymbol{K}_0$, $\boldsymbol{K}_1$, $\boldsymbol{K}_2$, $\overline{\boldsymbol{K}}_0$, $\overline{\boldsymbol{K}}_1$ are the stiffness matrices in which the subscripts 1,2 refer to the geometric non-linear terms and the over-bar refers to the prescribed initial imperfections, while $\boldsymbol{R}$ is the matrix originating from the enforcement of the BCs thorough a penalty approach. On the right hand-side, the vectors $\boldsymbol{F}_D$ and $\boldsymbol{F}_L$ collect the discrete terms associated with the external loads. Details on the matrices appearing in Eq.(4.12) are given in Appendix A.

To solve the non-linear problem given in Eq.(4.12), an incremental-iterative procedure is employed.

It is important to observe that the local stiffness of the laminate layers, and thus all the matrices on the left hand-side of Eq.(4.12), except $\boldsymbol{R}$, are affected by the damage level $\boldsymbol{\omega}[\mathscr{H}(\boldsymbol{X})]$. The vector $\boldsymbol{\omega}[\mathscr{H}(\boldsymbol{X})]$, which collects the damage indices, plays the role of an internal state vector that depends on the loading/solution history $\mathscr{H}(\boldsymbol{X})$. As a consequence, the incremental form of Eq.(4.12) may be expressed as

$$\boldsymbol{R}\,\Delta\boldsymbol{X} + \Delta\left[\left(\boldsymbol{K}_0 + \overline{\boldsymbol{K}}_0 + \boldsymbol{K}_1 + \boldsymbol{K}_2 + \overline{\boldsymbol{K}}_1\right)\boldsymbol{X}\right] = \Delta\boldsymbol{F}_D + \Delta\boldsymbol{F}_L \tag{4.13}$$

with

$$\Delta\left[\left(\boldsymbol{K}_0 + \overline{\boldsymbol{K}}_0 + \boldsymbol{K}_1 + \boldsymbol{K}_2 + \overline{\boldsymbol{K}}_1\right)\boldsymbol{X}\right] = \left(\boldsymbol{K}_{t,geo} + \boldsymbol{K}_{t,dmg}\right)\Delta\boldsymbol{X}, \tag{4.14}$$

where $\Delta\,(\circ)$ is the incremental operator, $\boldsymbol{K}_{t,geo}$ is the tangent stiffness matrix contribution related to the geometric non-linearity and the initial imperfections, whilst $\boldsymbol{K}_{t,dmg}$ is the tangent stiffness matrix contribution related to the

damage evolution. Further details about such matrices are reported in Appendix B.

4.2.3 Multi-domain Ritz model: sub-domains continuity conditions

As mentioned in the *Introduction*, the direct application of a Ritz approximation to problems involving a hard discontinuity, e.g. a damage localisation or crack, gives rise to artefacts induced by the unavoidable presence of Gibbs effects. This issue, which will be further highlighted and investigated in the numerical tests, has called for the development of mitigation strategies able to ensure the objectivity of the response upon damage localisation. Among various strategies, an adaptive subdivision of the Ritz analysis domain into smaller subdomains, over which hierarchical variable order Ritz approximations are further adopted, has proved one of the most promising in contrasting the observed issue. The subdivision scheme is here described, together with the method used to transfer the information from a parent domain to its children ones, and it will be further discussed in the subsequent sections. For the sake of readability, the governing equations presented in Eq. (4.12) are written considering small-strain assumptions:

$$(\boldsymbol{K}_0 + \boldsymbol{R})\,\boldsymbol{X} = \boldsymbol{F}_D + \boldsymbol{F}_L, \tag{4.15}$$

thus not considering all the matrices that account for geometric non-linearities.

Consider the original plate subdivided into N_{el} quadrilateral sub-domains; the quantities associated with such sub-domains are denoted by the superscript $\langle t \rangle$. Each separate sub-domain $\langle t \rangle$ is mapped into its corresponding natural coordinate system and is associated with its governing equations provided in Eq. (4.12). Let Γ_{pq} denote the edge shared between two contiguous sub-domains

$\langle p \rangle$ and $\langle q \rangle$: the integrity of the domain requires displacement continuity and traction equilibrium along Γ_{pq}.

The displacement continuity on Γ_{pq} requires that: *i*) the modelling plane translations of the two contiguous sub-domains have equal components in the global reference system $x_1 x_2 x_3$; *ii*) the rotations around the global axes x_i of the two contiguous sub-domains are equal. These considerations give

$$\boldsymbol{\Lambda}_u^{\langle p \rangle} \boldsymbol{u}^{\langle p \rangle} = \boldsymbol{\Lambda}_u^{\langle q \rangle} \boldsymbol{u}^{\langle q \rangle} \qquad \text{on } \Gamma_{pq} \tag{4.16a}$$

$$\boldsymbol{\Lambda}_\vartheta^{\langle p \rangle} \boldsymbol{\vartheta}^{\langle p \rangle} = \boldsymbol{\Lambda}_\vartheta^{\langle q \rangle} \boldsymbol{\vartheta}^{\langle q \rangle} \qquad \text{on } \Gamma_{pq} \tag{4.16b}$$

where $\boldsymbol{\Lambda}_\alpha^{\langle r \rangle}$ are suitable transformation matrices from the local to the global reference systems. It is worth noting that the introduction of the drilling rotation θ_3 does not affect the plate displacements but it allows to generalise the rotation continuity condition through Eq.(4.16b), see e.g. Ref.[134].

On the other hand, the traction equilibrium is enforced in terms of resultant forces and moments along Γ_{pq}, written as

$$\boldsymbol{\Lambda}_u^{\langle p \rangle} \tilde{\boldsymbol{N}}^{\langle p \rangle} + \boldsymbol{\Lambda}_u^{\langle q \rangle} \tilde{\boldsymbol{N}}^{\langle q \rangle} = \boldsymbol{0} \tag{4.17a}$$

$$\boldsymbol{\Lambda}_\vartheta^{\langle p \rangle} \tilde{\boldsymbol{M}}^{\langle p \rangle} + \boldsymbol{\Lambda}_\vartheta^{\langle q \rangle} \tilde{\boldsymbol{M}}^{\langle q \rangle} = \boldsymbol{0} \tag{4.17b}$$

The overall set of discrete equations, considering the subdivision of the original domain into sub-domains, is then obtained by applying the variational formulation and Ritz approximation scheme to all the sub-domains, and enforcing the boundary and continuity conditions expressed in Eq.(4.16) through suitable penalty terms, see e.g. Ref.[135]. Therefore, the resolving system of equations, for $t = 1 \dots N_{el}$ is

$$\left(\boldsymbol{K}_0^{\langle t \rangle} + \boldsymbol{R}^{\langle t \rangle} + \sum_{\substack{r=1 \\ r \neq t}}^{N_{el}} \boldsymbol{P}_{rt}^{\langle t,t \rangle} \right) \boldsymbol{X}^{\langle t \rangle} - \sum_{\substack{r=1 \\ r \neq t}}^{N_{el}} \boldsymbol{P}_{rt}^{\langle t,r \rangle} \boldsymbol{X}^{\langle r \rangle} = \boldsymbol{F}_D^{\langle t \rangle} + \boldsymbol{F}_L^{\langle t \rangle}, \tag{4.18}$$

where the matrices $\boldsymbol{P}_{rt}^{\langle .,. \rangle}$, explicitly given in Appendix A, are introduced to properly describe the connection between sub-domains.

The incremental form associated with Eq.(4.18) is eventually given by

$$\left[\boldsymbol{R}^{\langle t \rangle} + \sum_{\substack{r=1 \\ r \neq t}}^{N_{el}} \boldsymbol{P}_{rt}^{\langle t,t \rangle}\right] \Delta \boldsymbol{X}^{\langle t \rangle} - \left[\sum_{\substack{r=1 \\ r \neq t}}^{N_{el}} \boldsymbol{P}_{rt}^{\langle t,r \rangle}\right] \Delta \boldsymbol{X}^{\langle r \rangle} + \Delta \left[\boldsymbol{K}_0^{\langle t \rangle} \boldsymbol{X}^{\langle t \rangle}\right] = \Delta \boldsymbol{F}_D^{\langle t \rangle} + \Delta \boldsymbol{F}_L^{\langle t \rangle} \tag{4.19}$$

for $t = 1 \dots N_{el}$.

4.3 Implementation details

The proposed model has been implemented using MATLAB® [136].

In this study, the nonlinear damage evolution problem is solved by employing an incremental-iterative Newton-Raphson scheme in displacement control. Once the solution at a given load step is obtained, a load increment is enforced, and the Newton-Raphson iteration is started, triggering the non-linear evolution of the internal damage variables; the process is arrested when the residual is reduced below a preset tolerance, so that a subsequent increment, if of interest, may be applied. A block diagram describing the most relevant phases of the implemented model is reported in Fig.(4.1).

Some remarks about how the adaptive multi-domain procedure works are herein reported. All the subdomains are initially flagged as *undamaged*, unless some *a priori* damage is considered. If, upon load increment, the failure criteria are met in an undamaged sub-domain, then the adaptive procedure is activated. Hence, the program steps back to the previous converged solution and subdivides the considered sub-domain, which is going to feature damage initiation, into a collection of patches. It is worth mentioning an important constrain that must be considered in the subdivision process: the stress-strain diagram must not present snap-back that may arise after the computation of

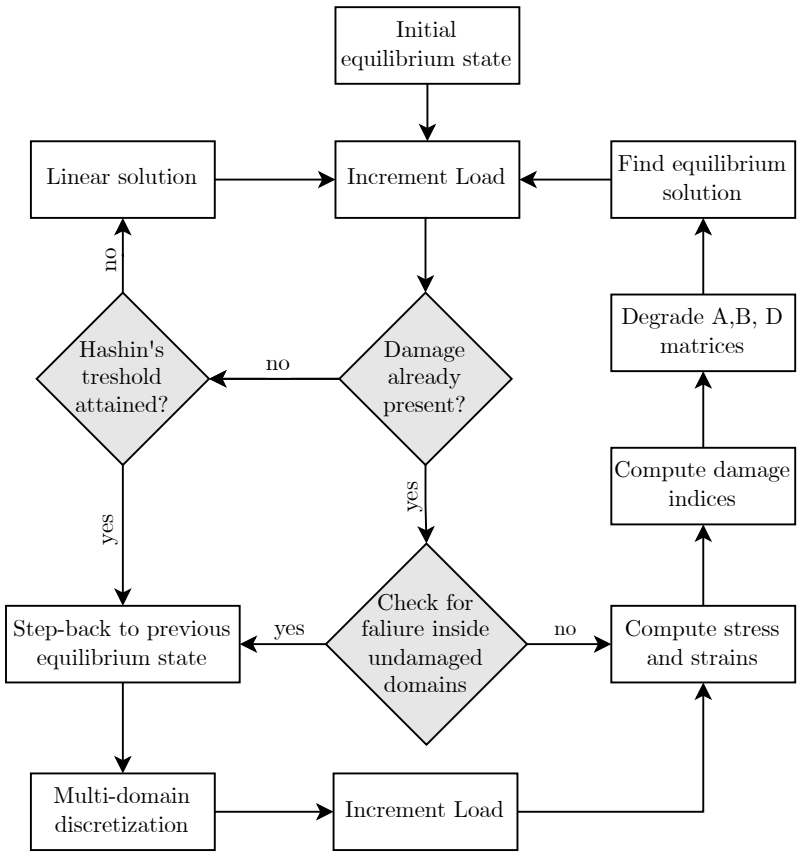

Figure 4.1: Block diagram representing the phases of the adaptive Ritz damage model.

$e^f_{i,eq}$ in Eq.(3.31). To ensure that, the maximum size for the new sub-domains in which damage can spread is:

$$L_c \leq \frac{2E_i G_{c,i}}{X_i} \qquad i = ft, fc, mt, mc, \tag{4.20}$$

where E_i, $G_{c,i}$ and X_i are the Young modulus, fracture energies and strengths associated with their corresponding damage modes, respectively. This is consistent with what often done in CDM approaches, see e.g. [80, 81]. Those new sub-domains are still flagged as undamaged, except those within which the damage threshold will be overcome by re-applying the load increment.

To transfer the fields information from the last converged state, involving

a certain set of domains, to the new subdivided domains, a least square procedure is employed. Therefore, after computing and assembling the stiffness and penalty matrices, the solution vector of the new discretization X_m is computed by equating the displacement field of the previous discretization and the multi-domain discretization of the available converged solution,

$$\boldsymbol{u}(x_1, x_2) = \tilde{\boldsymbol{u}}(x_1, x_2) = \boldsymbol{\Phi}(x_1, x_2)\boldsymbol{X} = \tilde{\boldsymbol{\Phi}}(x_1, x_2)\boldsymbol{X}_m \tag{4.21}$$

where $\tilde{\boldsymbol{u}}$ and $\tilde{\boldsymbol{\Phi}}(x_1, x_2)$ are respectively the displacements and the matrix of polynomials associated with the new discretization. The solution vector $\boldsymbol{X}_m$ is then obtained by minimising not only $||\tilde{\boldsymbol{\Phi}}(x_1, x_2)\boldsymbol{X}_m - \boldsymbol{\Phi}(x_1, x_2)\boldsymbol{X}||$ but also $||\boldsymbol{X}_m||$ [137].

Finally, it is worth highlighting an important implementation feature before presenting the validation and numerical result; convergence issues are frequent and well-known in material models that show softening and stiffness loss. In this study, a viscous regularisation approach is used as mentioned in Ref.[41], to mitigate such numerical convergence issues. The following evolution equation is then introduced

$$\dot{\omega}_i^v = \frac{1}{\beta}\left(\omega_i - \omega_i^v\right) \tag{4.22}$$

where β is a *viscous parameter* and ω_i^v denotes the regularised damaged variable for the *i-th* damage mode, computed as

$$\omega_i^v|_n = \frac{\Delta\tau}{\beta + \Delta\tau}\omega_i|_n + \frac{\beta}{\beta + \tau}\omega_i^v|_{n-1}, \tag{4.23}$$

where, the subscripts $n-1$ and n denote two subsequent time/load steps, and $\Delta\tau$ is the interval between them, while τ is the time/load parameter.

It has been demonstrated that, when the viscosity parameter β is small compared to $\Delta\tau$, the viscous regularisation scheme improves the rate of convergence without significantly affecting the accuracy of the results. Therefore, for all applications shown in the numerical result sections the value of $\beta = 1 \times 10^{-5}$ has been chosen.

Chapter 5

Performed experimental tests

Six months have been spent at the Italian Centre of Aerospace Research, to conduct experimental tests on thermoplastic composite coupons equipped with various types of sensors commonly used for SHM systems, namely FBG and distributed fibre optics. The objective of this experimental campaign was to determine whether the sensors commonly employed in SHM systems, effectively detect damage in thermoplastic composite material as they do for classical thermoset composite materials. This investigation was essential for several reasons. Firstly, thermoplastic composites are gaining popularity in aerospace applications due to their superior impact resistance, recyclability, and potential for rapid manufacturing. However, their adoption depends on reliable damage detection methods to ensure structural integrity and safety. By verifying the performance of SHM sensors in thermoplastic composites, CIRA aimed to validate and potentially enhance monitoring techniques, thereby supporting broader implementation of these advanced materials in the aerospace industry.

Two experimental setups were employed: i) cantilever test of thermoplastic fabric composite coupon equipped with FBG sensors; ii) cantilever test of

thermoplastic fabric composite coupons equipped with distributed fibre optics.

The coupons tested were 20, all obtained from a composite flat panel made using 4 layers of fabric 0–90 CF/PEEK thermoplastic composite material. The relevant properties of the coupons used are listed in Tab. (5.1).

Property	Value
Layer type	Fabric 0–90
Number of layers	4
Nominal layer thickness	0.3 mm
Young Moduli, $E_1 = E_2$	54.4 GPa
Shear Modulus, G_{12}	2.65 GPa
Poisson ratio, ν_{12}	0.05

Table 5.1: Properties of thermoplastic CF/PEEK composite coupons.

As the first step, they were divided into three different categories, as shown in Fig. (5.1). Then, each group was categorised and numbered using these labels:

- TT1, label used for pristine coupons with smaller width;
- TT2, label used for pristine coupons having double width with respect to TT1 coupons;
- TTD, label used for coupons that were subjected to a low-velocity impact that has generated barely visible damage (BVD);
- TTS, label used for pristine coupons having a metal spray coating on the top surface.

Geometric properties, schematically reported in Fig.(5.2), of each coupon

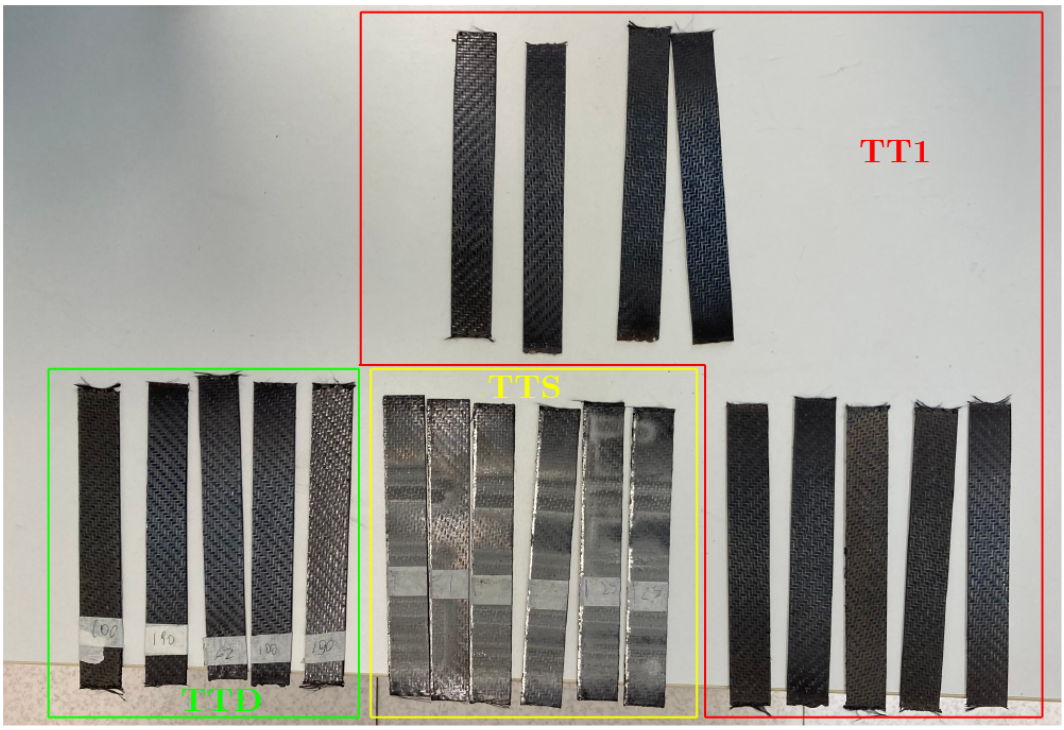

Figure 5.1: Thermoplastic composite coupons divided into categories.

were then measured, namely the length L, the width b and the thickness t, which are reported in Tab. (5.2) in terms of mean values.

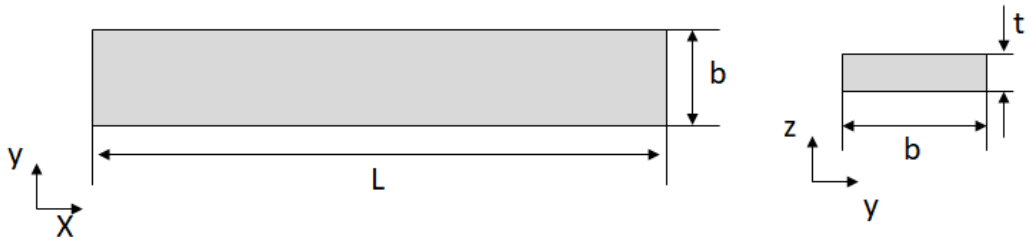

Figure 5.2: Schematic representation of coupon.

It is important to note that all the TTS coupons were initially designed for testing using a three-point bending test. However, after a deep inspection and some preliminary tests, it was discovered that the poor adhesion of the metal spray coating made the results unreliable. Consequently, these coupons were

Coupon ID	L [mm]	b [mm]	t[mm]
TT1	196.0	26.3	1.30
TT2	194.2	51.5	1.55
TTD	196.0	25.6	1.60
TTS	194.9	26.6	1.55

Table 5.2: Mean geometric values for each coupon category.

discarded due to their unsatisfactory performance.

5.1 Cantilever test

In this section the experimental setup as well as the relevant geometric properties of specimens are reported, while the results are shown in *Chapter 6*.

The cantilever test was conducted using a displacement-controlled machine to lower the free end of the beam step by step. The other end of the beam was secured in a clamp, creating a fixed support constraint. The schematic representation of the cantilever test and the actual setup are reported in Fig.(5.3).

The tests were conducted under quasi-static loading conditions to prevent any influence from potential dynamic behaviour on the response. Hence, small increments of displacement were applied during the test, and after the structure stabilised, the force values and displacement increments were recorded.

Next, the testing was organised into two separate batches:

- **Test Batch #1 (TB1)**: This series included two coupons, one from the TT1 category and one from the TTD category. These were used to evaluate the performance of FBG and distributed fibre optic sensors.

- **Test Batch #2 (TB2)**: In this series, all remaining coupons were

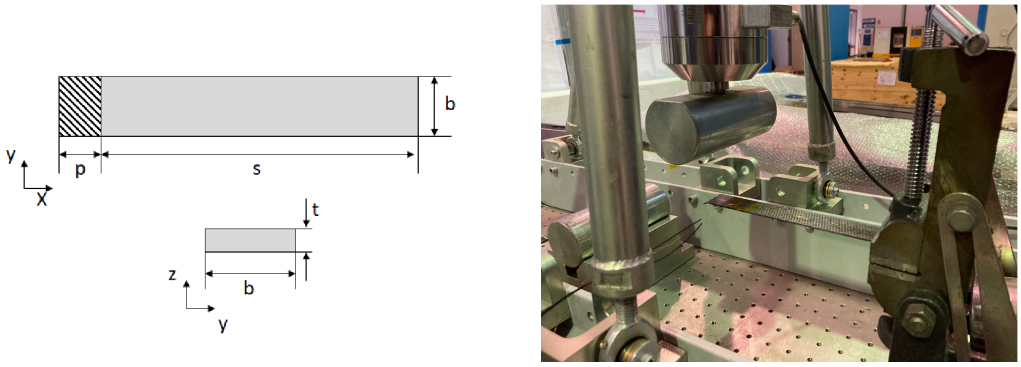

(a) (b)

Figure 5.3: Experimental setup for cantilever beam test: (a) schematic representation and (b) actual experimental setup used.

tested, with only force and displacement data being recorded. The purpose was to verify the robustness of the experimental setup.

5.1.1 Test Batch #1

The selected specimens for the TB1 test were: TT1-01, tested in two different configurations—one as pristine and the other rotated 180 degrees about the axis normal to the top surface; and TTD-01, which exhibited BVD. These coupons were first sensorised with FBG sensors. Four sensors were glued along the x direction on the top surface of each coupon as shown in Fig. (5.4b). The schematic representation of the FBG installation is reported in Fig. (5.4a).

In Tab. (5.3) the actual positions of the FBGs are reported for the three configurations while in Tab. (5.4) are reported the geometric properties referred to Fig.(5.4a) and the number of tests conducted for each specimen.

After evaluating the capabilities of the FBG sensors, the investigation shifted to examining the behaviour of distributed fibre optics. The distributed fibre optic was glued on each coupon tested on the top surface of the specimen using two branches, allowing for a comprehensive analysis of its performance

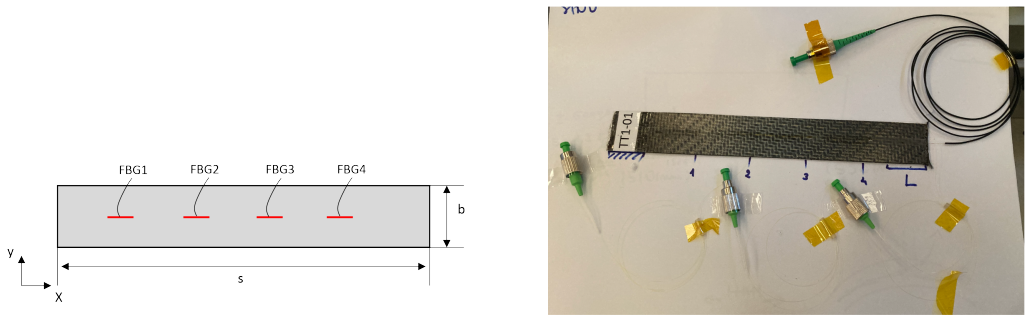

(a) (b)

Figure 5.4: Schematic (a) and real position (b) of the FBG sensors installed on the pristine coupon TT1-01.

Coupon ID	FBG distance from $x = 0$ [mm]			
	FBG1	FBG2	FBG3	FBG4
TT1-01	19.0	58.0	102.0	122.0
TT1-01 (flipped)	28.0	48.0	92.0	131.0
TTD-01	24.0	56.0	89.0	115.0

Table 5.3: FBG position for three different configurations tested.

in detecting and locating damage.

First, a distributed fibre optic was installed in the TTD-01 coupon to determine if it could accurately locate the position of damage, particularly near the BVD area.

Subsequently, artificial damage was introduced in the TT1-01 coupon to assess the accuracy of the damage estimation provided by the fibre optic sensor. The schematic representation and the corresponding geometric values of the TT1-01 damaged coupon are reported in Fig. (5.5) and Tab. (5.5) respectively.

Coupon ID	Number of tests	s [mm]	b [mm]	t [mm]
TT1-01	5	174.0	26.2	1.3
TT1-01 flipped	2	174.0	26.2	1.3
TT1-01	5	174.0	25.6	1.6

Table 5.4: Geometric properties and number of tests conducted for specimens TT1-01 and TTD-01.

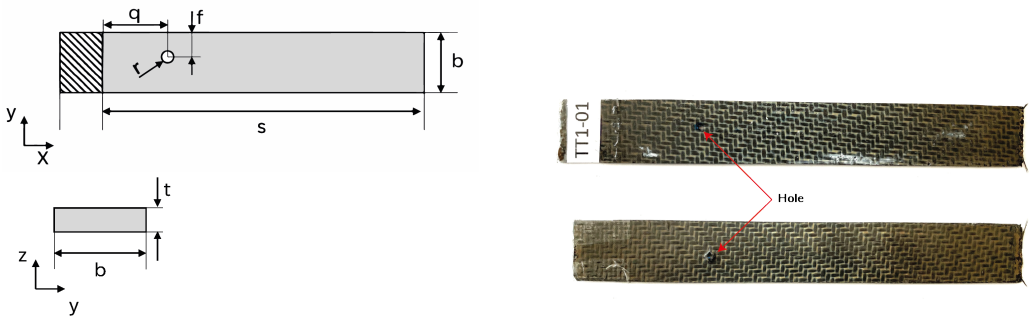

(a) (b)

Figure 5.5: Geometric properties for coupon TT1 with hole tested in TB1: (a) schematic representation; (b) picture of actual damage.

5.1.2 Test Batch #2

In this series of tests, all remaining coupons were evaluated, focusing on recording force and displacement data. The primary objective was to verify the robustness and reliability of the experimental setup, ensuring that it consistently produced accurate and repeatable results. This step was used to identify any potential issues or inconsistencies in the measurement process. Additionally, it helped in tuning the equipment and methodology, ensuring that all parameters were optimally set for precise data collection. Only one test for each specimen

Coupon ID	s [mm]	b [mm]	t [mm]	q [mm]	f [mm]	r
TT1-01 (damaged)	174.0	26.0	1.3	36.5	11.5	3.0

Table 5.5: Geometric properties of artificial damage made on specimens TT1-01.

was performed, to avoid any accumulation of damage between subsequent tests of the same coupon. Tabs. (5.6)– (5.8)report the geometric properties of the coupons tested.

Coupon ID	s [mm]	b [mm]	t [mm]
TT1-02	173.0	25.5	1.4
TT1-03	173.0	26.6	1.4
TT1-04	175.0	27.3	1.4
TT1-05	175.0	26.1	1.3
TT1-06	174.0	26.0	1.3
TT1-07	175.0	26.3	1.4

Table 5.6: Geometric properties for coupons TT1 tested in TB2.

Coupon ID	s [mm]	b [mm]	t [mm]
TT2-01	168.0	51.6	1.4
TT2-02	168.0	51.3	1.4
TT2-03	173.0	51.1	1.4
TT2-04	163.0	51.7	1.4
TT2-05	173.0	51.3	1.3
TT2-06	168.0	51.7	1.3
TT2-07	166.0	52.4	1.4

Table 5.7: Geometric properties for coupons TT2 tested in TB2.

Coupon ID	s [mm]	b [mm]	t [mm]
TTD-02	175.0	25.6	1.4
TTD-03	173.0	26.6	1.6
TTD-04	175.0	26.5	1.5
TTD-05	177.0	26.0	1.5

Table 5.8: Geometric properties for coupons TTD tested in TB2.

Chapter 6

Results

In this chapter, both numerical and experimental results obtained during the PhD activities are presented.

The developed computational framework is first validated through a convergence analysis and a comparison with available literature data. Then some analyses are performed for both classical and VAT laminates, considering both small and moderately large strains. For all the performed analyses given in Sec.(6.1), the strain-softening parameter $\alpha_i = 2$ have been selected for each damage index. Then, in Sec.(6.2), first some tests that shows the spurious effects that may arise with the localisation phenomena using a single-domain Ritz approach are presented. Then, by using a multi-domain discretization it is possible to obtain a meaningful response without un-physical behaviour. In all numerical tests, the same order of polynomial for both directions was chosen, namely $M_\chi = N_\chi = p$.

Finally, all the experimental results for TB1 and TB2 obtained with the cantilever test are presented.

6.1 Numerical results for single-domain approach

The proposed model has been validated first by assessing its convergence with respect to the order of the polynomial expansions in the Ritz approximation given in Eq.(4.5). Then, two test cases have been analysed, the first involves a plate that undergoes three-point bending loading in small strains and the second considering a plate subjected to a uni-axial in-plane compression and experiencing non-linear strains in the von Kármán sense.

6.1.1 Method validation

The first analysed case considers the rectangular composite straight-fibres plate schematically represented in Fig.(6.1), with sides of length $2a = 60\,\text{mm}$ and $2b = 25\,\text{mm}$, thickness $h = 1.8\,\text{mm}$. The unidirectional laminate is made up of M10 carbon/epoxy layers, whose material properties are listed in Tab.6.1, with $[0]_{10}$ laminate lay-up. The boundary conditions for the three-point bending test are defined so that, on the short edges, the rotation ϑ_1 and the in-plane displacements are free whilst the other degrees of freedom are fully constrained, whereas the longest edges are completely free.

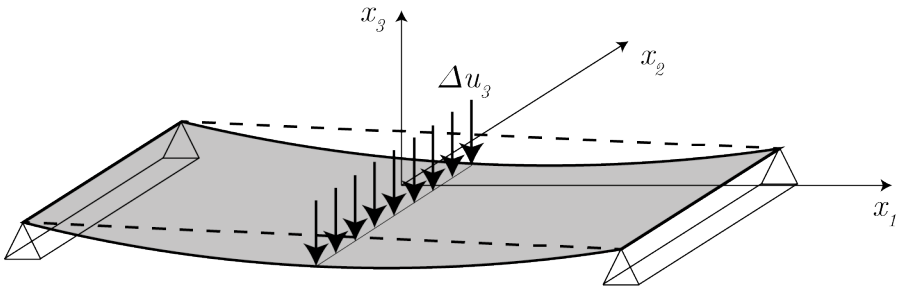

Figure 6.1: Schematic representation of three-point bending test.

The analysis has been performed in displacement control by increasing, at each step, the applied displacement Δu_3 of all the points of the centre segment

Elastic property		Value	Strength property		Value
E_1	[GPa]	105.00	X_T	[MPa]	1400.0
E_2	[GPa]	8.57	X_C	[MPa]	930.0
$G_{23} = G_{13}$	[GPa]	3.05	Y_T	[MPa]	47.0
G_{12}	[GPa]	4.39	Y_C	[MPa]	60.3
ν_{12}		0.34	S_L	[MPa]	53.0

Table 6.1: Material properties of straight fibre lamina [1] used in three-point bending test.

of the plate and employing a Newton-Raphson scheme. The convergence of the solution with respect to the degree of the polynomial expansion has been assessed by studying the total reaction force along the x_3 direction at the supports and the displacement of the central point of the plate which is shown in Fig.(6.2a).

The analysis shows that, for the considered case, convergence is quickly achieved in the initial linear part of the response, whilst a relatively high number of polynomial expansion terms, up to the order $p = 30$, are needed to accurately represent the response in the proximity of failure, as could be reasonably expected considering the localisation of damage. The converged results, corresponding to $p = 30$, were then compared with experimental and FE results [138]. The analysis using the Ritz method with $p = 30$ has a total of 4500 degrees of freedom (DOFs), whilst the FE results have been obtained using 2000 S8R elements with 49266 DOFs. As it can be observed in Fig.(6.2b), even if the proposed model underestimates the maximum load, it provides good agreement with the experimental test measurements.

The second analysed case considers a quadrilateral quasi-isotropic composite plate with sides of length $2a = 2b = 250\,\text{mm}$ and thickness $h = 6\,\text{mm}$

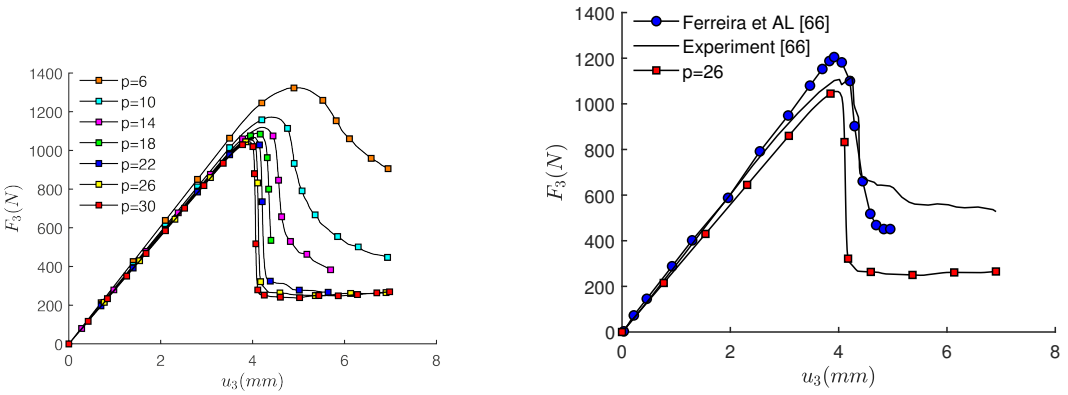

(a) (b)

Figure 6.2: Three-point bending test of the unidirectional laminate response in terms of reaction force of supports vs transverse displacement at the centre of the plate. (a) Convergence analysis and (b) comparison between the present model, experimental and FE results.

subjected to uni-axial in-plane compression load along the x_1 direction, as schematically represented in Fig.(6.3).

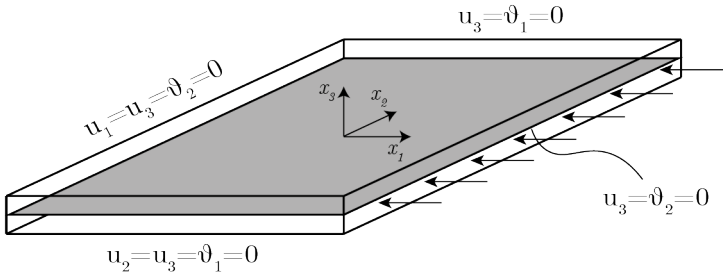

Figure 6.3: Schematic representation of the compressive test.

The laminate is assembled from carbon/epoxy layers whose material properties are listed in Tab. 6.2, whilst its stacking sequence is $[0/90/45/-45]_S$. Also in this case a convergence analysis has been first performed. To promote the plate lateral deflection before buckling, an initial imperfection is introduced

as a bi-sinusoidal prescribed deflection with amplitude $0.005\,h$. The boundary conditions used in this analysis are reported in Table 6.3.

Fig.(6.4) shows the results of the convergence analysis in terms of transverse displacement of the plate's mid-plane centre point versus the axial load value. The transverse displacement is normalised with respect to the plate thickness, whilst the axial load is normalised with respect to the critical buckling load [139]. In this case, results obtained with $p = 22$ do not significantly differ from those obtained with $p = 18$. Therefore, to perform faster analyses, the polynomial degree $p = 18$, which gives a total of 1620 DOFs, was used for the subsequent geometrically non-linear analyses involving comparable load cases. For validation purposes, Fig.(6.4) shows results from three different `ABAQUS` analyses, which are obtained using meshes of 20×20, 30×30 and 50×50 elements, respectively. For each mesh, S4R element type is considered, which gives a total of 2646, 5766 and 15606 DOFs, respectively. The FE results have been obtained employing an orthotropic damage model and adopting the built-in `ABAQUS` localisation mitigation strategy, based on the crack-band theory. However, it is observed that even adopting such a scheme, the FE results show a relative scatter, which is consistent with several literature sources, see e.g. Ref.[130], which report that energy regularisation strategies based on the crack band theory may partially lose objectivity for complex loading cases. It is also shown that, compared to the FE/`ABAQUS` results, the curves obtained by the proposed Ritz method exhibit reduced scatter and appear to converge with increasing polynomial order approximation.

6.1.2 Damage analysis of VAT laminates

After validation, the developed method has been applied to the analysis of VAT composite plates.

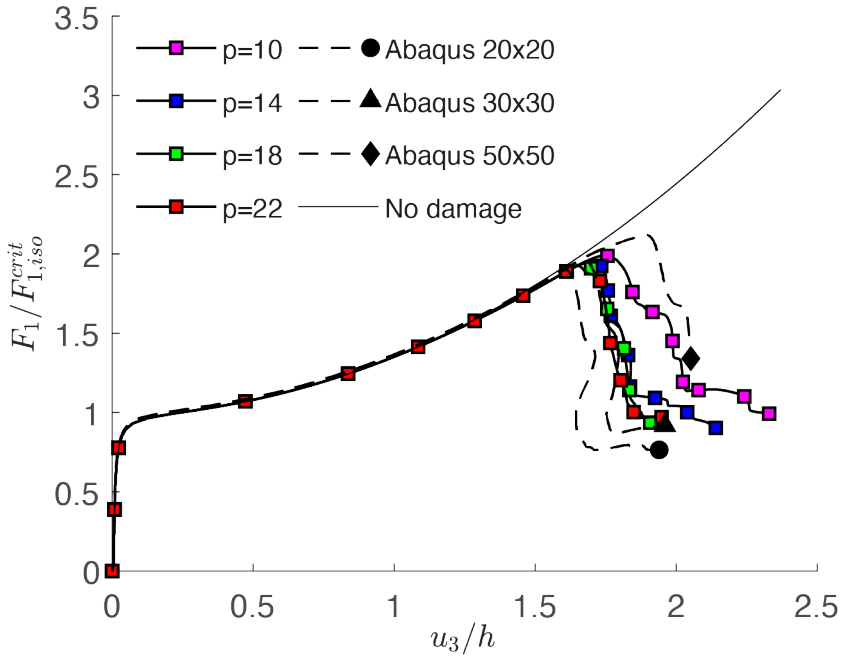

Figure 6.4: Convergence study of quasi-isotropic laminate under in-plane compressive load. Results obtained with the Ritz method are compared with FE/ABAQUS results for different discretizations.

Elastic property		Value	Strength property		Value
E_1	[GPa]	181.00	X_T	[MPa]	1500.0
E_2	[GPa]	10.27	X_C	[MPa]	1200.0
G_{ij}	[GPa]	7.17	Y_T	[MPa]	40.0
ν_{12}		0.34	Y_C	[MPa]	176.0
			S_L	[MPa]	68.0

Table 6.2: Material properties of straight fibre lamina for the compressive test, where $G_{ij} = G_{23} = G_{13} = G_{12}$.

Edge		u_1	u_2	u_3	ϑ_1	ϑ_2
$x_2 = -b,$	$x_1 \in [-a, a]$	F	C	C	C	F
$x_1 = +a,$	$x_2 \in (-b, b]$	F	F	C	F	C
$x_2 = +b,$	$x_1 \in (-a, a]$	F	F	C	C	F
$x_1 = -a,$	$x_2 \in [-b, b]$	C	F	C	F	C

Table 6.3: Boundary condition used for the convergence study of quasi-isotropic laminated. F=Free and C=Clamped.

The first test considers a VAT composite plate with stacking sequence $[0 + \langle 0| - 90\rangle/0 + \langle 90|0\rangle/0]_S$ under tensile loading. The material properties for each lamina with respect to the fibre and transverse directions are given again in Table 6.2. The plate has sides of size $2a = 2b = 250\,\text{mm}$ and thickness $h = 6.25\,\text{mm}$.

Fig.(6.5) shows the response in terms of force vs displacement along the x_1 direction. As expected, after the load reaches a maximum level, it suddenly drops while the damage level in each ply rises. Referring to Fig.(6.5), four points of interest along the loading curve are highlighted: point A identifies

the initiation of damage; point B corresponds to the maximum load; points C and D describe the post-failure load drop.

The contour plots of the relevant damage indexes corresponding to the four highlighted points are reported in Fig.(6.6), which describes how damage evolves through the thickness during the loading process. It is worth noting that only the results for the first three plies are shown, considering the symmetry of the laminate. At point A, matrix tension damage initiates in the first two plies, whereas the 0° ply is still undamaged. When the maximum load is attained, at point B, damage has spread through the thickness in all the laminae. Next, in the proximity of the sudden load drop, damage still evolves in all the plies, as can be seen for point C, before eventually reaching the maximum level at point D.

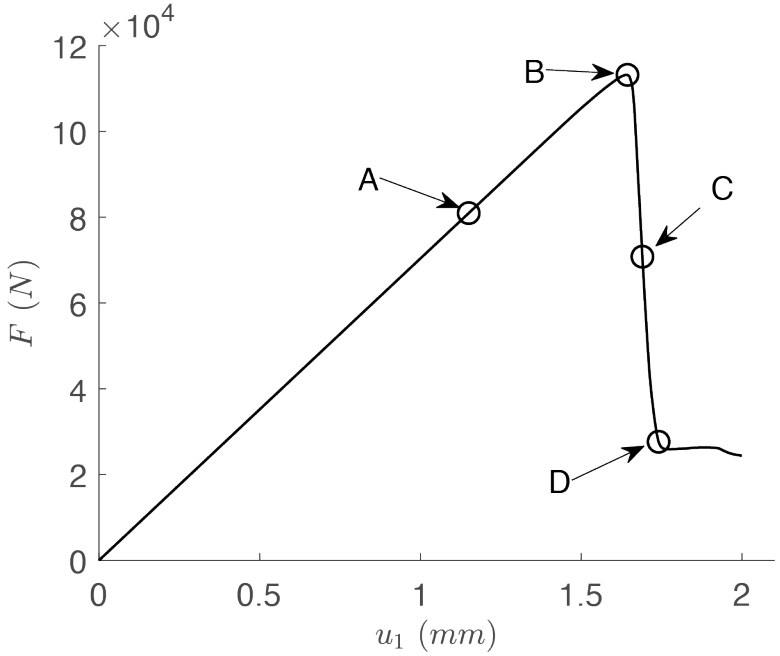

Figure 6.5: Force vs displacement results for VAT laminate under tensile load.

After considering a VAT laminated plate in tension, for which a small strains implementation has been employed, some VAT laminates under com-

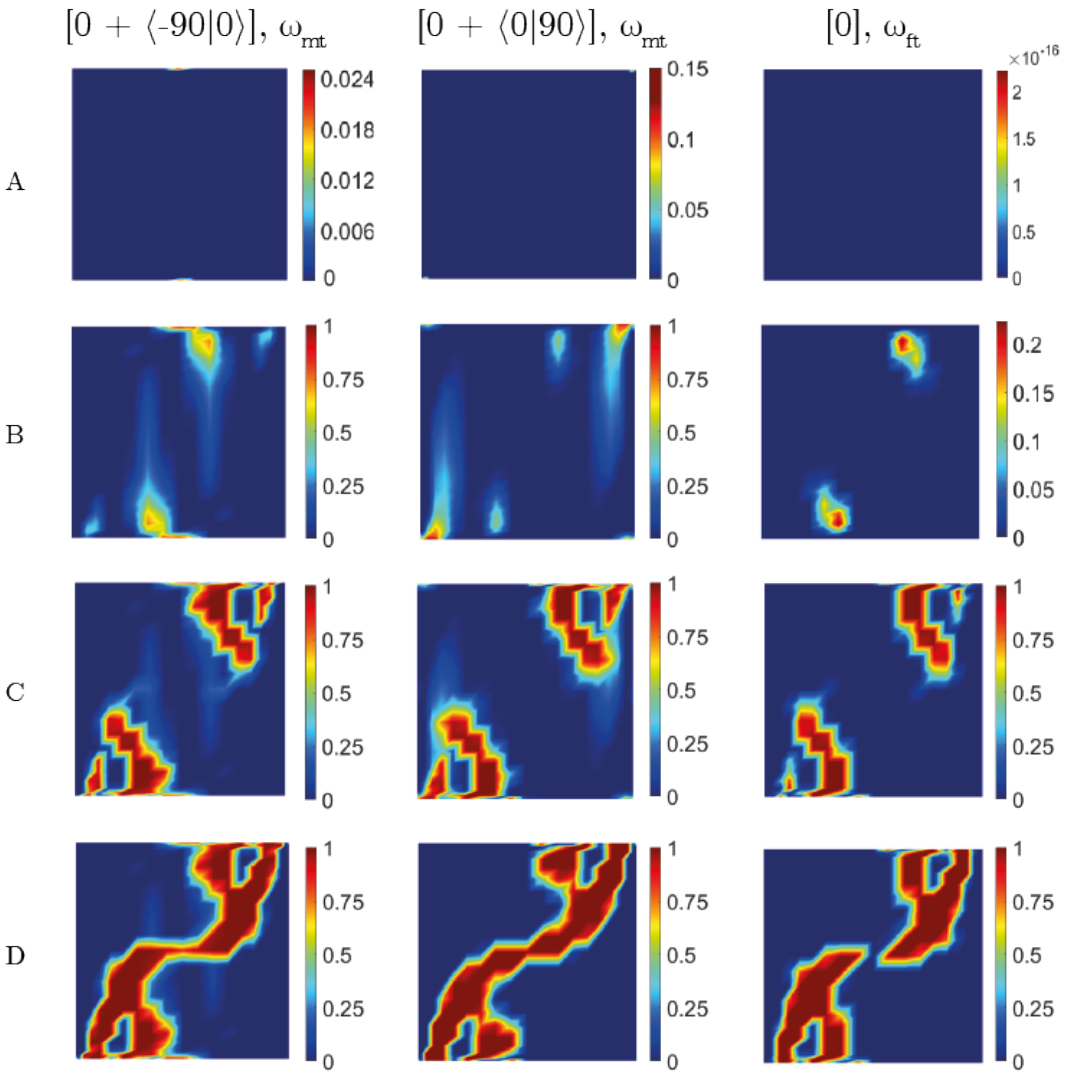

Figure 6.6: Damage contour plots for 3 plies of a VAT laminate laminate under tensile test at points of interest.

pression loading are analysed, activating the presence of moderate strains in the von Kármán sense.

Square plates with sides of size $a = b = 250\,\text{mm}$ are considered. Four lay-ups, namely $[90 \pm \langle 0|75\rangle]_{3S}$, $[0 \pm \langle 0|15\rangle]_{3S}$, $[0 \pm \langle 0|45\rangle]_{3S}$, $[0 \pm \langle 45|0\rangle]_{3S}$ are investigated. They consist of 12 constant thickness plies, each 0.27 mm thick. The material properties for each orthotropic layer, along the fibres and

transverse directions, are summarised in Table 6.2. The panels are loaded by uniform axial displacement imposed along the edges parallel to the x_2 axis and an initial prescribed lateral bi-sinusoidal deflection of amplitude $0.005\,h$ has been introduced, where h indicates the plate thickness. Simply-supported boundary conditions are assumed for all the edges, with free in-plane displacements allowed along the unloaded edges, as reported in Fig.(6.7).

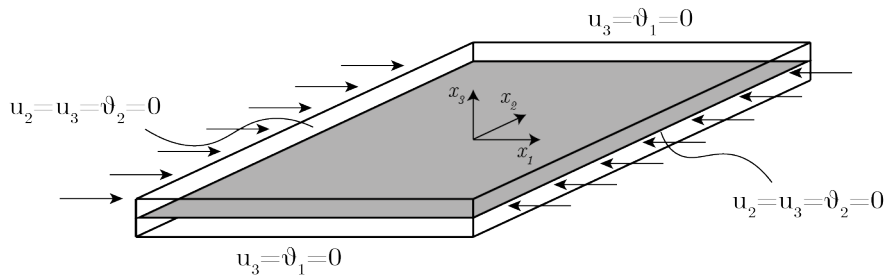

Figure 6.7: Schematic representation of the VAT composite under compressive load.

Fig.(6.8) shows the comparison in terms of in-plane force versus plate centre deflection for different VAT plate stacking sequences. The force has been normalised with respect to the critical buckling load of a quasi-isotropic laminate of the same size while the transverse displacement has been normalised with respect to the laminate thickness.

The results show that, as expected, the presence of damage affects the mechanical response of the plate, identifying a maximum load after which the bearing capability of the plate is noticeably degraded. Such results may be useful for identifying the operational limits of different lay-ups, thus providing valuable insights to the designer.

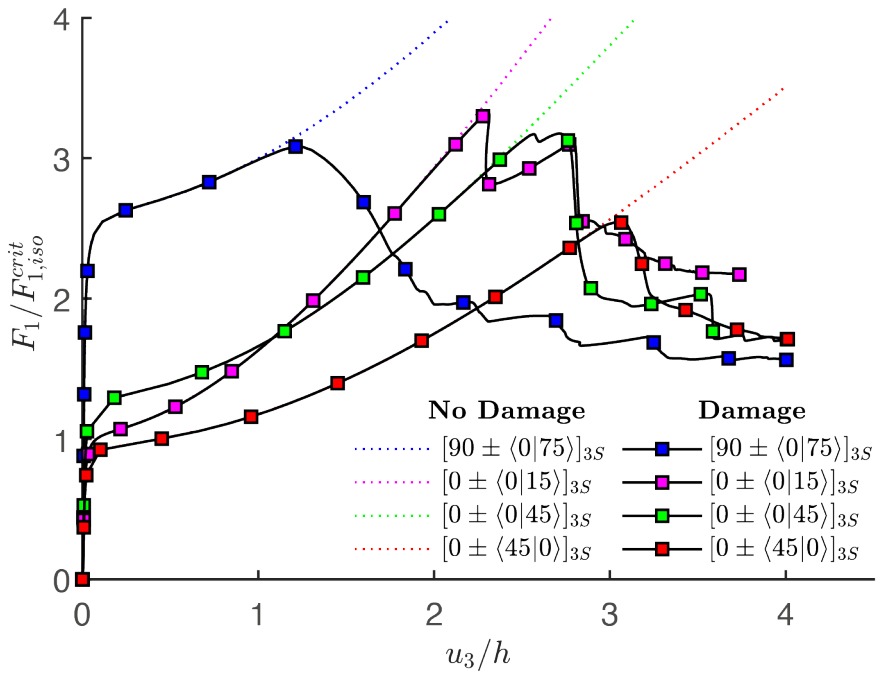

Figure 6.8: Comparison of post-buckling results in terms of force vs transverse displacement with and without the damage model activated for different VAT layups under in plane-load.

6.2 Numerical results for multi-domain approach

In this section, some applications of the multi-domain Ritz approach are presented. The first test shows the spurious effects that may arise with the localisation phenomena using a single-domain Ritz approach. Next, by using the multi-domain adaptive discretization developed it is possible to obtain a meaningful response without un-physical behaviour. In all tests, the same order of polynomial for both directions was chosen, namely $M_\chi = N_\chi = p$.

6.2.1 Treatment of damage Gibbs artefacts

To illustrate the issues arising when coupling the single-domain Ritz method with a localised damage representation, a square unidirectional composite lamina subjected to uniaxial tension is considered, as shown in Fig.(6.9). Moreover, a narrow band of material along the x_2 axis in the left vertical edge has strength lower than the rest of the plate, to artificially induce the onset of the damage. The plate has sides $L = H = 10\,\text{mm}$, and the material properties are given in Tab. 6.4.

The analysis is performed in displacement control, by setting the maximum displacement $u_1 = 0.15\,\text{mm}$. Fig.(6.10) shows the damage plot related to the damage index ω_{ft} in the fibre direction for different polynomial expansions used in the Ritz approximation scheme. It is clear that the Gibbs effect is present and generates an oscillatory behaviour of the damage along the x_1 axis. The presence of Gibbs effects is due to the employment of the single-domain Ritz method, which has global support, for capturing a localised damage phenomenon. After reaching the peak stress, material points unaffected by damage generally unload. As a result, the strain values in contiguous material points can exhibit steep variations. Hence, the polynomial Ritz approximation in Eq.(4.9) may fail to capture such localised variation, giving rise to the

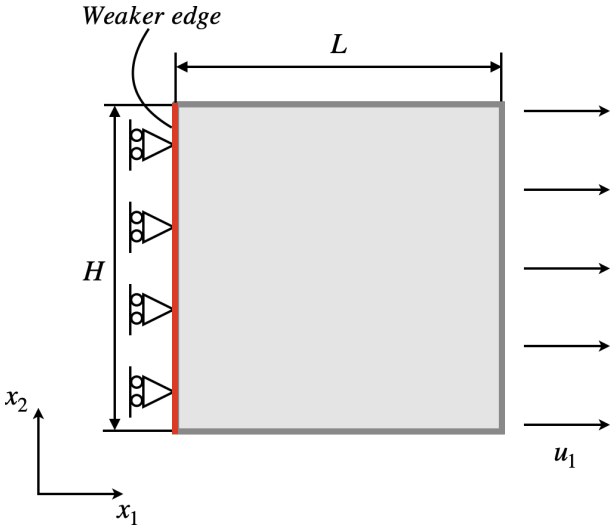

Figure 6.9: Schematic representation of square plate loaded with a prescribed displacement u_1 in the x_1 direction applied on the right edge.

mentioned Gibbs effect [140].

To address this inconvenience, this study has explored various methods, such as utilising filters to minimise the presence of Gibbs ripples. Although such approaches have demonstrated some advantages, they were not able to fully remove Gibbs artefacts. Therefore, a strategy based on the adaptive multi-domain subdivision of the analysis domain has been considered. The same test as that performed above is now analysed using the adaptive multi-domain procedure schematically represented in the block diagram in Fig.(4.1). Starting from a single-domain representation, the damage onset is triggered at the level of displacement $u_2 = 0.0165\,\text{mm}$. At this stage, the multi-domain discretization procedure is activated. The new sub-domains, which are coloured in grey in Fig.(6.11), adopt a Ritz polynomial expansion of order $p = 1$, whilst the bigger sub-domain maintains a higher polynomial order, namely $p = 4$, to retain a high level of accuracy. As shown in Fig.(6.11), three different discretizations were employed to verify the independence of the response from the

Properties	Values
Modulus [GPa]	$E_{11} = 105.0$; $E_{22} = 8.57$;
	$G_{23} = G_{13} = 3.05$; $G_{12} = 4.39$
Poisson's ratio	$\nu_{12} = 0.34$
Strength [MPa]	$X^T = 1400.0$; $X^C = 930.0$;
	$Y^T = 47.0$; $Y^C = 60.3$;
	$S^L = S^T = 53.0$
Fracture toughness [kJ m^{-2}]	$G_{c,ft} = 200$; $G_{c,fc} = 100$
	$G_{c,mt} = 1.0$; $G_{c,mc} = 1.0$

Table 6.4: Material properties of straight fibre lamina used in tensile test.

number and the dimension of the sub-domains: (*i*) discretization of Fig.(6.11a) is named *3E2B* and uses two sub-domains in the damaged band; (*ii*) discretization of Fig.(6.11b) is named *5E4B* and uses four sub-domains in the damaged band; (*iii*) discretization of Fig.(6.11c) is named *9E8B* and uses eighth sub-domains in the damaged band.

Damage plots related to each discretization used are reported in Fig.(6.12), where it appears that the Gibbs effect is completely removed.

Fig.(6.13a) shows the result in terms of force-vs-displacement, which confirms the independence of the type of multi-domain discretization used, thus validating the objectivity of the response. Finally, the solution of the present method is compared with FE results obtained with the ABAQUS built-in CDM model in Fig.(6.13b). The comparison of the results shows excellent agreement with established FE analysis methods.

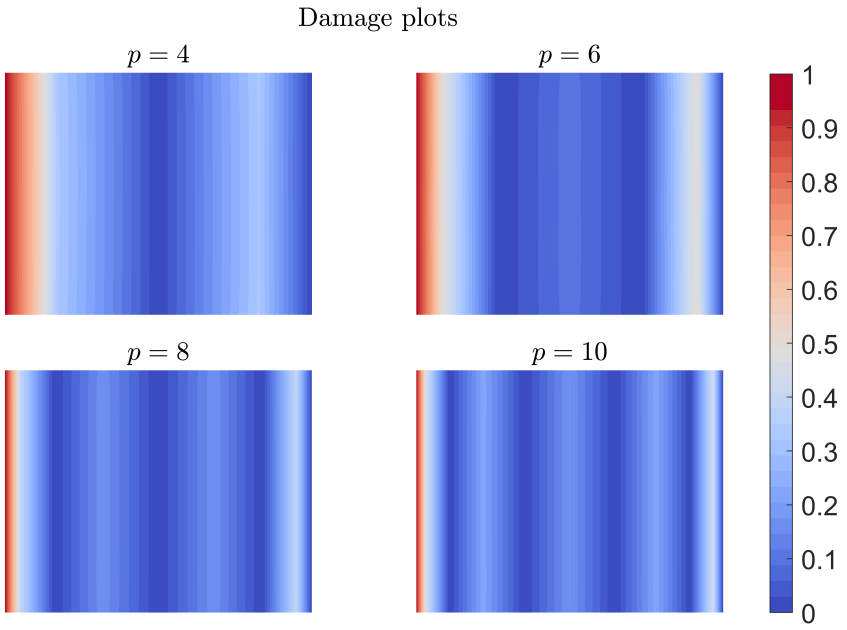

Figure 6.10: Damage plot of ω_{ft} index for lamina in tension showing Gibbs effects.

6.2.2 Method validation

For validation purposes and to assess the capabilities of the developed adaptive multi-domain Ritz method, another test is herein reported. The damage evolution in a composite unidirectional lamina under tensile load with a pre-existing crack spanning half length of the edge has been considered. The plate was modelled taking advantage of the symmetry to reduce the number of degrees of freedom. The geometry and boundary conditions of this test case are reported in Fig.(6.14). The half specimen modelled is a square plate with sides $L = H = 200\,\text{mm}$ and thickness $h = 1\,\text{mm}$. Material properties for the composite material used are reported in Tab. (6.4) and the lamina has a fibre orientation $\theta = 0°$ with respect to the x_1 axis.

The whole plate domain was initially divided into three sub-domains as shown in Fig.(6.15a), where the sub-domain (1) was used to model the pre-

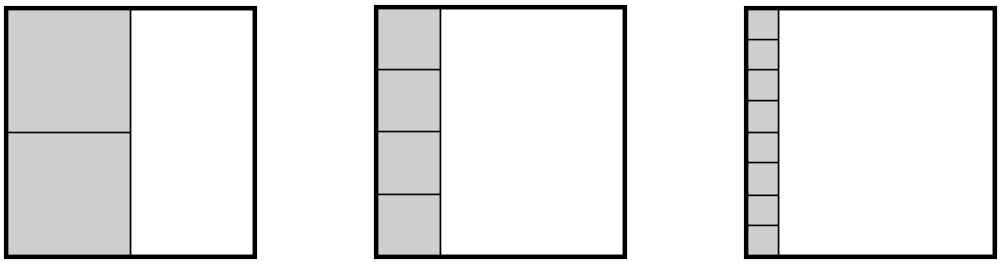

(a) (b) (c)

Figure 6.11: Multi-domain discretizations used: (a) discretization 3E2B; (b) discretization 5E4B; (c) discretization 9E8B.

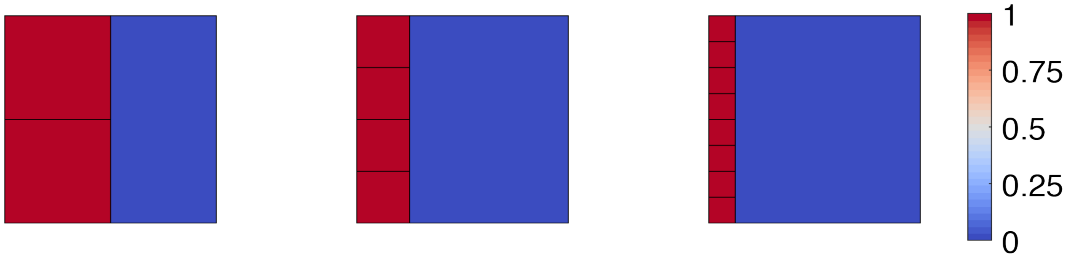

(a) (b) (c)

Figure 6.12: Damage plots of ω_{ft} index for lamina in tension adopting different discretizations showing the removal of Gibbs effect.

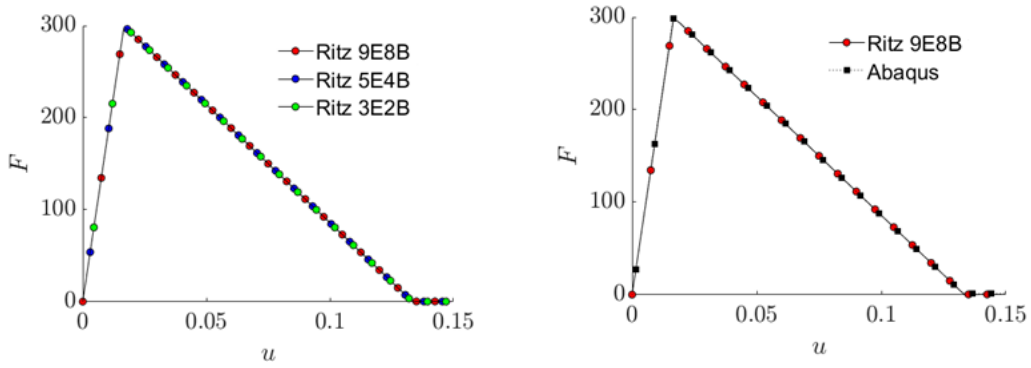

(a) (b)

Figure 6.13: Force-vs-displacement result of unidirectional composite lamina in tension: (a) comparison for three different discretizations showing discretization-independent results; (b) comparison of present method with `ABAQUS`.

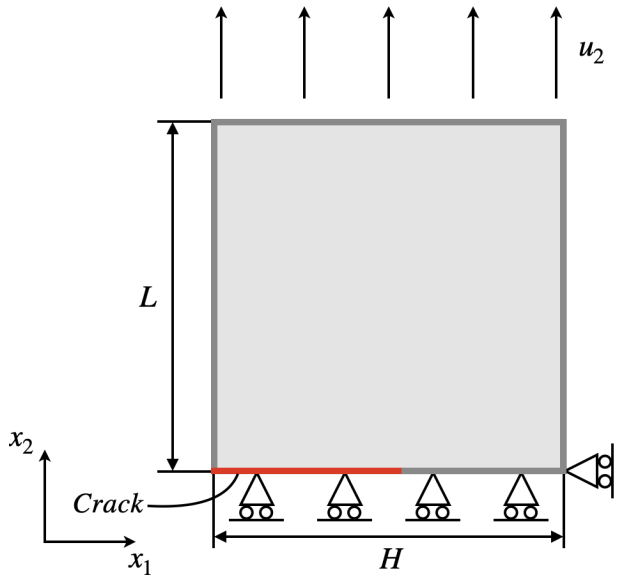

Figure 6.14: Geometry and boundary condition for unidirectional lamina with a pre-existing crack.

existing crack by setting all the damage indices $\omega_i = 1$.

During the incremental loading procedure, the damage starts developing at the crack tip. Hence, the adaptive refinement is activated following the procedure illustrated in Fig.(4.1). The damage propagates along the x_1 direction and the new sub-domains were added only next to the crack tip. Fig.(6.15b) shows an intermediate discretization step where the subdomains in which the damage spread are coloured in grey. The final stage of discretization is reported in Fig.(6.15c), where the damage is fully propagated along the side of the plate.

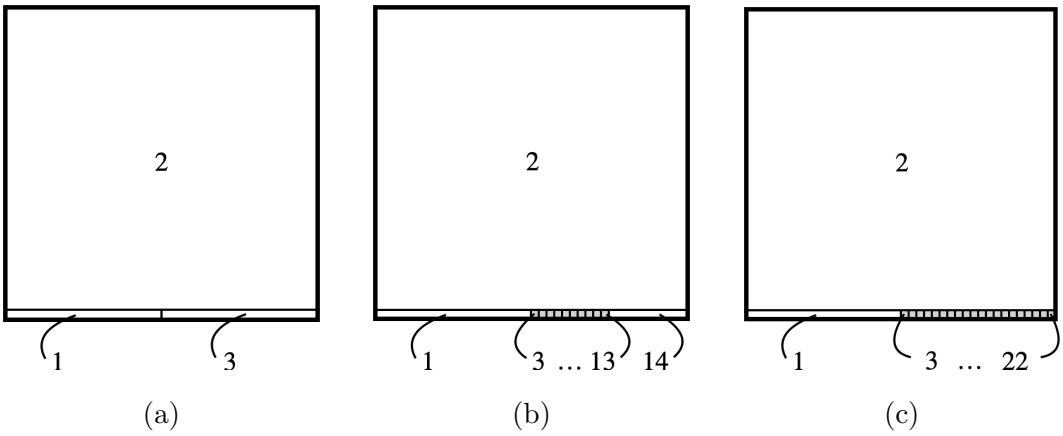

Figure 6.15: Different phases of adaptive discretization used: (a) initial discretization; (b) intermediate discretization; (c) final discretization.

The solution convergence concerning the polynomial order has been evaluated by examining the total reaction force and displacement in the x_2 direction, as shown in Fig.(6.16a). The analysis demonstrates that, in the specific case studied, rapid convergence is attained by utilising a polynomial order of $p = 6$ for the undamaged sub-domains. These findings have been compared to results obtained using `ABAQUS`, employing a converged mesh composed of 20×20 finite elements. Fig.(6.16b) illustrates a strong agreement between the results, validating the proposed approach. Furthermore, a reduction of approximately

60% in the number of system DOFs can be observed: the proposed model, employing a polynomial expansion of $p = 6$, has a total of 1068 DOFs, while the FE analysis involves 2646 DOFs.

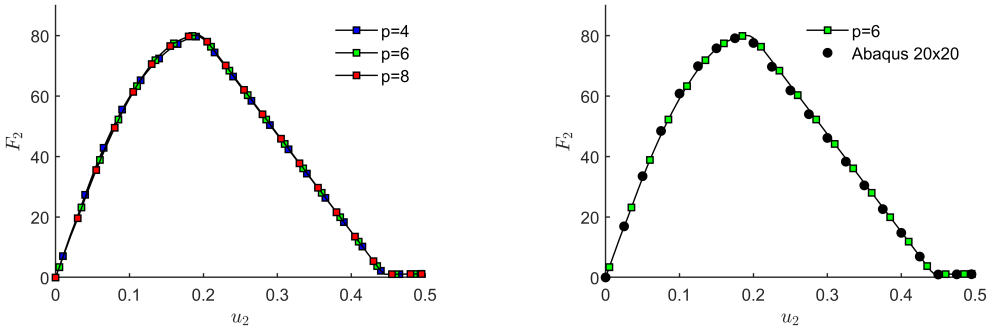

(a) (b)

Figure 6.16: Results of the composite lamina with pre-existing crack loaded in tension: (a) convergence analysis; (b) comparison of results with `ABAQUS`.

6.2.3 Notched VAT thermoplastic lamina

Subsequent tests were performed to show the behaviour of a single-edge notched VAT lamina loaded in tension. The schematic representation of the problem is reported in Fig.(6.14) with geometrical parameters $L = 1\,\text{mm}$ and $H = 0.75\,\text{mm}$. The properties of the material used refer to an AS4/PEEK thermoplastic composite material that is reported in Table 6.5. The analyses were performed in displacement control, using a maximum displacement increment $\Delta = 1 \times 10^{-4}\text{mm}$ which can be automatically adjusted during the iteration to obtain a convergent solution in the Newton-Raphson numerical procedure.

Four different VAT laminae were analysed having a fibre variation angle of $[0 + \langle 30|0\rangle]$, $[0 + \langle 45|0\rangle]$, $[0 + \langle 0|30\rangle]$ and $[0 + \langle 0|45\rangle]$ respectively. Fibre path representations for each lamina are reported in Fig.(6.17).

Properties	Values
Modulus [GPa]	$E_{11} = 127.6$; $E_{22} = 10.8$; $G_{12} = G_{13} = 6.0$; $G_{23} = 5.7$
Poisson's ratio	$\nu_{12} = 0.32$
Strength [MPa]	$X^T = 2023.4$; $X^C = 1234.1$; $Y^T = 92.7$; $Y^C = 176.0$; $S^L = S^T = 186.0$
Fracture toughness [kJ m^{-2}]	$G_{c,ft} = 201$; $G_{c,fc} = 128$ $G_{c,mt} = 0.8$; $G_{c,mc} = 0.8$

Table 6.5: Properties of AS4/PEEK composite lamina.

Fig.(6.18) shows the response in terms of force vs displacements for the analysed laminae. For all configurations, after the linear-elastic branch, a nonlinear response occurs due to the onset and evolution of damage, up to the point where the lamina is completely broken.

The discretization employed at the beginning of the analysis was composed of three subdomains utilising a polynomial order of $p = 12$ for each of them giving a total number of 3042 DOFs. In the final stage, the adaptive discretization results in a total number of 138 subdomains: 135 of order $p = 1$ were used to track the damage evolution, whilst 3 of order $p = 12$ were used for the undamaged subdomains, giving a total number of 6282 DOFs.

6.3 Experimental results for TB1

In this section results obtained from the experimental tests of TB1 are presented.

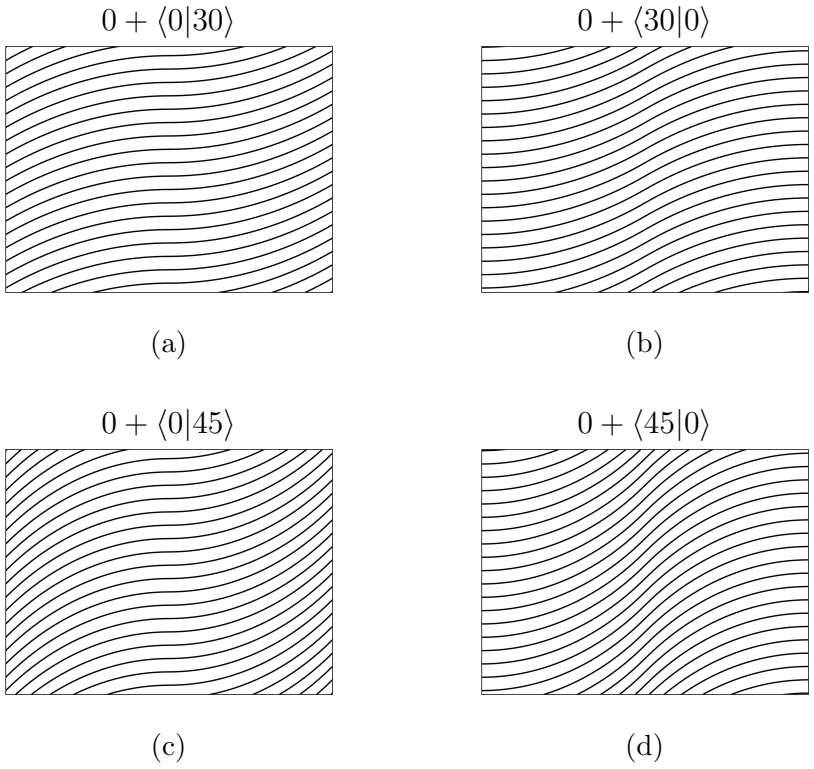

Figure 6.17: Fibre path representations for each lamina analysed.

6.3.1 Cantilever test with FBG sensors

The first set of tests for TB1 was conducted on the pristine coupon equipped with four FBG sensors, identified as TT1-01. Five different quasi-static tests were performed to collect data on force, displacements, and readings from the FBG sensors. The primary parameter observed was the flexural modulus: any reduction in this value would indicate the occurrence of damage.

After data collection, the computed flexural modulus was compared with the reference flexural modulus shown in Tab.(5.1). Fig.(6.19) shows the results of the five different tests in terms of force vs displacement for coupon TT1-01 in pristine condition. The flexural modulus was computed as,

$$E_{exp} = m\frac{4s^3}{bt^3}, \tag{6.1}$$

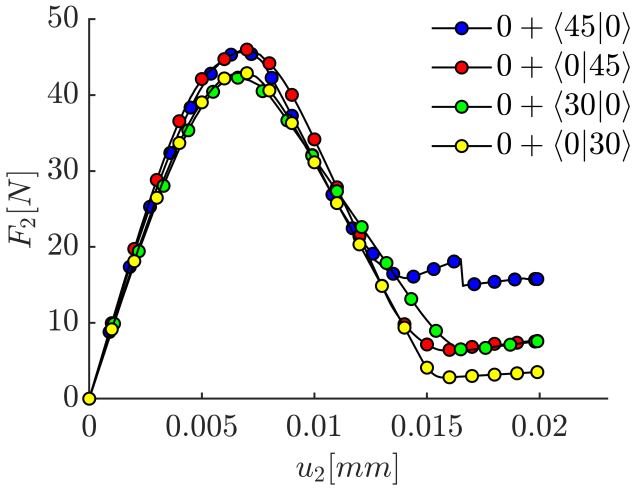

Figure 6.18: Force vs displacement curves for VAT AS4/PEEK thermoplastic composite laminae.

where m is the slope of the linear elastic response of the force vs displacement curve. Tab.(6.6) shows the computed flexural modulus values and their deviations from the reference value. The computed moduli are generally consistent with the reference value, except for test#3 and test#5. The discrepancies in these tests could be due to operator reading errors or issues in the experimental setup, such as misalignment of the load application point. Fig.(6.20) shows the data computed from the FBG sensors in terms of local flexural modulus for each data point, computed using the relation

$$E_{FBG} = \frac{6F\,(s - x_i)}{bt^2\varepsilon_i}, \tag{6.2}$$

where F is the applied load recorded at the data point considered, the subscript $i \in \{1, 2, 3, 4\}$ indicates the FBG and ε_i is the strain value obtained from the FBG reading. All the computed values obtained from the FBGs suggest that no damage is present, because the local flexural modulus is almost constant between all data points. It is worth noting that test#3 and test#5 have more scatter subsequent values, but these two tests were discarded due to the bad

correlation highlighted in the previous comparison.

Test #	E_{exp} [GPa]	Diff from E_{ref}
1	52.72	0.61%
2	54.00	3.05%
3	60.79	16.01%
4	54.41	3.84%
5	60.79	16.02%

Table 6.6: Experimental flexural moduli computed form force vs displacement results and difference from the reference value for coupon TT1-01 in pristine condition.

Next, other cantilever tests were performed: two for the same pristine coupon by placing the encastre on the other end and five for the specimen TTD-01, which had a BVD. Figs.(6.21) and (6.22) show the results in terms of force vs displacement, while Tab. (6.7) summarizes the flexural moduli E_{exp} computed with Eq.(6.1).

For the TT1-01 flipped coupon, the results were consistent with those of the first set of tests, thereby validating the experimental setup used. In the case of the specimen that was impacted and exhibited BVD, several observations can be made. Firstly, the computed flexural modulus, E_{exp}, is significantly lower than the reference value, indicating that the impact caused damage. Additionally, it was observed that the flexural modulus decreased with each subsequent test, suggesting that the damage was propagating with each loading cycle. Finally, Fig.(6.23) and Fig.(6.24), show the computed flexural moduli using the readings obtained from the FBGs, for specimens TT1-01 flipped and TTD-01 respectively. As expected, for the first coupon, the FBGs did not detect any damage. Additionally, compared to the initial tests conducted on TT1, the

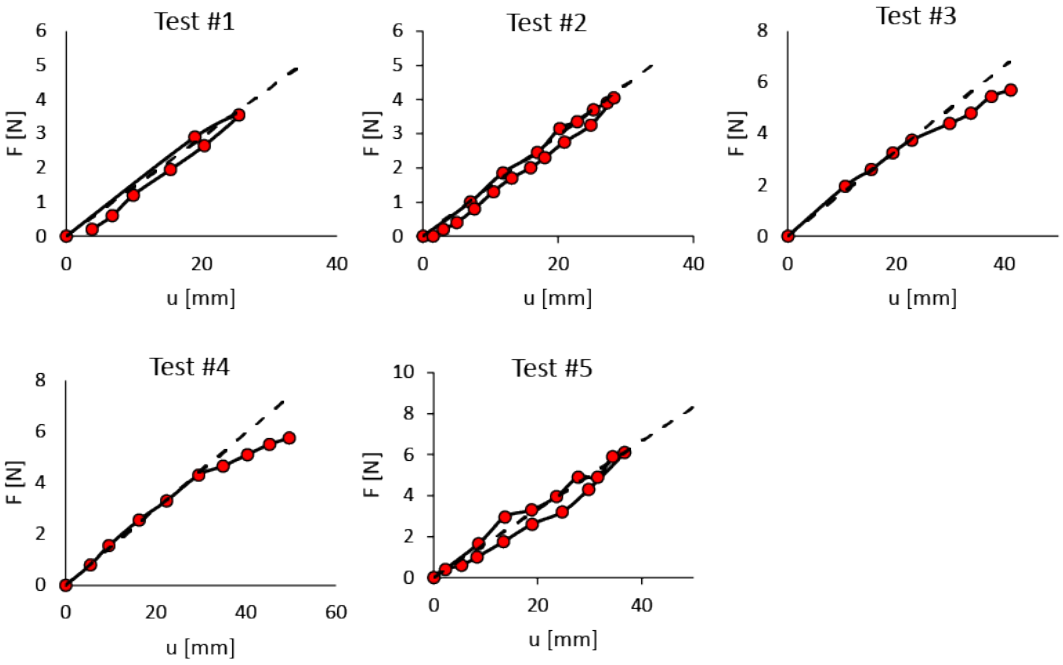

Figure 6.19: Force–displacement plots for specimen TT1-01.

experimental procedure has improved, resulting in less variation between the local readings of the FBGs. For the specimen with the BVD, several observations can be made. First, in the tests 1–3, the reading from FBG_1 was zero because the bonding was imperfect, preventing it from detecting anything. Additionally, at a certain load level, the computed flexural modulus E_{FBG} for FBG_2 drops to zero, indicating potential damage since the local strain reading increases significantly. This is plausible, as FBG2 was positioned very close to the BVD. This result is indicative and provides important insights into the potential presence of damage near the sensor. It shows that a single FBG sensor is capable of detecting local strain variations in the thermoplastic composite specimen. A more precise indication of the damage location could be provided by a network of FBG sensors, supplemented with a correlation algorithm, or by a network of piezoelectric sensors, as used in more traditional SHM systems. If the size and shape of components allow, distributed fibre optics can also be

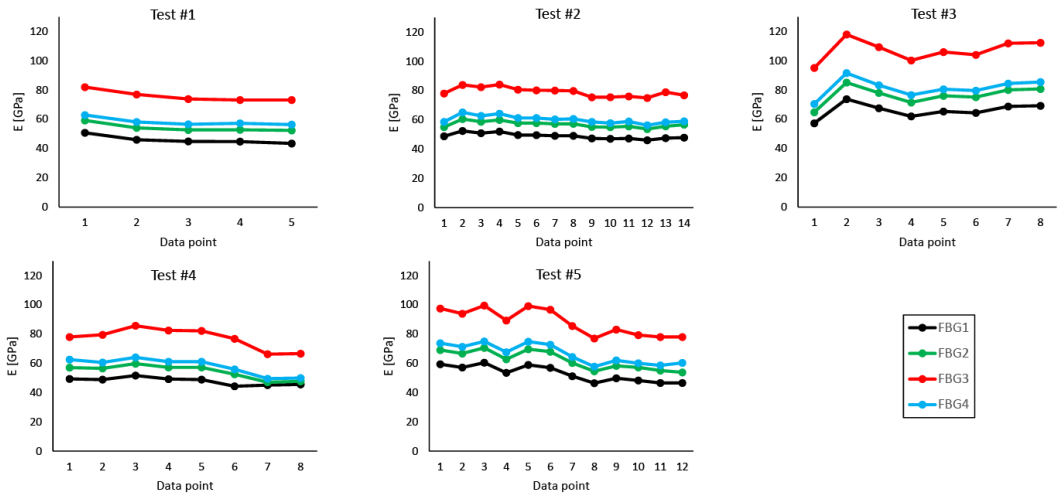

Figure 6.20: Computed flexural modulus at each data point using readings from four FBGs installed in specimen TT1-01.

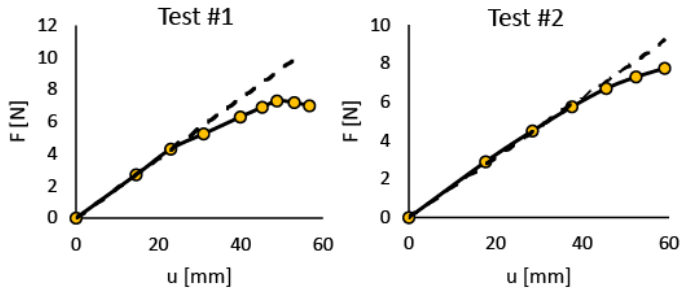

Figure 6.21: Force–displacement plots for specimen TT1-01 flipped.

used, providing information along the entire path where the fiber is installed. Two additional tests utilizing distributed fiber optics will be presented in the following section.

6.3.2 Cantilever test with distributed fibre optic sensors

In the final phase of TB1, two additional tests were performed using distributed fibre optic sensors. These tests aimed to further investigate the capabilities of distributed fibre optics in detecting and locating damage within thermoplastic

Test #	TT1-01 flipped		TTD-01	
	E_{exp} [GPa]	Diff from E_{ref}	E_{exp} [GPa]	Diff from E_{ref}
1	54.80	4.59%	26.97	−48.53%
2	50.95	−2.77%	25.80	−50.76%
3			23.90	−54.39%
4			24.31	−53.60%
5			22.64	−56.79%

Table 6.7: Experimental flexural moduli computed form force vs displacement results and difference from the reference value for coupon TT1-01 in pristine flipped condition and coupon TTD-01.

composite materials.The objective was to gain more detailed insights into the strain distribution and damage propagation along the entire length of the fiber, thereby enhancing the overall understanding of the material behaviour under loading conditions.

The distributed fibre optic sensors were installed on two different specimens following a specific configuration:

- TTD-01: The fibre optic was installed on the top surface, following the path illustrated in the Fig.(6.25a), with a forward and return loop along the red line. An additional unbonded branch was included to prevent fibre breakage, given the small dimensions of the specimen.

- TT1-01: Before installing the fiber optic, a hole was introduced to create an artificial damage site. The sensor was then mounted in a similar configuration to ensure comprehensive strain monitoring, as schematize in Fig.(6.25b).

The BVD in specimen TTD-01 was located at a distance $d = 80$ mm from

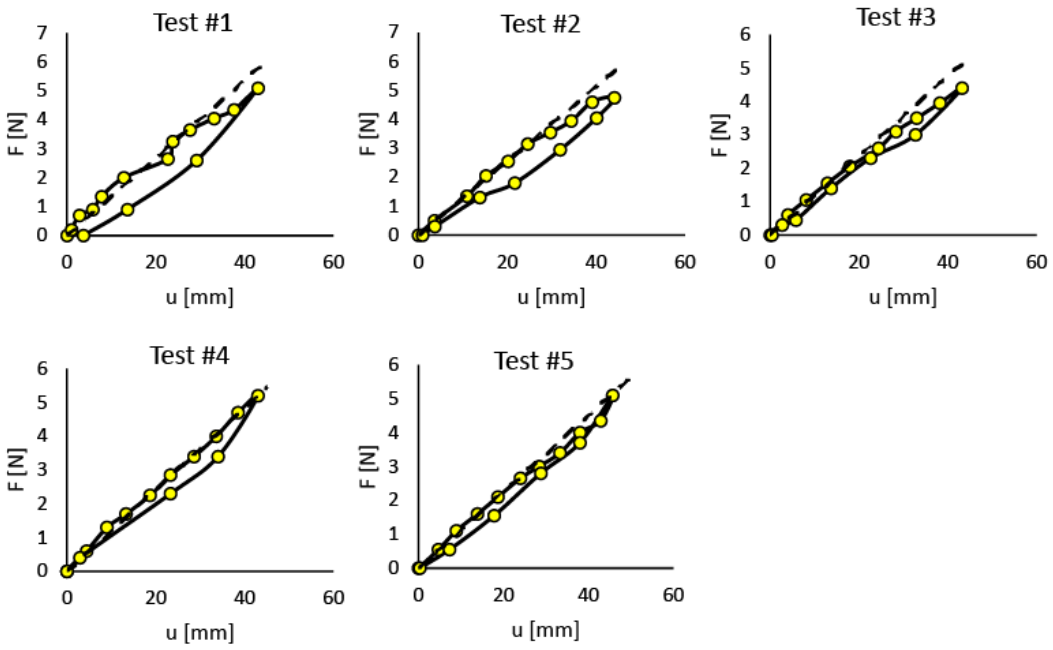

Figure 6.22: Force–displacement plots for specimen TTD-01.

the encastre, while the hole in specimen TT1-01 was at a distance $q = 36.5$ mm as reported in Tab.(5.5). Fig.(6.26) and Fig.(6.27) shows results for three different cantilever tests for TTD-01 and TT1-01 specimen respectively, where each different curve represents a load level. The vertical axis displays the value in microstrain obtained from the sensor reading while the horizontal axis represents the length of the fibre optic. It is worth noting the values of microstrain go to zero in the unbounded branch. As can be seen, in both cases the sensing system was capable of detecting the presence of damage. For specimen TTD-01 the fibre optic localised the damage, which is represented by a peak in the microstrain measure, with an approximate error of $e = 6 - 50\%$ relative to the position of the BVD. For specimens TT1-01 with artificial damage the error computed in the localisation of damage was $e = 4 - 10\%$. The relatively high error in damage localisation for specimen TTD-01 can be attributed to the fact that the specimen had already been tested six times.

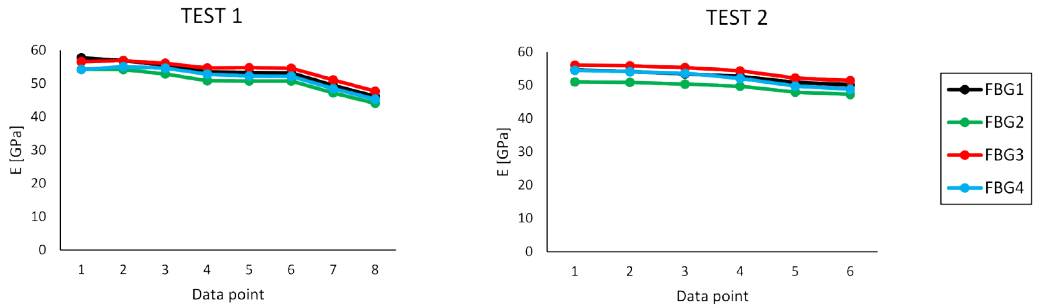

Figure 6.23: Computed flexural modulus at each data point using readings from four FBGs installed in specimen TT1-01 flipped.

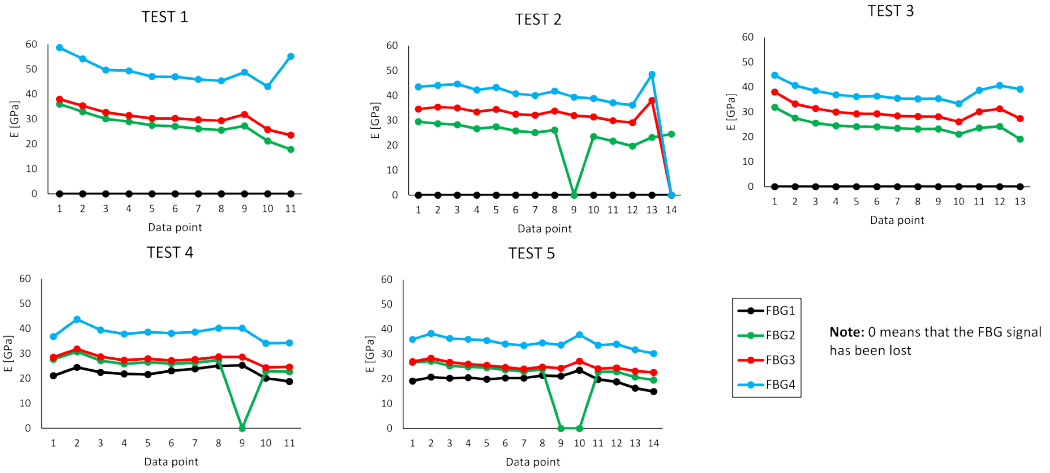

Figure 6.24: Computed flexural modulus at each data point using readings from four FBGs installed in specimen TTD-01.

(a) (b)

Figure 6.25: Schematic representation of installed distributed fibre optic for (a) specimen TTD-01 and (b) specimen TT1-01 with artificial damage.

Consequently, additional damage may have developed in areas away from the BVD, contributing to the increased error. Furthermore, since the specimen was subjected to an impact, and without microscopic scans assessing the actual internal state of the damage, it is not certain that the damage developed precisely at the BVD location. On the other hand, in the TT1 specimen, which was intact and had well-defined artificial damage, the localization error was significantly lower and within a reasonable range.

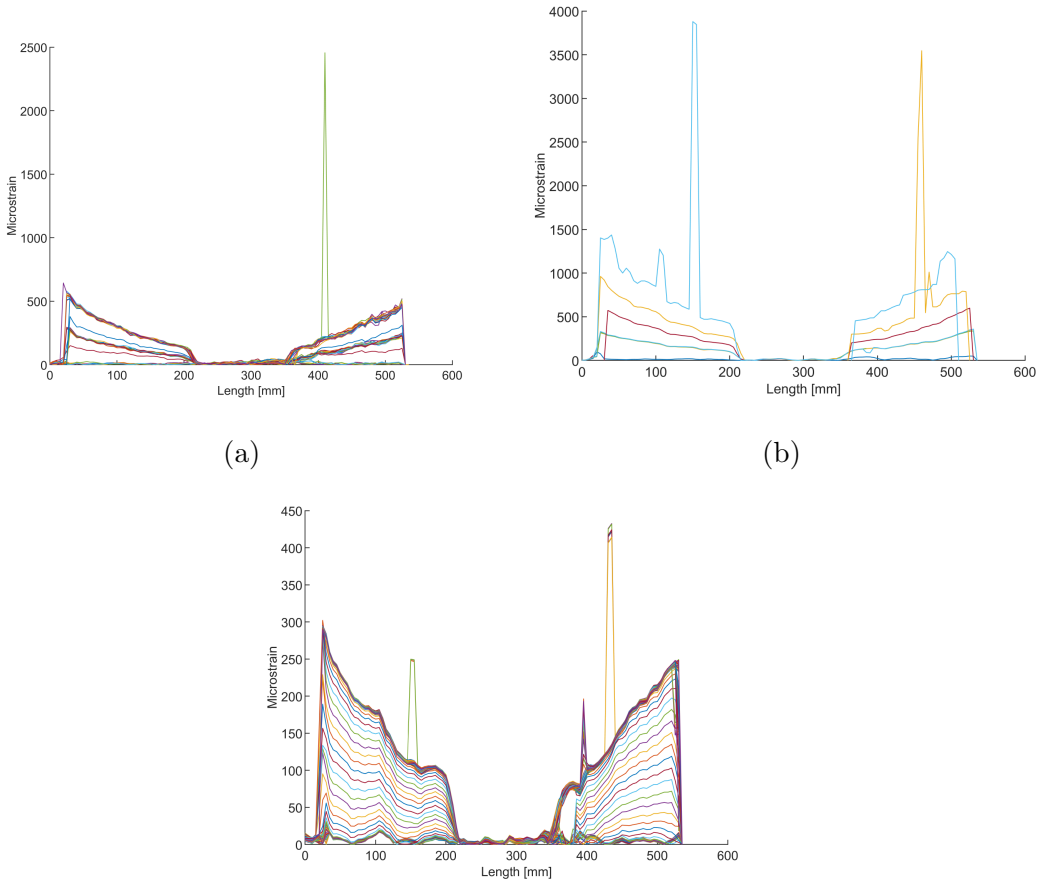

Figure 6.26: Variation of microstrain along the length of specimen TTD-01 obtained from fiber optic readings.

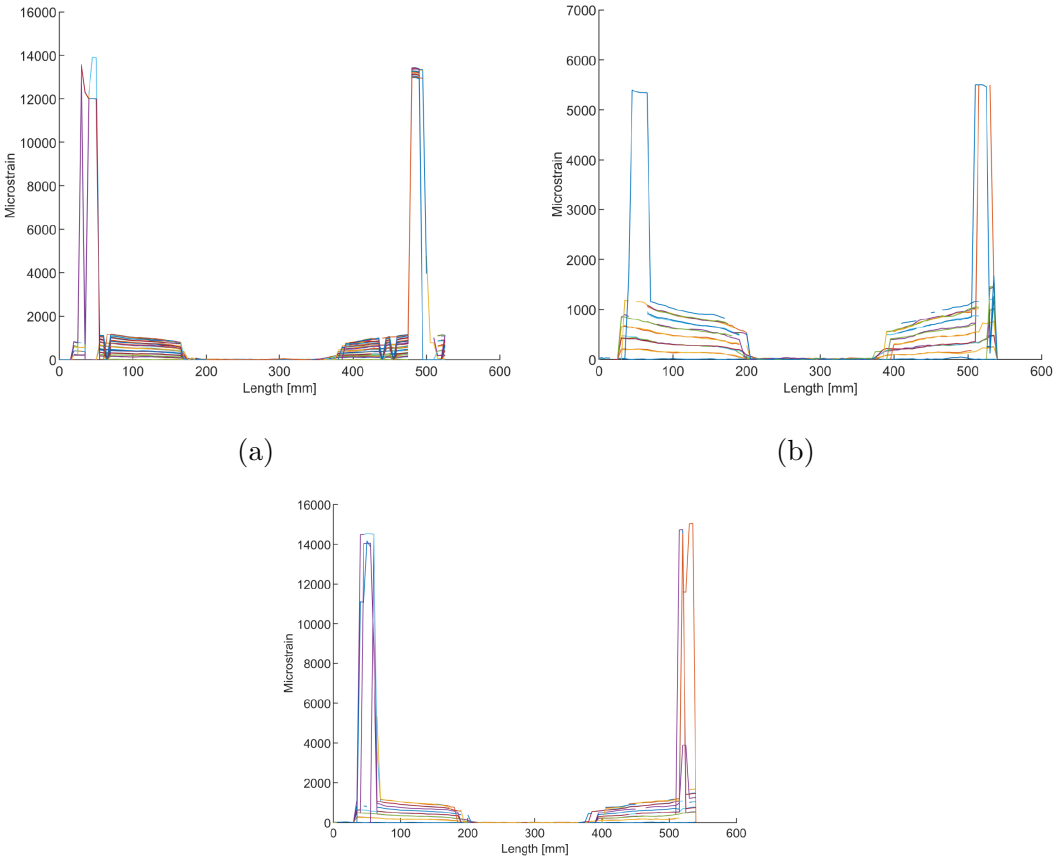

Figure 6.27: Variation of microstrain along the length of specimen TT1-01 with artificial damage obtained from fiber optic readings.

6.4 Experimental results for TB2

The final set of experimental tests focused on the remaining coupons that had not been previously tested. The primary goal of this phase was to verify and assess the robustness and reliability of the experimental procedures employed in the tests. The evaluation of these additional coupons aimed to ensure the consistency and accuracy of the experimental setup and to validate the findings from the earlier tests.

The experimental setup for TB2 followed the same procedure as the previous tests. Each coupon was carefully prepared and subjected to quasi-static loading conditions. Unlike the earlier tests, these coupons were not equipped with sensors. Instead, the focus was on monitoring force and displacement to validate the overall experimental procedure.

The results from TB2 are presented in three figures, each illustrating the force-displacement curves for the remaining coupons: Fig.(6.28) shows the force-displacement results for TT1 coupons, Fig.(6.29) shows the force-displacement results for TT2 coupons, and Fig.(6.30) shows the force-displacement results for TTD coupons. These curves provide an overview of the structural behavior under loading and help identify any deviations or anomalies in the experimental data.

To further validate the experimental procedure, the computed flexural moduli E_{exp} for the remaining coupons were compared with the reference flexural moduli E_{ref}. This comparison is presented in Tabs.(6.8 – 6.10), which highlights the differences between the computed and reference values. The comparison shows that the differences from reference values are minimal for TT1 and TT2 coupons, validating the reliability of the experimental setup and the accuracy of the force and displacement measurements. However, the results of TT1-07 coupon were rejected due to the high difference from the reference

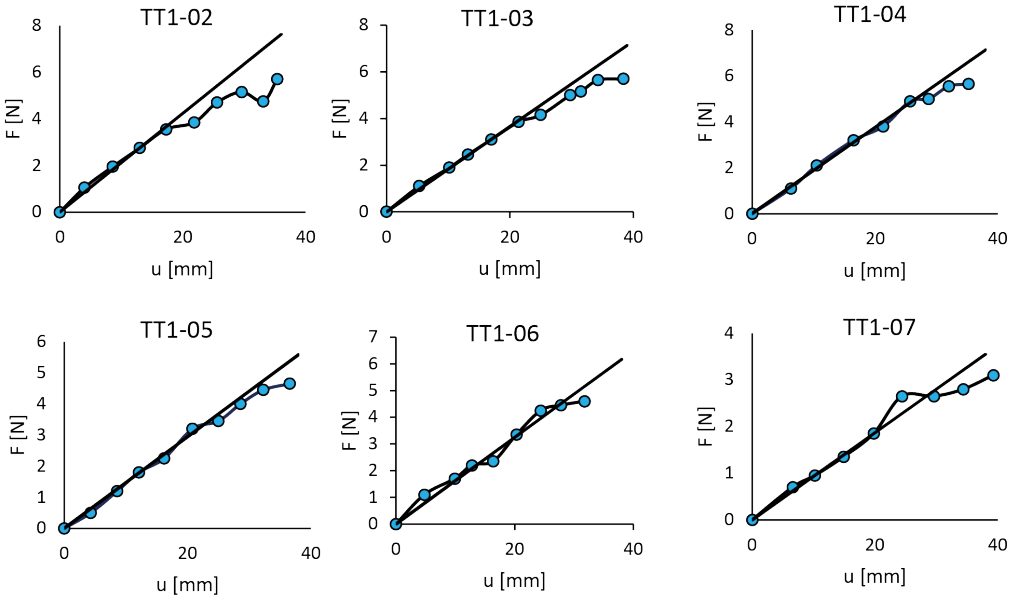

Figure 6.28: Force–displacement plots for specimen group TT1.

value. Indeed, after a visual inspection, it was clear that the coupon had been poorly manufactured. For the TTD coupons, the deviation from the reference values is higher due to damage, which affects the structural integrity and response.

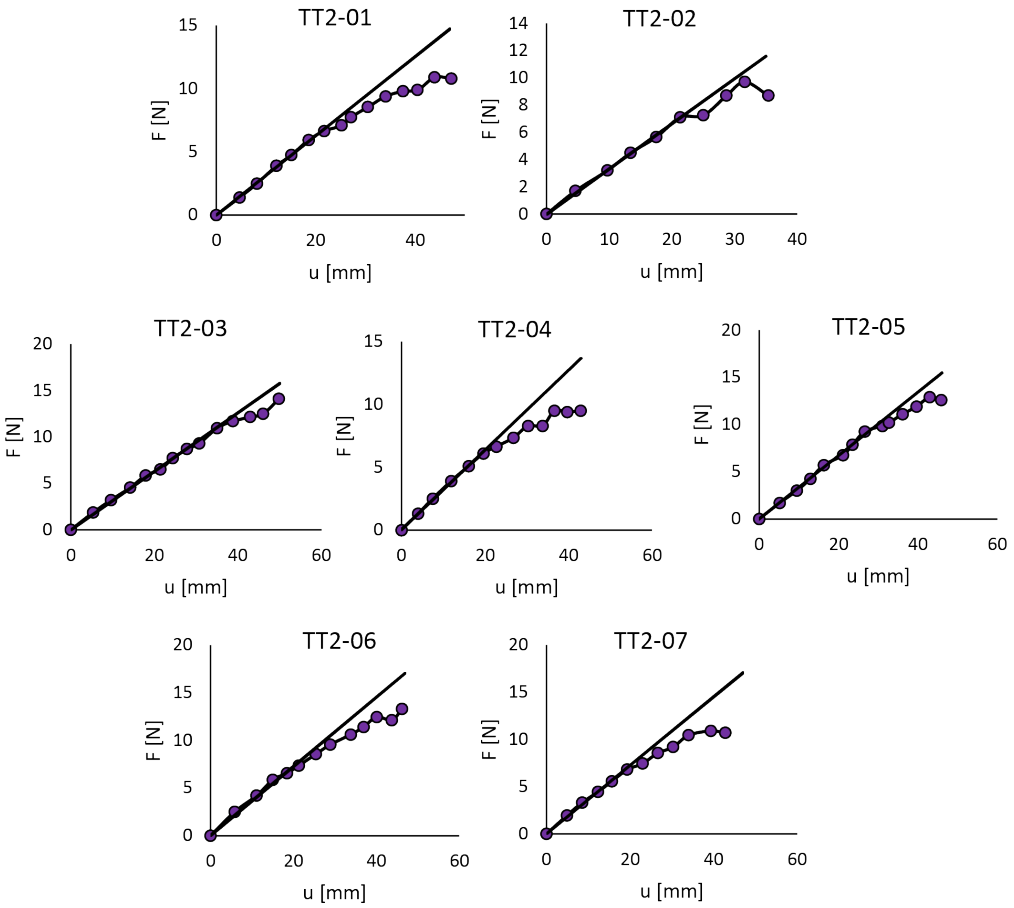

Figure 6.29: Force–displacement plots for specimen group TT2.

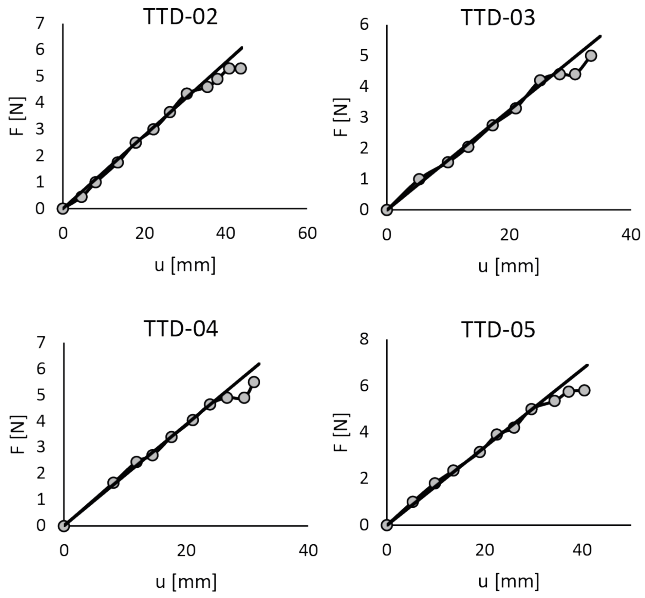

Figure 6.30: Force–displacement plots for specimen group TTD.

Coupon ID	E_{exp} [GPa]	Diff from E_{ref}
TT1-02	56.38	7.59%
TT1-03	51.89	−0.97%
TT1-04	53.77	2.61%
TT1-05	54.95	4.86%
TT1-06	53.48	2.06%
TT1-07	24.94	−52.40%

Table 6.8: Experimental flexural moduli computed form force vs displacement results and difference from the reference value for coupon TT1 in pristine condition.

Coupon ID	E_{exp} [GPa]	Diff from E_{ref}
TT2-01	46.78	−10.73%
TT2-02	49.76	−5.04%
TT2-03	51.86	−1.02%
TT2-04	43.22	−17.53%
TT2-05	55.17	5.29%
TT2-06	54.09	3.23%
TT2-07	50.98	−2.70%

Table 6.9: Experimental flexural moduli computed form force vs displacement results and difference from the reference value for coupon TT2 in pristine condition.

Coupon ID	E_{exp} [GPa]	Diff from E_{ref}
TTD-02	42.15	−19.56%
TTD-03	30.64	−41.53%
TTD-04	43.40	−17.17%
TTD-05	47.15	−10.03%

Table 6.10: Experimental flexural moduli computed form force vs displacement results and difference from the reference value for coupons TTD with BVD.

Chapter 7

Conclusions and future works

The proposed numerical formulation offers valuable insights into the initiation, evolution, and failure of composite laminates, including VAT configurations, with a remarkable reduction in computational costs, in terms of number of DOFs with respect to more popular approaches. The developed tool may be used to efficiently investigate damage characteristics of VAT and classical laminates and find trade-off design solutions. Moreover, it simplifies the data preparation stage of the analysis, as it frees the user from the need of preparing a suitable mesh for capturing the features of the VAT plates, which may require a noticeable amount of time and attention. In the present model, only the polynomial order must be selected according to the features of the underlying problem. However, it has been shown that the coupling of a classical single-domain Ritz approach, may result in an un-physical response, due to the spreading of spurious numerical effects. Hence, designers and engineers must consider the constraints and limitations associated with different modelling and computational tools while predicting the structural behaviour of composite materials and components.

The proposed adaptive hp-Ritz approach has shown to be a good alterna-

tive to classical FE-based analysis. It is worth noting that, the generalised displacements over the patches where damage localises are approximated using first-order polynomials, whilst the larger undamaged sub-domains retain a higher polynomial degree to avoid losing accuracy. The use of first-order polynomials is crucial for representing uniform strain states in the damaged areas, which allows capturing uniform damage evolution within the considered damaged patches.

Although the proposed hp refinement solves the spurious effects arising in single-domain approaches, classical CDM approaches still bear known issues linked with the discretization grids [130]. Indeed, the proposed technique can capture cases in which damage localises in narrow bands while a single-domain approach succeeds in capturing cases where damage is distributed over a well-defined finite region [28]. In the last numerical case, the introduction of a multi-domain splitting may incur in localisation issues and associated spurious dependencies, analogously to what happens in FE-CDM models, if no regularisation technique is adopted. Therefore, different damage models could be investigated, e.g. non-local, phase field or gradient approaches [128, 141, 32].

From a more physical standpoint, the model might be expanded to take into account additional damage mechanisms, such as impact-induced damage or inter-laminar delamination. Layer-wise displacement approximations along the thickness, hybrid variational statements [142], and cohesive inter-laminar traction-separation laws [143, 71] could all be used to describe delamination. The direct modelling of the displacement jump between adjacent layers and their relationship to inter-laminar damage, all the way to complete decohesion, would be made possible by these techniques. In order to trace the evolution of impact-induced damage, it is possible to examine contact mechanics laws that are appropriate for describing the localised mechanical effects of impacts [12] in conjunction with the incremental approach proposed in this work.

Although the numerical models have not yet been directly validated with different experimental results, the experimental tests conducted in this study provide important preliminary insights. These tests involved thermoplastic composite coupons equipped with various sensors commonly used in SHM systems, such as FBGs and distributed fibre optics.

The tests were divided into two batches. In the first batch, selected coupons were tested to assess the capabilities of the sensors in detecting and locating damage. The second batch aimed to verify the robustness and reliability of the experimental setup by focusing on recording force and displacement data. The preliminary findings from these tests are encouraging and suggest that the sensors can detect damage effectively, providing a foundation for further refinement of the numerical models.

Future research should focus on directly validating the numerical models with extensive experimental data to enhance their accuracy and reliability. This involves conducting more comprehensive experimental tests under various loading conditions and comparing the results with the numerical predictions.

Moreover, integrating advanced sensor technologies and SHM systems with numerical models should be explored to improve damage detection and monitoring capabilities. Developing sophisticated algorithms for data analysis and interpretation, including the use of machine learning and artificial intelligence, can help in predicting damage progression and optimising maintenance strategies.

Expanding the scope of experimental tests considering different types of composite materials and varying loading conditions will provide a more comprehensive understanding of damage mechanisms and sensor performance. This will lead to more robust and reliable SHM systems, ensuring the safety and longevity of engineering structures.

In summary, while the current study lays a solid foundation, continued

research and development are necessary to fully realise the potential of SHM systems and advanced numerical models in the maintenance and management of composite structures.

Appendix A

Governing equation matrices

The matrices appearing in the right-hand side of Eq.(4.12) have the following expressions

$$\boldsymbol{K}_0 = \int_\Omega \begin{bmatrix} \left(\boldsymbol{\mathcal{B}}_{pU}^\intercal \boldsymbol{A} \boldsymbol{\mathcal{B}}_{pU} + \boldsymbol{\mathcal{B}}_{nU}^\intercal \boldsymbol{A}_s \boldsymbol{\mathcal{B}}_{nU}\right) & \left(\boldsymbol{\mathcal{B}}_{pU}^\intercal \boldsymbol{B} \boldsymbol{\mathcal{B}}_{p\Theta} + \boldsymbol{\mathcal{B}}_{nU} \boldsymbol{A}_s \boldsymbol{\mathcal{B}}_{i\Theta}\right) \\ \left(\boldsymbol{\mathcal{B}}_{p\Theta}^\intercal \boldsymbol{B} \boldsymbol{\mathcal{B}}_{pU} + \boldsymbol{\mathcal{B}}_{i\Theta}^\intercal \boldsymbol{A}_s \boldsymbol{\mathcal{B}}_{nU}\right) & \left(\boldsymbol{\mathcal{B}}_{p\Theta}^\intercal \boldsymbol{D} \boldsymbol{\mathcal{B}}_{p\Theta} + \boldsymbol{\mathcal{B}}_{i\Theta} \boldsymbol{A}_s \boldsymbol{\mathcal{B}}_{i\Theta}\right) \end{bmatrix} d\Omega,$$

$$\boldsymbol{K}_1 = \frac{1}{2} \int_\Omega \begin{bmatrix} \left(\boldsymbol{\mathcal{B}}_{pU}^\intercal \boldsymbol{A} \boldsymbol{\mathcal{B}}_{nlU} + \boldsymbol{\mathcal{B}}_{nlU}^\intercal \boldsymbol{A} \boldsymbol{\mathcal{B}}_{pU}\right) & 2\boldsymbol{\mathcal{B}}_{nlU}^\intercal \boldsymbol{B} \boldsymbol{\mathcal{B}}_{p\Theta} \\ \boldsymbol{\mathcal{B}}_{p\Theta}^\intercal \boldsymbol{B} \boldsymbol{\mathcal{B}}_{nlU} & 0 \end{bmatrix} d\Omega,$$

$$\boldsymbol{K}_2 = \frac{1}{2} \int_\Omega \begin{bmatrix} \boldsymbol{\mathcal{B}}_{nlU}^\intercal \boldsymbol{A} \boldsymbol{\mathcal{B}}_{nlU} & 0 \\ 0 & 0 \end{bmatrix} d\Omega,$$

$$\overline{\boldsymbol{K}}_0 = \int_\Omega \begin{bmatrix} \left(\boldsymbol{\mathcal{B}}_{pU}^\intercal \boldsymbol{A} \bar{\boldsymbol{\mathcal{B}}}_{nlU} + \bar{\boldsymbol{\mathcal{B}}}_{nlU}^\intercal \boldsymbol{A} \boldsymbol{\mathcal{B}}_{pU} + \bar{\boldsymbol{\mathcal{B}}}_{nlU}^\intercal \boldsymbol{A} \bar{\boldsymbol{\mathcal{B}}}_{nlU}\right) & \bar{\boldsymbol{\mathcal{B}}}_{nlU}^\intercal \boldsymbol{B} \boldsymbol{\mathcal{B}}_{p\Theta} \\ \boldsymbol{\mathcal{B}}_{p\Theta}^\intercal \boldsymbol{B} \bar{\boldsymbol{\mathcal{B}}}_{nlU} & 0 \end{bmatrix} d\Omega,$$

$$\overline{\boldsymbol{K}}_1 = \frac{1}{2} \int_\Omega \begin{bmatrix} \left(2\boldsymbol{\mathcal{B}}_{nlU}^\intercal \boldsymbol{A} \bar{\boldsymbol{\mathcal{B}}}_{nlU} + \bar{\boldsymbol{\mathcal{B}}}_{nlU}^\intercal \boldsymbol{A} \boldsymbol{\mathcal{B}}_{nlU}\right) & 0 \\ 0 & 0 \end{bmatrix} d\Omega,$$

$$\boldsymbol{R} = \int_\Omega \begin{bmatrix} \boldsymbol{\Phi}_u^\intercal \boldsymbol{\Xi}_u^\intercal \boldsymbol{\omega}_u \boldsymbol{\Xi}_u \boldsymbol{\Phi}_u & 0 \\ 0 & \boldsymbol{\Phi}_\vartheta^\intercal \boldsymbol{\Xi}_\vartheta^\intercal \boldsymbol{\omega}_\vartheta \boldsymbol{\Xi}_\vartheta \boldsymbol{\Phi}_\vartheta \end{bmatrix} d\Omega, \tag{A.1}$$

The matrices appearing in the left-hand side of Eq.(4.12) have the following expressions

$$\boldsymbol{F}_L = \int_\Omega \begin{Bmatrix} \boldsymbol{\Phi}_u^\intercal \boldsymbol{q} \\ \boldsymbol{\Phi}_\vartheta^\intercal \boldsymbol{m} \end{Bmatrix} d\Omega + \int_{\partial\Omega_l} \begin{Bmatrix} \boldsymbol{\Phi}_u^\intercal \, \overline{\boldsymbol{N}} \\ \boldsymbol{\Phi}_\vartheta^\intercal \, \overline{\boldsymbol{M}} \end{Bmatrix} d\partial\Omega,$$

$$\boldsymbol{F}_D = \int_{\partial\Omega_c} \begin{Bmatrix} \boldsymbol{\Phi}_u^\intercal \boldsymbol{\Xi}_u^\intercal \boldsymbol{\omega}_u \boldsymbol{\Xi}_u \, \bar{\boldsymbol{u}} \\ \boldsymbol{\Phi}_\vartheta^\intercal \boldsymbol{\Xi}_\vartheta^\intercal \boldsymbol{\omega}_\vartheta \boldsymbol{\Xi}_\vartheta \, \bar{\boldsymbol{\vartheta}} \end{Bmatrix} d\partial\Omega. \tag{A.2}$$

The penalty matrix used for for connection between subdomains appearing in Eq. (4.18) is given by

$$\boldsymbol{P}_{pt}^{\langle r,s\rangle} = \int_{\Gamma_{pt}} \begin{bmatrix} \left(\boldsymbol{\Phi}_u^{\langle r\rangle T} \boldsymbol{\Lambda}_u^{\langle r\rangle T} \boldsymbol{\mu}_u^{\langle pt\rangle} \, \boldsymbol{\Lambda}_u^{\langle s\rangle} \boldsymbol{\Phi}_u^{\langle s\rangle} \right) & \boldsymbol{0} \\ \boldsymbol{0} & \left(\boldsymbol{\Phi}_\vartheta^{\langle r\rangle T} \boldsymbol{\Lambda}_\vartheta^{\langle r\rangle T} \boldsymbol{\mu}_\vartheta^{\langle pt\rangle} \, \boldsymbol{\Lambda}_\vartheta^{\langle s\rangle} \boldsymbol{\Phi}_\vartheta^{\langle s\rangle} \right) \end{bmatrix} d\Gamma \tag{A.3}$$

Appendix B

Tangent stiffness matrix contributions

The tangent stiffness matrix contribution $\boldsymbol{K}_{t,geo}$, related to the geometric non-linearity in Eq.(4.14), is computed as

$$\boldsymbol{K}_{t,geo} = \boldsymbol{K}_{1t} + \overline{\boldsymbol{K}}_{1t} + \boldsymbol{K}_{2t} + \boldsymbol{K}_{G}, \tag{B.1}$$

where the matrices $\boldsymbol{K}_{1t}$, $\boldsymbol{K}_{2t}$, $\overline{\boldsymbol{K}}_{1t}$ and $\boldsymbol{K}_{G}$ are defined as

$$\boldsymbol{K}_{1t} = \int_{\Omega} \begin{bmatrix} \left(\boldsymbol{\mathcal{B}}_{pU}^{\intercal} \boldsymbol{A} \boldsymbol{\mathcal{B}}_{nlU} + \boldsymbol{\mathcal{B}}_{nlU}^{\intercal} \boldsymbol{A} \boldsymbol{\mathcal{B}}_{pU}\right) & \boldsymbol{\mathcal{B}}_{nlU}^{\intercal} \boldsymbol{B} \boldsymbol{\mathcal{B}}_{p\Theta} \\ \boldsymbol{\mathcal{B}}_{p\Theta}^{\intercal} \boldsymbol{B} \boldsymbol{\mathcal{B}}_{nlU} & 0 \end{bmatrix} d\Omega,$$

$$\overline{\boldsymbol{K}}_{1t} = \int_{\Omega} \begin{bmatrix} \left(\boldsymbol{\mathcal{B}}_{nlU}^{\intercal} \boldsymbol{A} \bar{\boldsymbol{\mathcal{B}}}_{nlU} + \bar{\boldsymbol{\mathcal{B}}}_{nlU}^{\intercal} \boldsymbol{A} \boldsymbol{\mathcal{B}}_{nlU}\right) & 0 \\ 0 & 0 \end{bmatrix} d\Omega, \tag{B.2}$$

$$\boldsymbol{K}_{2t} = \int_{\Omega} \begin{bmatrix} \boldsymbol{\mathcal{B}}_{nlU}^{\intercal} \boldsymbol{A} \boldsymbol{\mathcal{B}}_{nlU} & 0 \\ 0 & 0 \end{bmatrix} d\Omega, \qquad \boldsymbol{K}_{G} = \int_{\Omega} \begin{bmatrix} \boldsymbol{\mathcal{B}}_{nU}^{\intercal} \widehat{\widehat{\boldsymbol{N}}} \boldsymbol{\mathcal{B}}_{nU} & 0 \\ 0 & 0 \end{bmatrix} d\Omega,$$

where

$$\widehat{\boldsymbol{N}} = \begin{bmatrix} N_{11} & N_{12} & 0 \\ N_{12} & N_{22} & 0 \\ 0 & 0 & 0 \end{bmatrix}. \tag{B.3}$$

The tangent stiffness matrix contribution $\boldsymbol{K}_{t,dmg}$, related to the damage evolution in Eq.(4.14), is computed as

$$\boldsymbol{K}_{t,dmg} = \boldsymbol{K}_{0D} + \boldsymbol{K}_{12D}. \tag{B.4}$$

The terms $\boldsymbol{K}_{0D}$ and $\boldsymbol{K}_{12D}$ are more specifically related to the damage-induced evolution of the small-strains contribution $\boldsymbol{K}_0$ to the stiffness matrix and to the contribution originating from the geometric non-linearity respectively.

Regarding the first term, from Eq.(4.14) ones can write

$$\Delta\left(\boldsymbol{K}_0\boldsymbol{X}\right) = \boldsymbol{K}_0\Delta\boldsymbol{X} + \Delta\boldsymbol{K}_0\boldsymbol{X}. \tag{B.5}$$

The second term of the right hand-side in Eq.(B.5) can be written as

$$\Delta\boldsymbol{K}_0\boldsymbol{X} = \Delta\begin{bmatrix} \boldsymbol{K}_0^{11} & \boldsymbol{K}_0^{12} \\ \boldsymbol{K}_0^{21} & \boldsymbol{K}_0^{22} \end{bmatrix}\begin{Bmatrix} \boldsymbol{U} \\ \boldsymbol{\Theta} \end{Bmatrix}. \tag{B.6}$$

The detailed computation is developed only for the first term $\boldsymbol{K}_0^{11}$ of the matrix appearing in Eq.(B.6), being the computation of the other terms similar. One may write

$$\Delta\left(\boldsymbol{K}_0^{11}\right)\boldsymbol{U} = \Delta\left[\int_\Omega \left(\boldsymbol{\mathcal{B}}_{pU}^{\intercal}\boldsymbol{A}\boldsymbol{\mathcal{B}}_{pU} + \boldsymbol{\mathcal{B}}_{nU}^{\intercal}\boldsymbol{A}_s\boldsymbol{\mathcal{B}}_{nU}\right)d\Omega\right]\boldsymbol{U} \tag{B.7}$$

and then, noting that, in the present formulation, the second term within the integral sign does not depend on damage, recalling Eq.(3.23)

$$\begin{aligned} \Delta\left(\boldsymbol{K}_0^{11}\right)\boldsymbol{U} &= \int_\Omega \sum_{i,k}\int_{h_{k-1}}^{h_k} \boldsymbol{\mathcal{B}}_{pU}^{\intercal}\Delta\left(\boldsymbol{Q}_{p,i}\right)\boldsymbol{\mathcal{B}}_{pU}\boldsymbol{U}dx_3d\Omega = \\ &= \int_\Omega \sum_{i,k}\int_{h_{k-1}}^{h_k} \boldsymbol{\mathcal{B}}_{pU}^{\intercal}\frac{\partial\boldsymbol{Q}_{p,i}}{\partial\omega_i^v}\frac{\partial\omega_i^v}{\partial\omega_i}\frac{\partial\omega_i}{\partial e_{i,eq}}\frac{\partial e_{i,eq}}{\partial\boldsymbol{e}_p}\frac{\partial\boldsymbol{e}_p}{\partial\boldsymbol{X}}\Delta\boldsymbol{X}\boldsymbol{\mathcal{B}}_{pU}\boldsymbol{U}dx_3d\Omega \end{aligned} \tag{B.8}$$

where the derivation chain rule has been applied and the summation is intended for $i \in \{ft, fc, mt, mc\}$ and $k \in [1, N_{ply}]$. The derivatives involved in Eq.(B.8) may be computed as

$$\begin{aligned} \frac{\partial \omega_i^v}{\partial \omega_i} &= \frac{\Delta\tau}{\beta + \Delta\tau}, \qquad \frac{\partial \omega_i}{\partial e_{i,eq}} = \frac{\alpha_i}{\alpha_i - 1}\left(\frac{e_{i,eq}^0}{e_{i,eq}^2}\right), \\ \frac{\partial e_{i,eq}}{\partial \boldsymbol{e}_p} &= \left\{ \frac{\partial e_{i,eq}}{\partial e_{11}} \quad \frac{\partial e_{i,eq}}{\partial e_{22}} \quad \frac{\partial e_{i,eq}}{\partial e_{12}}, \right\} \\ \frac{\partial \boldsymbol{e}_p}{\partial \boldsymbol{X}} \Delta \boldsymbol{X} &= \boldsymbol{\mathcal{B}}_{pU} \Delta \boldsymbol{U} + x_3 \boldsymbol{\mathcal{B}}_{p\Theta} \Delta \boldsymbol{\Theta} + \boldsymbol{\mathcal{B}}_{nlU} \Delta \boldsymbol{U}. \end{aligned} \tag{B.9}$$

Noting that the product of Eqs.(B.9) results in a scalar, this block is conveniently moved at the end of the integral as follows

$$\begin{aligned} &\int_\Omega \sum_{i,k} \int_{h_{k-1}}^{h_k} \boldsymbol{\mathcal{B}}_{pU}^\intercal \frac{\partial \boldsymbol{Q}_{p,i}}{\partial \omega_i^v} \boldsymbol{\mathcal{B}}_{pU} \boldsymbol{U} \frac{\partial \omega_i^v}{\partial \omega_i} \frac{\partial \omega_i}{\partial e_{i,eq}} \frac{\partial e_{i,eq}}{\partial \boldsymbol{e}_p} \frac{\partial \boldsymbol{e}_p}{\partial \boldsymbol{X}} \Delta \boldsymbol{X} \, dx_3 d\Omega = \\ &= \int_\Omega \boldsymbol{\mathcal{B}}_{pU}^\intercal \left[\sum_{i,k} \int_{h_{k-1}}^{h_k} \frac{\partial \boldsymbol{Q}_{p,i}}{\partial \omega_i^v} \boldsymbol{\mathcal{B}}_{pU} \boldsymbol{U} \zeta(\alpha_i, \beta, \Delta\tau) dx_3 \right] \boldsymbol{\mathcal{B}}_{pU} \Delta \boldsymbol{U} + \\ &+ \boldsymbol{\mathcal{B}}_{pU}^\intercal \left[\sum_{i,k} \int_{h_{k-1}}^{h_k} \frac{\partial \boldsymbol{Q}_{p,i}}{\partial \omega_i^v} \boldsymbol{\mathcal{B}}_{pU} \boldsymbol{U} \zeta(\alpha_i, \beta, \Delta\tau) x_3 dx_3 \right] \boldsymbol{\mathcal{B}}_{pU} \Delta \boldsymbol{\Theta} + \\ &+ \boldsymbol{\mathcal{B}}_{pU}^\intercal \left[\sum_{i,k} \int_{h_{k-1}}^{h_k} \frac{\partial \boldsymbol{Q}_{p,i}}{\partial \omega_i^v} \boldsymbol{\mathcal{B}}_{pU} \boldsymbol{U} \zeta(\alpha_i, \beta, \Delta\tau) dx_3 \right] \boldsymbol{\mathcal{B}}_{nlU} \Delta \boldsymbol{U} d\Omega = \\ &= \int_\Omega \boldsymbol{\mathcal{B}}_{pU}^\intercal \boldsymbol{A}^{*,1} \boldsymbol{\mathcal{B}}_{pU} \Delta \boldsymbol{U} + \boldsymbol{\mathcal{B}}_{pU}^\intercal \boldsymbol{B}^{*,1} \boldsymbol{\mathcal{B}}_{pU} \Delta \boldsymbol{\Theta} + \boldsymbol{\mathcal{B}}_{pU}^\intercal \boldsymbol{A}^{*,1} \boldsymbol{\mathcal{B}}_{nlU} \Delta \boldsymbol{U} d\Omega, \end{aligned} \tag{B.10}$$

where

$$\zeta(\alpha_i, \beta, \Delta\tau) = \frac{\Delta\tau}{\beta + \Delta\tau} \frac{\alpha_i}{\alpha_i - 1} \left(\frac{e_{i,eq}^0}{e_{i,eq}^2}\right) \frac{\partial e_{i,eq}}{\partial \boldsymbol{e}_p}. \tag{B.11}$$

Repeating the same procedures for all the elements of the matrix $\boldsymbol{K}_0$, the final expression of the matrix $\boldsymbol{K}_{0D}$ is obtained as

$$\boldsymbol{K}_{0D} = \boldsymbol{K}_0 + \int_\Omega \begin{bmatrix} \boldsymbol{\mathcal{B}}_{pU}^\intercal \boldsymbol{A}^* \left(\boldsymbol{\mathcal{B}}_{pU} + \boldsymbol{\mathcal{B}}_{nlU} \right) & \boldsymbol{\mathcal{B}}_{pU}^\intercal \boldsymbol{B}^* \boldsymbol{\mathcal{B}}_{p\Theta} \\ \boldsymbol{\mathcal{B}}_{p\Theta}^\intercal \boldsymbol{B}^* \left(\boldsymbol{\mathcal{B}}_{pU} + \boldsymbol{\mathcal{B}}_{nlU} \right) & \boldsymbol{\mathcal{B}}_{p\Theta}^\intercal \boldsymbol{D}^* \boldsymbol{\mathcal{B}}_{p\Theta} \end{bmatrix} d\Omega, \tag{B.12}$$

where

$$\begin{aligned}
\boldsymbol{A}^{*} &= \sum_{i,k} \int_{h_{k-1}}^{h_k} \frac{\partial \boldsymbol{Q}_{p,i}}{\partial \omega_i^v} \left(\boldsymbol{\mathcal{B}}_{pU}\boldsymbol{U} + x_3 \boldsymbol{\mathcal{B}}_{p\Theta}\boldsymbol{\Theta}\right) \zeta(\alpha_i, \beta, \Delta\tau) dx_3, \\
\boldsymbol{B}^{*} &= \sum_{i,k} \int_{h_{k-1}}^{h_k} \frac{\partial \boldsymbol{Q}_{p,i}}{\partial \omega_i^v} \left(\boldsymbol{\mathcal{B}}_{pU}\boldsymbol{U} + x_3 \boldsymbol{\mathcal{B}}_{p\Theta}\boldsymbol{\Theta}\right) \zeta(\alpha_i, \beta, \Delta\tau) x_3 dx_3, \\
\boldsymbol{D}^{*} &= \sum_{i,k} \int_{h_{k-1}}^{h_k} \frac{\partial \boldsymbol{Q}_{p,i}}{\partial \omega_i^v} \left(\boldsymbol{\mathcal{B}}_{pU}\boldsymbol{U} + x_3 \boldsymbol{\mathcal{B}}_{p\Theta}\boldsymbol{\Theta}\right) \zeta(\alpha_i, \beta, \Delta\tau) x_3^2 dx_3.
\end{aligned} \tag{B.13}$$

The same procedure is repeated for computing the tangent stiffness terms related to the material degradation in the non-linear geometry matrix contributions, which leads to

$$\boldsymbol{K}_{12D} = \boldsymbol{K}_{1D} + \boldsymbol{K}_{2D} \tag{B.14}$$

where $\boldsymbol{K}_{1D}$ is given by

$$\int_{\Omega} \begin{bmatrix} \boldsymbol{\mathcal{B}}_{pU}^{\intercal} \boldsymbol{A}^{**} \left(\boldsymbol{\mathcal{B}}_{pU} + \boldsymbol{\mathcal{B}}_{nlU}\right) + \boldsymbol{\mathcal{B}}_{nlU}^{\intercal} \boldsymbol{A}^{\#} \boldsymbol{\mathcal{B}}_{pU} & \left(\boldsymbol{\mathcal{B}}_{pU}^{\intercal} \boldsymbol{B}^{**} \boldsymbol{\mathcal{B}}_{p\Theta} + \boldsymbol{\mathcal{B}}_{nlU}^{\intercal} \boldsymbol{B}^{\#} \boldsymbol{\mathcal{B}}_{p\Theta}\right) \\ \left(\boldsymbol{\mathcal{B}}_{p\Theta}^{\intercal} \boldsymbol{B}^{**} \boldsymbol{\mathcal{B}}_{pU} + \boldsymbol{\mathcal{B}}_{p\Theta}^{\intercal} \boldsymbol{B}^{**} \boldsymbol{\mathcal{B}}_{nlU}\right) & \boldsymbol{\mathcal{B}}_{p\Theta}^{\intercal} \boldsymbol{D}^{**} \boldsymbol{\mathcal{B}}_{p\Theta} \end{bmatrix} d\Omega \tag{B.15}$$

and

$$\boldsymbol{K}_{2D} = \int_{\Omega} \begin{bmatrix} \boldsymbol{\mathcal{B}}_{nlU}^{\intercal} \boldsymbol{A}^{\#} \boldsymbol{\mathcal{B}}_{nlU} & 0 \\ 0 & 0 \end{bmatrix} d\Omega, \tag{B.16}$$

in which

$$\begin{aligned}
\boldsymbol{A}^{**} &= \sum_{i,k} \int_{h_{k-1}}^{h_k} \frac{1}{2} \frac{\partial \boldsymbol{Q}_{p,i}}{\partial \omega_i^v} \boldsymbol{\mathcal{B}}_{nlU} \boldsymbol{U} \zeta(\alpha_i, \beta, \Delta\tau) dx_3 \\
\boldsymbol{B}^{**} &= \sum_{i,k} \int_{h_{k-1}}^{h_k} \frac{1}{2} \frac{\partial \boldsymbol{Q}_{p,i}}{\partial \omega_i^v} \boldsymbol{\mathcal{B}}_{nlU} \boldsymbol{U} \zeta(\alpha_i, \beta, \Delta\tau) x_3 dx_3 \\
\boldsymbol{D}^{**} &= \sum_{i,k} \int_{h_{k-1}}^{h_k} \frac{1}{2} \frac{\partial \boldsymbol{Q}_{p,i}}{\partial \omega_i^v} \boldsymbol{\mathcal{B}}_{nlU} \boldsymbol{U} \zeta(\alpha_i, \beta, \Delta\tau) x_3^2 dx_3 \\
\boldsymbol{A}^{\#} &= \sum_{i,k} \int_{h_{k-1}}^{h_k} \frac{\partial \boldsymbol{Q}_{p,i}}{\partial \omega_i^v} \left(\boldsymbol{\mathcal{B}}_{pU} \boldsymbol{U} + x_3 \boldsymbol{\mathcal{B}}_{p\Theta} \boldsymbol{\Theta} + \frac{1}{2} \boldsymbol{\mathcal{B}}_{nlU} \boldsymbol{U} \right) \zeta(\alpha_i, \beta, \Delta\tau) dx_3 \\
\boldsymbol{B}^{\#} &= \sum_{i,k} \int_{h_{k-1}}^{h_k} \frac{\partial \boldsymbol{Q}_{p,i}}{\partial \omega_i^v} \left(\boldsymbol{\mathcal{B}}_{pU} \boldsymbol{U} + x_3 \boldsymbol{\mathcal{B}}_{p\Theta} \boldsymbol{\Theta} + \frac{1}{2} \boldsymbol{\mathcal{B}}_{nlU} \boldsymbol{U} \right) \zeta(\alpha_i, \beta, \Delta\tau) x_3 dx_3.
\end{aligned} \tag{B.17}$$

Bibliography

[1] Tita, V., de Carvalho, J., and Vandepitte, D. Failure analysis of low velocity impact on thin composite laminates: Experimental and numerical approaches. *Composite Structures*, 83(4):413–428, 2008.

[2] Yao, S.-S., Jin, F.-L., Rhee, K. Y., Hui, D., and Park, S.-J. Recent advances in carbon-fiber-reinforced thermoplastic composites: A review. *Composites Part B: Engineering*, 142:241–250, 2018. ISSN 1359-8368. doi: https://doi.org/10.1016/j.compositesb.2017.12.007.

[3] Reis, J. P., de Moura, M., and Samborski, S. Thermoplastic composites and their promising applications in joining and repair composites structures: A review. *Materials*, 13(24), 2020. ISSN 1996-1944. doi: 10.3390/ma13245832.

[4] Parandoush, P. and Lin, D. A review on additive manufacturing of polymer-fiber composites. *Composite Structures*, 182:36–53, 2017.

[5] Yassin, K. and Hojjati, M. Processing of thermoplastic matrix composites through automated fiber placement and tape laying methods: A review. *Journal of Thermoplastic Composite Materials*, 31(12):1676–1725, 2018.

[6] Oliveri, V., Zucco, G., Peeters, D., Clancy, G., Telford, R., Rouhi, M., McHale, C., O'Higgins, R. M., Young, T. M., and Weaver, P. M. Design,

manufacture and test of an in-situ consolidated thermoplastic variable-stiffness wingbox. *AIAA Journal*, 57(4):1671–1683, 2019.

[7] Dhinakaran, V., Surendar, K., Hasunfur Riyaz, M., and Ravichandran, M. Review on study of thermosetting and thermoplastic materials in the automated fiber placement process. *Materials Today: Proceedings*, 27: 812–815, 2020. First International conference on Advanced Lightweight Materials and Structures.

[8] Gürdal, Z., Tatting, B., and Wu, C. Variable stiffness composite panels: Effects of stiffness variation on the in-plane and buckling response. *Composites Part A: Applied Science and Manufacturing*, 39(5):911–922, 2008.

[9] Milazzo, A. and Oliveri, V. Investigation of buckling characteristics of cracked variable stiffness composite plates by an extended ritz approach. *Thin-Walled Structures*, 163:107750, 2021.

[10] Sciascia, G., Oliveri, V., and Weaver, P. M. Dynamic analysis of pre-stressed variable stiffness composite shell structures. *Thin-Walled Structures*, 175:109193, 2022.

[11] Sciascia, G., Oliveri, V., and Weaver, P. M. Dynamic performance of hygrothermal mechanically preloaded variable-stiffness composite fairing structures. *AIAA Journal*, pages 1–18, 2023.

[12] Milazzo, A. and Benedetti, I. A non-linear ritz method for the analysis of low velocity impact induced dynamics in variable angle tow composite laminates. *Composite Structures*, 276, 2021.

[13] Kant, T. and Pandya, B. A simple finite element formulation of a higher-

order theory for unsymmetrically laminated composite plates. *Composite Structures*, 9(3):215–246, 1988.

[14] Carrera, E. Theories and finite elements for multilayered, anisotropic, composite plates and shells. *Archives of Computational Methods in Engineering*, 9(2):87–140, 2002.

[15] Demasi, L. Treatment of stress variables in advanced multilayered plate elements based upon reissner's mixed variational theorem. *Computers & Structures*, 84(19):1215–1221, 2006. ISSN 0045-7949.

[16] Caliri Jr, M. F., Ferreira, A. J., and Tita, V. A review on plate and shell theories for laminated and sandwich structures highlighting the finite element method. *Composite Structures*, 156:63–77, 2016.

[17] Demasi, L., Biagini, G., Vannucci, F., Santarpia, E., and Cavallaro, R. Equivalent single layer, zig-zag, and layer wise theories for variable angle tow composites based on the generalized unified formulation. *Composite Structures*, 177:54–79, 2017.

[18] Tornabene, F., Fantuzzi, N., and Bacciocchi, M. The gdq method for the free vibration analysis of arbitrarily shaped laminated composite shells using a nurbs-based isogeometric approach. *Composite Structures*, 154: 190–218, 2016.

[19] Gulizzi, V., Benedetti, I., and Milazzo, A. An implicit mesh discontinuous galerkin formulation for higher-order plate theories. *Mechanics of Advanced Materials and Structures*, 27(17):1494–1508, 2020.

[20] Gulizzi, V., Benedetti, I., and Milazzo, A. A high-resolution layer-wise discontinuous galerkin formulation for multilayered composite plates. *Composite Structures*, 242:112137, 2020.

[21] Benedetti, I., Gulizzi, V., and Milazzo, A. Layer-wise discontinuous galerkin methods for piezoelectric laminates. *Modelling*, 1(2):198–214, 2020.

[22] Milazzo, A. and Oliveri, V. Buckling and postbuckling of stiffened composite panels with cracks and delaminations by ritz approach. *AIAA Journal*, 55(3):965–980, 2017.

[23] Oliveri, V. and Milazzo, A. A rayleigh-ritz approach for postbuckling analysis of variable angle tow composite stiffened panels. *Computers & Structures*, 196:263–276, 2018.

[24] Milazzo, A., Benedetti, I., and Gulizzi, V. An extended ritz formulation for buckling and post-buckling analysis of cracked multilayered plates. *Composite Structures*, 201:980–994, 2018.

[25] Milazzo, A., Benedetti, I., and Gulizzi, V. A single-domain ritz approach for buckling and post-buckling analysis of cracked plates. *International Journal of Solids and Structures*, 159:221–231, 2019.

[26] Chandrakar, P., Sharma, N., and Maiti, D. K. Damage-induced buckling characteristics of thermally loaded variable angle tow laminated plates under uncertain environment. *European Journal of Mechanics-A/Solids*, 103:105188, 2024.

[27] Pan, Z., Zhang, L., and Liew, K. A phase-field framework for failure modeling of variable stiffness composite laminae. *Computer Methods in Applied Mechanics and Engineering*, 388:114192, 2022.

[28] Campagna, D., Milazzo, A., Benedetti, I., and Oliveri, V. A non-linear ritz method for progressive failure analysis of variable angle tow com-

posite laminates. *Mechanics of Advanced Materials and Structures*, 30 (5):995–1008, 2023.

[29] Dang, T. D. and Hallett, S. R. A numerical study on impact and compression after impact behaviour of variable angle tow laminates. *Composite Structures*, 96:194–206, 2013.

[30] Dang, T. D., Hallet, S. R., Kim, B. C., Cahain, Y. L., Butler, R., and Liu, W. Modelling of as manufactured geometry for prediction of impact and compression after impact behaviour of variable angle tow laminates. *Journal of Composite Materials*, 49(12):1423–1438, 2015.

[31] Pan, Z., Zhang, L., and Liew, K. A phase-field framework for failure modeling of variable stiffness composite laminae. *Computer Methods in Applied Mechanics and Engineering*, 388:114192, 2022.

[32] Natarajan, S., Annabattula, R. K., et al. Modeling crack propagation in variable stiffness composite laminates using the phase field method. *Composite Structures*, 209:424–433, 2019.

[33] González, C. and LLorca, J. Mechanical behavior of unidirectional fiber-reinforced polymers under transverse compression: Microscopic mechanisms and modeling. *Composites Science and Technology*, 67(13):2795–2806, 2007.

[34] Benedetti, I., Gulizzi, V., and Milazzo, A. A microstructural model for homogenisation and cracking of piezoelectric polycrystals. *Computer Methods in Applied Mechanics and Engineering*, 357:112595, 2019.

[35] Lo Cascio, M., Milazzo, A., and Benedetti, I. Coupled vem–bem approach for isotropic damage modelling in composite materials. *Journal of Multiscale Modelling*, 14(01):2341001, 2023.

[36] Bergan, A., Dávila, C., Leone, F., Awerbuch, J., and Tan, T.-M. A mode I cohesive law characterization procedure for through-the-thickness crack propagation in composite laminates. *Composites Part B: Engineering*, 94:338–349, 2016.

[37] Li, S., Thouless, M., Waas, A., Schroeder, J., and Zavattieri, P. Use of a cohesive-zone model to analyze the fracture of a fiber-reinforced polymer–matrix composite. *Composites Science and Technology*, 65(3): 537–549, 2005.

[38] Rudraraju, S. S., Salvi, A., Garikipati, K., and Waas, A. M. In-plane fracture of laminated fiber reinforced composites with varying fracture resistance: Experimental observations and numerical crack propagation simulations. *International Journal of Solids and Structures*, 47(7):901–911, 2010.

[39] Matzenmiller, A., Lubliner, J., and Taylor, R. L. A constitutive model for anisotropic damage in fiber-composites. *Mechanics of materials*, 20 (2):125–152, 1995.

[40] Ladeveze, P. and LeDantec, E. Damage modelling of the elementary ply for laminated composites. *Composites science and technology*, 43(3): 257–267, 1992.

[41] Lapczyk, I. and Hurtado, J. A. Progressive damage modeling in fiber-reinforced materials. *Composites Part A: Applied Science and Manufacturing*, 38(11):2333–2341, 2007.

[42] Maimí, P., Camanho, P. P., Mayugo, J., and Dávila, C. A continuum damage model for composite laminates: Part I–constitutive model. *Mechanics of materials*, 39(10):897–908, 2007.

[43] Maimí, P., Camanho, P., Mayugo, J., and Dávila, C. A continuum damage model for composite laminates: Part II - computational implementation and validation. *Mechanics of Materials*, 39:909 – 919, 2007.

[44] Llobet, J., Maimí, P., Essa, Y., and De La Escalera, F. M. A continuum damage model for composite laminates: Part iii-fatigue. *Mechanics of Materials*, 153:103659, 2021.

[45] Llobet, J., Maimí, P., Turon, A., Bak, B., Lindgaard, E., Carreras, L., Essa, Y., and de la Escalera, F. M. A continuum damage model for composite laminates: Part iv-experimental and numerical tests. *Mechanics of Materials*, 154:103686, 2021.

[46] Ladevèze, P., Allix, O., Gornet, L., Lévêque, D., and Perret, L. A computational damage mechanics approach for laminates: identification and comparison with experimental results. In *Studies in Applied Mechanics*, volume 46, pages 481–500. Elsevier, 1998.

[47] Falzon, B. and Apruzzese, P. Numerical analysis of intralaminar failure mechanisms in composite structures. part I: Fe implementation. *Composite Structures*, 93(2):1039–1046, 2011.

[48] Falzon, B. and Apruzzese, P. Numerical analysis of intralaminar failure mechanisms in composite structures. part II: Applications. *Composite Structures*, 93(2):1047–1053, 2011.

[49] De Luca, A. and Di Felice, G. Modelling the simulation of impact induced damage onset and evolution in composites. *Composites Part B: Engineering*, 66:340–347, 2014.

[50] Benedetti, I., Nguyen, H., Soler-Crespo, R. A., Gao, W., Mao, L., Ghasemi, A., Wen, J., Nguyen, S., and Espinosa, H. D. Formulation

and validation of a reduced order model of 2D materials exhibiting a two-phase microstructure as applied to graphene oxide. *Journal of the Mechanics and Physics of Solids*, 112:66–88, 2018.

[51] Jirásek, M. and Desmorat, R. Localization analysis of nonlocal models with damage-dependent nonlocal interaction. *International Journal of Solids and Structures*, 174:1–17, 2019.

[52] Yang, Q. J. and Hayman, B. Simplified ultimate strength analysis of compressed composite plates with linear material degradation. *Composites Part B: Engineering*, 69:13–21, 2015.

[53] Ghannadpour, S. and Shakeri, M. Application of a new energy-based collocation method for nonlinear progressive damage analysis of imperfect composite plates. *Thin-Walled Structures*, 147:106369, 2020.

[54] Ghannadpour, S. and Abdollahzadeh, N. Progressive failure analysis of thick imperfect composite plates using nonlinear plate theory. *International Journal of Non-Linear Mechanics*, 121:103292, 2020.

[55] Sartorato, M., de Medeiros, R., Vandepitte, D., and Tita, V. Computational model for supporting shm systems design: Damage identification via numerical analyses. *Mechanical Systems and Signal Processing*, 84: 445–461, 2017. ISSN 0888-3270.

[56] Aliabadi, M. H. F. and Sharif Khodaei, Z. *Structural Health Monitoring for Advanced Composite Structures*. WORLD SCIENTIFIC (EUROPE), 2018.

[57] Campagna, D., Oliveri, V., Milazzo, A., Benedetti, I., et al. Progressive non-linear damage of variable angle tow composite plates by a ritz ap-

proach. In *Proceedings of the 10th Design, Modelling and Experiments of Advanced Structures and Systems Conference-DEMEASS2020*, 2022.

[58] Campagna, D., Oliveri, V., Milazzo, A., and Benedetti, I. A ritz model for damage analysis in variable angle tow composite plates. In *AIP Conference Proceedings*, volume 2848. AIP Publishing, 2023.

[59] Campagna, D., Milazzo, A., and Oliveri, V. On modelling damage in composite laminates using the ritz method and continuum damage mechanics. *Aerospace Science and Engineering: III Aerospace PhD-Days*, 33:233, 2023.

[60] Campagna, D., Oliveri, V., Benedetti, I., et al. A semi-analytical continuum damage mechanics model for variable angle tow composite laminates. In *TWENTY-THIRD INTERNATIONAL CONFERENCE ON COMPOSITE MATERIALS (ICCM23)*, 2023.

[61] Campagna, D., Oliveri, V., and Benedetti, I. An adaptive ritz formulation for progressive damage modelling in variable angle tow composite plates. *Composite Structures*, 331:117915, 2024.

[62] Pinho, S. T. *Modelling failure of laminated composites using physically-based failure models*. PhD thesis, University of London, 2005.

[63] Fleck, N. A. and Liu, D. Microbuckle initiation from a patch of large amplitude fibre waviness in a composite under compression and bending. *European Journal of Mechanics-A/Solids*, 20(1):23–37, 2001.

[64] Schultheisz, C. R. and Waas, A. M. Compressive failure of composites, part i: Testing and micromechanical theories. *Progress in Aerospace Sciences*, 32(1):1–42, 1996.

[65] Camanho, P. M. P. R. d. C. *Application of numerical methods to the strength of mechanically fastened joints in composite laminates.* PhD thesis, 1999.

[66] Argon, A. Fracture of composites. *Treatise on materials science and technology*, 1:79–114, 2013.

[67] Iannucci, L. and Ankersen, J. An energy based damage model for thin laminated composites. *Composites Science and Technology*, 66(7-8):934–951, 2006.

[68] Iannucci, L. and Willows, M. An energy based damage mechanics approach to modelling impact onto woven composite materials—part i: Numerical models. *Composites Part A: Applied Science and Manufacturing*, 37(11):2041–2056, 2006.

[69] Iannucci, L. and Willows, M. An energy based damage mechanics approach to modelling impact onto woven composite materials: Part ii. experimental and numerical results. *Composites Part A: Applied Science and Manufacturing*, 38(2):540–554, 2007.

[70] Park, K. and Paulino, G. H. Cohesive zone models: a critical review of traction-separation relationships across fracture surfaces. *Applied Mechanics Reviews*, 64(6):060802, 2011.

[71] Parrinello, F. and Benedetti, I. A coupled plasticity-damage cohesive-frictional interface for low-cycle fatigue analysis. *International Journal of Mechanical Sciences*, 224:107298, 2022.

[72] Yang, Q. and Cox, B. Cohesive models for damage evolution in laminated composites. *International Journal of Fracture*, 133(2):107–137, 2005.

[73] Kachanov, L. M. Rupture time under creep conditions. *International journal of fracture*, 97(1):11–18, 1999.

[74] Kachanov, L. *Introduction to continuum damage mechanics*, volume 10. Springer Science & Business Media, 1986.

[75] Krajcinovic, D. and Lemaitre, J. Continuum damage mechanics. *CISM course, Springer-Verlag*, 1987.

[76] Krajcinovic, D. *Damage mechanics*. Elsevier, 1996.

[77] Ortiz, M. A constitutive theory for the inelastic behavior of concrete. *Mechanics of materials*, 4(1):67–93, 1985.

[78] Lemaitre, J. and Chaboche, J.-L. *Mechanics of solid materials*. Cambridge university press, 1994.

[79] Lemaître, J. and Chaboche, J.-L. Aspect phénoménologique de la rupture par endommagement. *J Méc Appl*, 2(3), 1978.

[80] Bažant, Z. P. and Oh, B. H. Crack band theory for fracture of concrete. *Matériaux et construction*, 16(3):155–177, 1983.

[81] Maimí, P., Camanho, P. P., Mayugo, J.-A., and Dávila, C. G. A thermodynamically consistent damage model for advanced composites. Technical Report TM-2006-214282, NASA, 2006.

[82] Oliver, J. A consistent characteristic length for smeared cracking models. *International Journal for Numerical Methods in Engineering*, 28(2):461–474, 1989.

[83] Yuan, F.-G. *Structural health monitoring (SHM) in aerospace structures*. Woodhead Publishing, 2016.

[84] Giurgiutiu, V. Structural health monitoring of aerospace composites. 2015.

[85] Stolz, C. and Neumair, M. Structural health monitoring, in-service experience, benefit and way ahead. *Structural Health Monitoring*, 9(3): 209–217, 2010.

[86] Goggin, P., Huang, J., White, E., and Haugse, E. Challenges for shm transition to future aerospace systems. *Structural Health Monitoring*, pages 30–41, 2003.

[87] Bossi, R. H. NDE Developments for Composite Structures. *AIP Conference Proceedings*, 820(1):965–971, 03 2006.

[88] Kollgaard, J. R. and LaRiviere, S. G. NDE CHALLENGES WITH FUTURE COMMERCIAL AIRCRAFT–A BOEING PERSPECTIVE. *AIP Conference Proceedings*, 975(1):23–28, 02 2008.

[89] Gupta, R., Mitchell, D., Blanche, J., Harper, S., Tang, W., Pancholi, K., Baines, L., Bucknall, D. G., and Flynn, D. A review of sensing technologies for non-destructive evaluation of structural composite materials. *Journal of Composites Science*, 5(12), 2021. ISSN 2504-477X.

[90] Ajovalasit, A. Advances in strain gauge measurement on composite materials. *Strain*, 47(4):313–325, 2011. doi: https://doi.org/10.1111/j.1475-1305.2009.00691.x.

[91] Hegde, G., Asokan, S., and Hegde, G. Fiber bragg grating sensors for aerospace applications: A review. *ISSS Journal of Micro and Smart Systems*, 11(1):257–275, 2022.

[92] Jodhani, J., Handa, A., Gautam, A., Ashwni, and Rana, R. Ultrasonic non-destructive evaluation of composites: A review. *Materials Today:*

Proceedings, 78:627–632, 2023. ISSN 2214-7853. 3rd Biennial International Conference on Future Learning Aspects of Mechanical Engineering (FLAME 2022).

[93] De Luca, A., Caputo, F., Khodaei, Z. S., and Aliabadi, M. Damage characterization of composite plates under low velocity impact using ultrasonic guided waves. *Composites Part B: Engineering*, 138:168–180, 2018.

[94] Salmanpour, M. S., Sharif Khodaei, Z., and Aliabadi, M. F. Impact damage localisation with piezoelectric sensors under operational and environmental conditions. *Sensors*, 17(5):1178, 2017.

[95] Van Steenkiste, R. J. and Kollár, L. P. Effect of the coating on the stresses and strains in an embedded fiber optic sensor. *Journal of composite materials*, 32(18):1680–1711, 1998.

[96] Gholizadeh, S. A review of non-destructive testing methods of composite materials. *Procedia Structural Integrity*, 1:50–57, 2016. ISSN 2452-3216. XV Portugese Conference on Fracture, PCF 2016, 10-12 February 2016, Paco de Arcos, Portugal.

[97] Yang, Y., Zhang, Y., and Tan, X. Review on vibration-based structural health monitoring techniques and technical codes. *Symmetry*, 13(11), 2021.

[98] Kahandawa, G. C., Epaarachchi, J., Wang, H., and Lau, K.-T. Use of fbg sensors for shm in aerospace structures. *Photonic Sensors*, 2:203–214, 2012.

[99] Soman, R., Wee, J., and Peters, K. Optical fiber sensors for ultrasonic structural health monitoring: A review. *Sensors*, 21(21):7345, 2021.

[100] Qiu, Y., Wang, Q.-b., Zhao, H.-t., Chen, J.-a., and Wang, Y.-y. Review on composite structural health monitoring based on fiber bragg grating sensing principle. *Journal of Shanghai Jiaotong University (Science)*, 18: 129–139, 2013.

[101] Bonopera, M. Fiber-bragg-grating-based displacement sensors: Review of recent advances. *Materials*, 15(16):5561, 2022.

[102] Muanenda, Y., Oton, C. J., and Di Pasquale, F. Application of raman and brillouin scattering phenomena in distributed optical fiber sensing. *Frontiers in Physics*, 7:155, 2019.

[103] Zou, W., He, Z., and Hotate, K. Complete discrimination of strain and temperature using brillouin frequency shift and birefringence in a polarization-maintaining fiber. *Opt. Express*, 17(3):1248–1255, Feb 2009.

[104] Lu, P., Lalam, N., Badar, M., Liu, B., Chorpening, B. T., Buric, M. P., and Ohodnicki, P. R. Distributed optical fiber sensing: Review and perspective. *Applied Physics Reviews*, 6(4):041302, 10 2019.

[105] Murayama, H., Wada, D., and Igawa, H. Structural health monitoring by using fiber-optic distributed strain sensors with high spatial resolution. *Photonic Sensors*, 3:355–376, 2013.

[106] Datta, A., Augustin, M., Gaddikeri, K. M., Viswamurthy, S., Gupta, N., and Sundaram, R. Damage detection in composite aircraft wing-like test-box using distributed fiber optic sensors. *Optical Fiber Technology*, 66:102651, 2021. ISSN 1068-5200.

[107] Güemes, A., Fernandez-Lopez, A., and Fernandez, P. Damage detection in composite structures from fibre optic distributed strain measurements.

In *EWSHM-7th European Workshop on Structural Health Monitoring*, 2014.

[108] Martins, B. L. and Kosmatka, J. B. Detecting damage in a uav composite wing spar using distributed fiber optic strain sensors. In *56th AIAA/ASCE/AHS/ASC Structures, Structural Dynamics, and Materials Conference*, page 0447, 2015.

[109] Bado, M. F., Casas, J. R., and Gómez, J. Post-processing algorithms for distributed optical fiber sensing in structural health monitoring applications. *Structural Health Monitoring*, 20(2):661–680, 2021.

[110] Li, J., Kapania, R. K., and Spillman Jr, W. B. Placement optimization of distributed-sensing fiber optic sensors using genetic algorithms. *AIAA journal*, 46(4):824–836, 2008.

[111] Song, Q., Zhou, P., Peng, H., Hu, Y., Xiao, Q., Wu, H., and Jia, B. Improved localization algorithm for distributed fiber-optic sensor based on merged michelson-sagnac interferometer. *Optics Express*, 28(5):7207–7220, 2020.

[112] Li, J., Khodaei, Z. S., and Aliabadi, M. Boundary element modelling of ultrasonic lamb waves for structural health monitoring. *Smart Materials and Structures*, 29(10):105030, 2020.

[113] Vosoughifar, H. R., Shokouhi, S. K. S., and Farshadmanesh, P. Optimal sensor placement of steel structure with ubf system for shm using hybrid fem-ga technique. In *Civil Structural Health Monitoring Workshop (CSHM-4), Berlin, Germany*, 2012.

[114] Guratzsch, R. F. and Mahadevan, S. Structural health monitoring sensor

placement optimization under uncertainty. *AIAA journal*, 48(7):1281–1289, 2010.

[115] Kefal, A. and Yildiz, M. Modeling of sensor placement strategy for shape sensing and structural health monitoring of a wing-shaped sandwich panel using inverse finite element method. *Sensors*, 17(12):2775, 2017.

[116] Thiene, M., Sharif-Khodaei, Z., and Aliabadi, M. Optimal sensor placement for damage detection based on ultrasonic guided wave. *Key Engineering Materials*, 665:269–272, 2016.

[117] Mallardo, V. and Aliabadi, M. Optimal sensor placement for structural, damage and impact identification: A review. *Structural Durability & Health Monitoring*, 9(4):287, 2013.

[118] Aliabadi, M. and Khodaei, Z. S. Optimal sensor positioning for impact localization in smart composite panels. *Journal of intelligent material systems and structures*, 24(5):559–573, 2013.

[119] Sbarufatti, C., Manes, A., Giglio, M., et al. Probability of detection and false alarms for metallic aerospace panel health monitoring. In *7th International Conference on Condition Monitoring and Machinery Failure Prevention Technologies 2010, CM 2010/MFPT 2010*, pages 1–14, 2010.

[120] Brinker, K. R. *Passively-coded embedded microwave sensors for materials characterization and structural health monitoring (SHM)*. Missouri University of Science and Technology, 2019.

[121] Diodati, G., Sorrentino, A., Pellone, L., Concilio, A., Ciminello, M., Apuleo, G., Shoham, S., Kressel, I., and Bardenstein, D. Numerical

analysis results of debonding damage effects for an shm system application on a typical composite beam. *Aerospace*, 10(6):507, 2023.

[122] De Medeiros, R., Sartorato, M., Ribeiro, M. L., Vandepitte, D., and Tita, V. Numerical and experimental analyses about shm metrics using piezoelectric materials. In *International Conference on Noise and Vibration Engineering (ISMA2012), Leuven, Belgium*, 2012.

[123] Li, G., Neerukatti, R. K., and Chattopadhyay, A. Fully coupled numerical simulation for wave propagation in composite materials. In *ASME International Mechanical Engineering Congress and Exposition*, volume 50633, page V009T17A006. American Society of Mechanical Engineers, 2016.

[124] Lemistre, M. B. and Placko, D. Evaluation of the performance of an electromagnetic shm system for composite, comparison between numerical simulation, experimental data, and ultrasonic investigation. In *Health Monitoring and Smart Nondestructive Evaluation of Structural and Biological Systems III*, volume 5394, pages 148–156. SPIE, 2004.

[125] Reddy, J. N. *Mechanics of laminated composite plates and shells: theory and analysis*. CRC press, 2003.

[126] Hashin, Z. and Rotem, A. A fatigue failure criterion for fiber reinforced materials. *Journal of Composite Materials*, 7(4):448–464, 1973.

[127] Hashin, Z. Failure Criteria for Unidirectional Fiber Composites. *Journal of Applied Mechanics*, 47(2):329–334, 06 1980.

[128] Bažant, Z. P. and Jirásek, M. Nonlocal integral formulations of plasticity and damage: Survey of progress. *Journal of Engineering Mechanics*, 128 (11):1119–1149, 2002.

[129] Jirásek, M. and Bauer, M. Numerical aspects of the crack band approach. *Computers & Structures*, 110-111:60–78, 2012.

[130] Lopes, B., Arruda, M., Almeida-Fernandes, L., Castro, L., Silvestre, N., and Correia, J. Assessment of mesh dependency in the numerical simulation of compact tension tests for orthotropic materials. *Composites Part C: Open Access*, 1:100006, 2020.

[131] Deng, X., Korobenko, A., Yan, J., and Bazilevs, Y. Isogeometric analysis of continuum damage in rotation-free composite shells. *Computer Methods in Applied Mechanics and Engineering*, 284:349–372, 2015.

[132] Yang, Q. J. and Hayman, B. Simplified ultimate strength analysis of compressed composite plates with linear material degradation. *Composites Part B: Engineering*, 69:13–21, 2015.

[133] Smith, S. T., Bradford, M. A., and Oehlers, D. J. Numerical convergence of simple and orthogonal polynomials for the unilateral plate buckling problem using the rayleigh-ritz method. *International Journal for Numerical Methods in Engineering*, 44:1685–1707, 1999.

[134] Zienkiewicz, O. C. and Taylor, R. L. *The finite element method: solid mechanics*, volume 2. Butterworth-heinemann, 2000.

[135] Reddy, J. N. *Energy principles and variational methods in applied mechanics*. John Wiley & Sons, 2017.

[136] MATLAB. *9.10.0.1710957 (R2021a) Update 4*. The MathWorks Inc., Natick, Massachusetts, 2021.

[137] Björck, Å. *Numerical methods for least squares problems*. SIAM, 1996.

[138] Ferreira, G. F., Almeida, J. H. S., Ribeiro, M. L., Ferreira, A. J., and Tita, V. A finite element unified formulation for composite laminates in bending considering progressive damage. *Thin-Walled Structures*, 172: 108864, 2022.

[139] Diaconu, C. G. and Weaver, P. M. Approximate solution and optimum design of compression-loaded, postbuckled laminated composite plates. *AIAA Journal*, 43(4):906–914, 2005.

[140] Davis, J. M. and Hagelstein, P. Gibbs phenomena for some classical orthogonal polynomials. *Journal of Mathematical Analysis and Applications*, 505(1):125574, 2022.

[141] de Borst, R. and Verhoosel, C. V. Gradient damage vs phase-field approaches for fracture: Similarities and differences. *Computer Methods in Applied Mechanics and Engineering*, 312:78–94, 2016.

[142] Benedetti, I. and Milazzo, A. Advanced models for smart multilayered plates based on reissner mixed variational theorem. *Composites Part B: Engineering*, 119:215–229, 2017.

[143] Benedetti, I. and Aliabadi, M. A three-dimensional cohesive-frictional grain-boundary micromechanical model for intergranular degradation and failure in polycrystalline materials. *Computer Methods in Applied Mechanics and Engineering*, 265:36–62, 2013.

Acknowledgements

I would like to thank the support of the PON Ricerca e Innovazione 2014-2020 – Fondo Sociale Europeo, Azione I.1 *Dottorati Innovativi con caratterizzazione Industriale* – Ciclo XXXVI (CUP: B73D2000501 0001 – Scholarship ID: DOT20KTEXX).

La borsa di dottorato è stata cofinanziata con risorse del Programma Operativo Nazionale Ricerca e Innovazione 2014–2020 (CCI 2014IT16M20P005), Fondo Sociale Europeo, Azione I.1 "Dottorati Innovativi con caratterizzazione Industriale"

UNIONE EUROPEA
Fondo Sociale Europeo
Fondo Europeo di Sviluppo Regionale

Ministero dell'Università e della Ricerca